

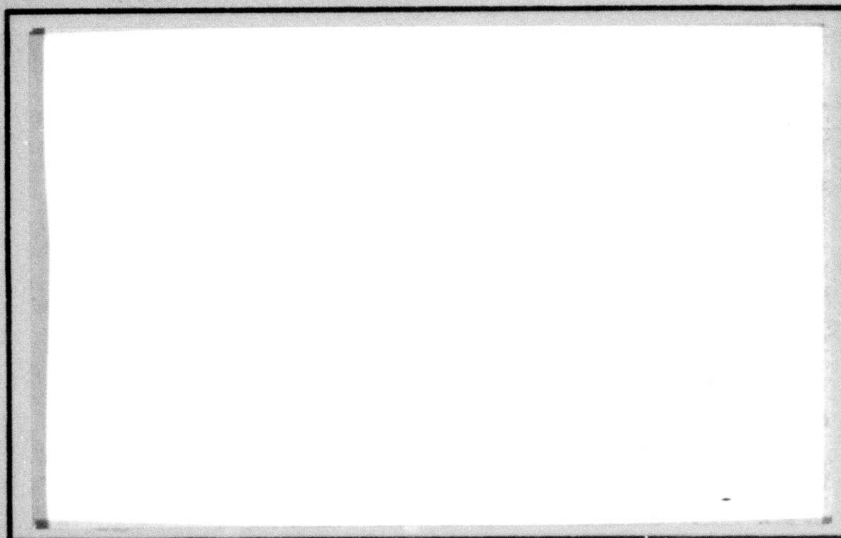
AD A094514

LEVEL



OF **COLLEGE
ENGINEERING**

DTIC
ELECTE
FEB 4 1981
S C



DDC FILE COPY



**VIRGINIA
POLYTECHNIC
INSTITUTE
AND
STATE
UNIVERSITY**

The Ruth H. Hooker Technical Library

JUN 30 1980

Naval Research Laboratory

APPROVED FOR PUBLIC RELEASE
DISTRIBUTION UNLIMITED

APPROVED FOR PUBLIC RELEASE
DISTRIBUTION UNLIMITED

BLACKSBURG,
VIRGINIA

81 2 02 131

1

DTIC
ELECTE
S FEB 4 1981
C

6

NONDESTRUCTIVE EVALUATION OF DAMAGE
IN METAL MATRIX COMPOSITES

by

10

David A. Ulman, Edmund G. Henneke, John C. Duke,
Kenneth L. Reifsnider and Wayne W. Stinchcomb

Department of Engineering Science and Mechanics
Virginia Polytechnic Institute and State University
Blacksburg, Virginia 24061

11 1 Jun 80

12 160

9

Final Report
June 1, 1980

15
ARPA Order No. 3388 Amend 1 and 2

Contract No. N00014-78-C-0153

Contract Effective Date: January 1, 1978

Contract Expiration Date: March 31, 1980

Principal Investigator: E. G. Henneke

(703) 961-5316

ARPA Order - 3388

APPROVED FOR PUBLIC RELEASE
DISTRIBUTION UNLIMITED

The views and conclusions contained in this document are those of the authors and should not be interpreted as necessarily representing the official policies, either expressed or implied, of the Defense Advanced Research Projects Agency or the U.S. Government.

APPROVED FOR PUBLIC RELEASE
DISTRIBUTION UNLIMITED

404722

4B

TABLE OF CONTENTS

	<u>Page</u>
REPORT SUMMARY.	iv
LIST OF SYMBOLS	vi
1. INTRODUCTION.	1
2. INVESTIGATION PROCEDURE	4
2.1 Specimens.	4
2.2 Mechanical Testing	7
2.2.1 Axial Tension Testing	7
2.2.2 Bend Testing.	8
2.2.3 Fatigue Testing	12
2.3 Nondestructive Evaluation Methods.	12
2.3.1 X-Ray Radiography	13
2.3.2 Ultrasonic C-Scan	14
2.3.3 Ultrasonic Attenuation.	16
2.3.4 Thermography.	18
2.3.5 Replication	18
2.3.6 Stiffness Change.	19
2.3.7 Eddy Current.	20
2.3.8 Acoustic Emission	22
2.4 Test Procedure	22
2.5 Notched Specimens.	24
3. RESULTS	29
3.1 Mechanical Tests	29
3.1.1 Axial Tension Tests	29
3.1.2 Static Bend Tests	33
3.1.3 Fatigue Tests	36

TABLE OF CONTENTS (continued)

	<u>Page</u>
3.2 Evaluation of NDE Results.	40
3.2.1 X-Ray Radiography	40
3.2.2 Ultrasonic C-Scan	45
3.2.3 Ultrasonic Attenuation.	49
3.2.4 Thermography.	53
3.2.5 Replication	56
3.2.6 Stiffness Change.	56
3.2.7 Eddy Current.	64
3.2.8 Acoustic Emission	70
3.3 Notched Specimens.	78
3.4 Scanning Electron Microscopy	114
4. DISCUSSION AND SUMMARY.	135
5. CONCLUSIONS	146
6. REFERENCES.	151

Accession For	
NTIS GRA&I	<input checked="" type="checkbox"/>
DTIC TAB	<input type="checkbox"/>
Unannounced	<input type="checkbox"/>
Justification	
By _____	
Distribution/	
Availability Codes	
Avail and/or	
Dist	Special
A	

REPORT SUMMARY

The major purpose of the present work was to develop a technical base for the application of nondestructive evaluation methods to metal matrix composites. To fulfill this aim, several objectives were established: (1) To obtain base line data on non-destructive evaluation methods applied to metal matrix, fiber-reinforced composite coupon specimens with controlled, fabricated flaws; (2) To investigate ways of modifying NDE methods for application to specimens having geometries other than the flat coupon specimens; and (3) To apply appropriate NDE methods to other specimens that would be mechanically tested elsewhere. In particular, these NDE methods should provide quantitative parameters that could be correlated with the mechanical properties.

An evaluation of nondestructive techniques for determining damage in Al/FP composite materials was performed and is presented here. The nondestructive techniques examined include X-ray radiography, ultrasonic C-scan, ultrasonic attenuation, video-thermography, replication, stiffness change, eddy current and acoustic emission. To control the location of damage development notches were manufactured into several specimens. After thorough initial nondestructive characterization, the specimens were fatigued in three point bending to initiate damage. The damage in the specimens was monitored at intermediate fatigue stages by nondestructive evaluation techniques to determine which techniques best characterize the material condition. Replication, radiography and C-scan were determined to be the best NDE techniques used for evaluation of the FP/Al composite. Also, X-ray radiography and ultrasonic C-scan, when compared, can be used to characterize the nature of a given flaw,

and flexural stiffness change can be directly correlated to material damage in particular longitudinal crack length.

In support of this project, Virginia Polytechnic Institute and State University has purchased a Faxitron X-ray radiographic unit using in-house funds. This unit is capable of producing soft (low energy) X-rays that can be used to radiograph composite materials such as graphite-epoxy and the metal matrix composites studied here.

LIST OF SYMBOLS

a:	Notch depth
b:	Beam width
C:	Longitudinal Crack Length
E_1 :	Young's modulus in fiber direction
E_A :	Longitudinal (Young's) modulus of elasticity measured during a quasi-static axial test
$(E_A)_{ULT}$:	The value of E_A at failure*
E_f :	The flexural rigidity calculated from a three point bend test
FL:	The distance between the central load point and the failure location
G_{12} :	The shear modulus of a plane parallel to the fiber orientation and the beam height
h:	The beam height
$I = \frac{bh^3}{12}$:	The moment of inertia
I_E :	The effective moment of inertia assuming the reduced cross-sectional area created by the longitudinal crack
K_I :	Stress intensity factor of the notch tip
L:	Beam length
M:	Moment applied during bend testing
M_{FP} :	Moment applied to failure location
$M_{ULT} = \frac{LP_{ULT}}{4}$:	Moment applied above the central load point at failure*
P:	Load applied during bend test
P_{ULT} :	Load applied by the central load point at failure*
$Q = \frac{b}{2} [\frac{h^2}{4} - y^2]$:	For rectangular beam
r:	Radius of curvature of beam

*The subscript ULT represents the ultimate value.

R :	Resistance measured by eddy current technique
\bar{R} :	Ratio of minimum to maximum fatigue load
$t = b$:	For rectangular beam
$V = \frac{P}{2}$:	Shear force in rectangular beam
V_f :	Fiber volume fraction
X :	Reactance measured by eddy current technique
Y :	Vertical distance from neutral axis of beam
Δ :	Deflection of beam at the central load point
Δ_s :	Deflection of beam due to shearing stresses at the central load point
Δ_b :	Deflection of beam due to pure bending at the central load point
Δ_{ULT} :	Deflection of beam at failure at the central load point*
ϵ_L :	Longitudinal strain (fiber direction).
$(\epsilon_L)_{ULT}$:	Longitudinal strain at failure*
(ϵ_T) :	Transverse strain
$(\epsilon_T)_{ULT}$:	Transverse strain at failure*
ν :	Poisson's ratio
ν_{ULT} :	Poisson's ratio at failure in axial tests*
σ_l :	Stress in fiber direction
σ_R :	Modulus of rupture
σ_{ULT} :	Ultimate stress axial test*
σ_{yp} :	Stress at the material yield point

*The subscript ULT represents the ultimate value.

LIST OF TABLES

- Table 1: Values of Resistance (R) and Reactance (X) Across the Width of FP/Al.
- Table 2: Notch Depth, Normalized Stress Intensity Factor and Tests Performed on Notched Specimens.
- Table 3: Test Matrix of Fatigue Load Increments.
- Table 4: Test Matrix.
- Table 5: Quasi-Static Tension Test Results.
- Table 6: Quasi-Static Bend Test Results.
- Table 7: Fatigue Test Results.
- Table 8A: Longitudinal Stiffness, E_A , and Flexural Stiffness, E_B , for Specimen 16/5.
- Table 8B: Longitudinal Stiffness, E_A , and Flexural Stiffness, E_B , for Specimen 12/4.
- Table 9: Flexural Stiffness for Specimens 15/4 and 11/5.
- Table 10: Reactance (X) and Resistance (R) Measured Across the Surface of a 45% V_f FP/Al Specimen by Eddy Current Technique.
- Table 11: Reactance (X) and Resistance (R) Measured Across the Surface of a 55% V_f FP/Al Specimen by Eddy Current Technique.
- Table 12: Bend Test Results for Notched Specimen 16/4.
- Table 13: Bend Test Results for Notched Specimen 17/4.
- Table 14: Bend Test Results for Notched Specimen 12/5.
- Table 15: Bend Test Results for Notched Specimen 23/5.
- Table 16: Longitudinal Crack Depth and Transverse Crack Length.

1. INTRODUCTION

In order to insure the quality and reliability of advanced composite materials the mechanics of the damage incurred under loading must be understood. To do this, the "damage state" must be characterized at various stages. Then the existing damage state must be related to the remaining strength of material as well as the "stress state" created by a particular loading pattern. The "strength state" or remaining strength of the material is measured by residual strength in a quasi-static failure test. Also since many structures are stiffness critical the relationship between damage and stiffness must be studied.

Manufacturing defects also enter into the complex problem of relating the condition of the material to the performance of the material. A manufacturing defect can affect the material stress state enough to propagate damage and therefore significantly reduce the material strength or stiffness.

In order to attempt to understand the complex physics involved in the failure process, insight into the effects of manufacturing defects and developed damage must be obtained. The logical way to proceed is to detect and characterize the defects and damage, then try to correlate the damage state to the stress state, strength state, stiffness and ultimately the failure process.

Various nondestructive evaluation (NDE) techniques can be used to gain this insight into the material damage state, stress state and strength state. X-ray radiography, ultrasonic C-scan, ultrasonic attenuation, eddy current and replication all provide information about the type of damage or manufactured defects that exist in a material.

Monitoring the stiffness change can characterize the effects of the damage and also provide useful information about the material stress state. Other NDE techniques, such as acoustic emission and thermography monitor the effects of the actual damage development process. Thermal energy and acoustic energy are released when the material stress state is altered by damage propagation. Also, thermal patterns develop during fatigue loading around defects or damage which produce localized stress concentrations.

Previous research efforts have attempted to correlate various NDE information to the stress-state, strength-state and/or damage state in composite materials. Some of the previous efforts which are relevant to this work are summarized below.

Knott [1] used X-ray radiography and ultrasonic C-scan to detect initial manufacturing flaws in boron-aluminum. These initial defects were found to affect the final failure location. Hayford, et al., [2] made a correlation between the shear strength of graphite-polyimide and ultrasonic attenuation. Jones [3] determined that delamination damage could be detected by vibro-thermography. Reifsnider and Masters [4] showed that replication can detect transverse cracks in graphite epoxy. These transverse cracks were also related to stiffness change. Fatigue damage was correlated with the stiffness of graphite-epoxy by O'Brien and Reifsnider [5]. Eddy current was used to detect cracks and fiber orientations in carbon fiber reinforced epoxy by Owston [6]. Acoustic emissions were monitored in metal matrix composites by Henneke, et al., [7,8]. More recently, Russell [9] characterized acoustic emissions from different types of damage development.

The major objective of this work is to investigate several non-destructive evaluation techniques for metal matrix composite materials. In particular, the program is undertaken to determine which NDE techniques can be used to study the damage development process in a ceramic fiber reinforced aluminum. This investigation will provide a basis for further studies into the damage state and the relationship between the damage state and the remaining life, stiffness and strength of the material.

Many different NDE techniques are investigated and evaluated as to their effectiveness in characterizing damage created by a variety of mechanical tests. Axial tension and three point bend tests were performed to characterize the material and to initiate and propagate damage. The results of these studies are reported in the following sections.

2. INVESTIGATION PROCEDURE

2.1 Specimens

All specimens tested were alumina (Al_2O_3) fiber reinforced aluminum manufactured by DuPont. The FP (DuPont trade name) fiber volume fraction (V_f) was either 45 or 55 percent. Specimens were labeled according to their V_f . For example, a specimen numbered 12/5 is the twelfth specimen of 55% V_f and similarly a specimen numbered 8/4 is the eighth specimen of 45% V_f . All specimens had a thickness of 0.101 inches and a length of 6 inches. The 45% V_f specimens had a width of 0.498 inches while the width of 55% V_f specimen was 0.462 inches.

The specimens were fabricated by a matrix injection process. Prepreg tape with a fugitive binder rather than a matrix material was used to consistently orient the fibers. Several strips of prepreg tape were arranged in the desired direction creating a laminated material. The laminate was then placed in a vacuum mold where the binding material was burnt off and molten aluminum matrix material was injected. In this manner, a plate six inches by six inches and approximately 1/2 inch thick was formed. Individual specimens were then sliced from this plate as shown in Figure 1. Thus the plies were oriented parallel to the thickness instead of parallel to the width as in the majority of composite laminates.

To aid in obtaining consistent NDE results, two standard specimens were designed and fabricated. These consisted of aluminum plates glued to FP/Al specimens. The 0.05 inch thick plates had a series of four holes drilled in them. The hole sizes were 6.4, 3.2, 1.6 and 0.8 mm in diameter. Figure 2 is a schematic diagram of a standard specimen. As

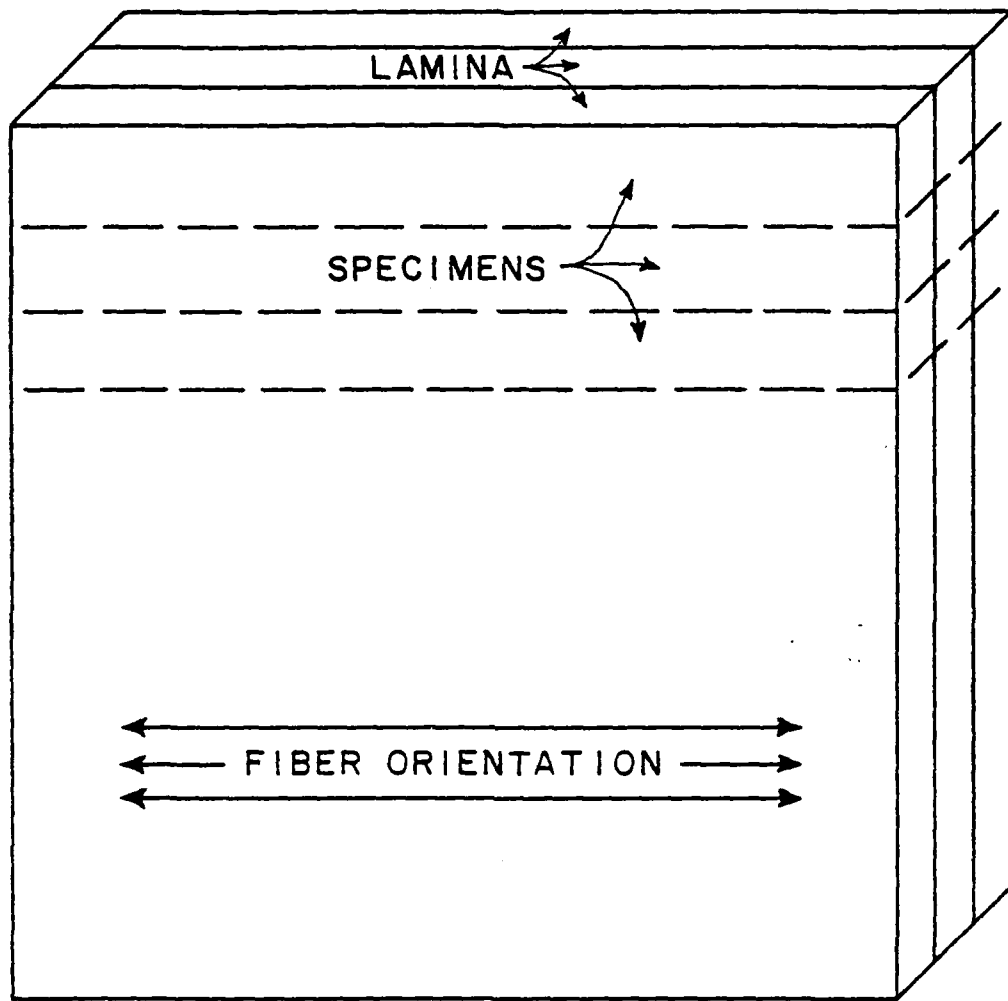


Figure 1: Specimens are sliced perpendicular to the lamina and parallel to the fibers.

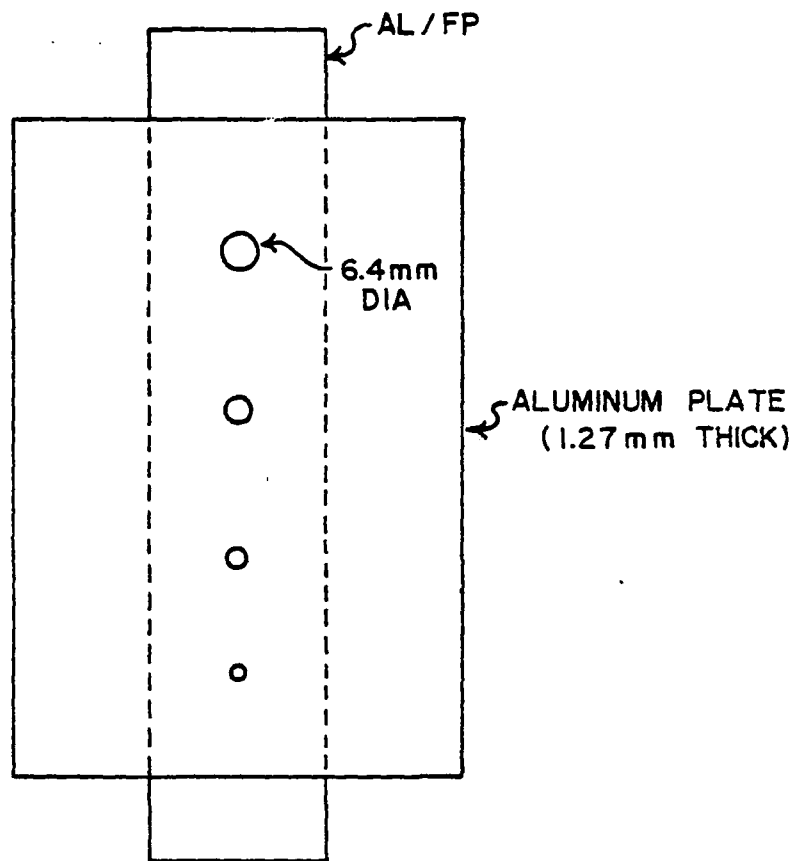


Figure 2: Standard specimen used to calibrate Ultrasonic C-scan and X-ray radiographs.

discussed below the holes served to locate regions in the standard specimen which serve to calibrate NDE parameters from one day to the next.

2.2 Mechanical Testing

All mechanical testing was performed on a 20 kip MTS hydraulic testing machine operating in load control. Tests were performed to initiate damage, characterize damage, or measure material characteristics.

2.2.1 Axial Tension Testing

During all axial tests, the specimen was carefully centered in one inch wide Instron grips until the remaining gauge length between grips was 3 1/2 inches. Between each jaw and the specimen two layers of emery cloth were inserted to prevent specimen damage from the gripping mechanism. The specimen was then loaded at a constant rate of two kips per minute until the maximum desired load, or failure, was obtained. If maximum load was achieved, the unloading rate was 10 kips per minute.

Initially, two specimens of each volume fraction were subjected to an axial, quasi-static tension test to fracture. During these initial tests, longitudinal strain, transverse strain, acoustic emission and ultrasonic attenuation were monitored. Data from these specimens were used to characterize the material properties and behavior.

Other specimens were axially tested to determine if axial stiffness correlates to damage generated by fatigue loading. Before fatigue testing, all specimens were axially loaded twice to a stress of 70 ksi (approximately 85% σ_{ULT}). In addition to stress-strain plots, acoustic

emission was monitored during the first 70 ksi loading, and ultrasonic attenuation was monitored during the second loading. Following the two 70 ksi tests the specimen was loaded to 40 ksi to measure the material axial stiffness, E_1 . The initial stiffness was compared with similar stiffness measurements taken at each intermediate fatigue stage.

2.2.2 Bend Testing

In order to induce damage in a localized region and generate failure in a region not subjected to grip effects, a three-point bend fixture was fabricated. The bend fixture pictured in Figures 3 and 4 loaded each specimen midway between two supporting pins 5.5 inches apart. Three-point bending subjects a beam to large shear stresses which, when applied to laminated materials, can create delaminations along ply interfaces. The ply interfaces discussed previously are oriented in the plane in which the shear stresses act; thus, if any defects exist along ply interfaces, a delamination might result.

The shear stresses, along with normal stresses created by bending, can be approximated by classical Euler-Bernoulli beam theory. As in classical beam theory [10,11] it is assumed that plane sections remain plane. This implies that the longitudinal strain component ϵ_x varies linearly with y , or

$$\epsilon_1 = \frac{y}{r} \quad (1)$$

The beam is assumed to be constructed of a linearly elastic, homogeneous material in which the only significant stress components are σ_1 and τ_{12} . Therefore, we can rewrite (1) as

$$\sigma_1 = \frac{y}{Er}$$

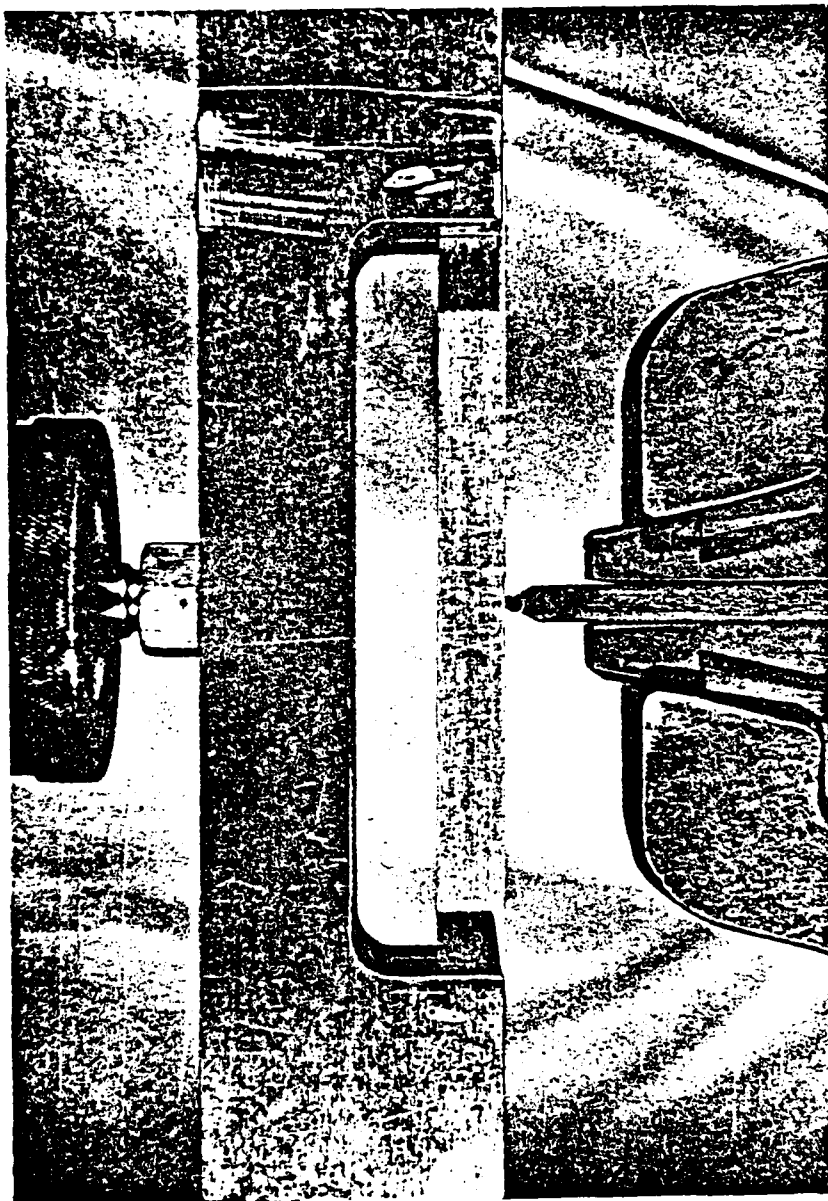


Figure 3: Bend test fixture for static and cyclic loading of FP/Al Specimens.

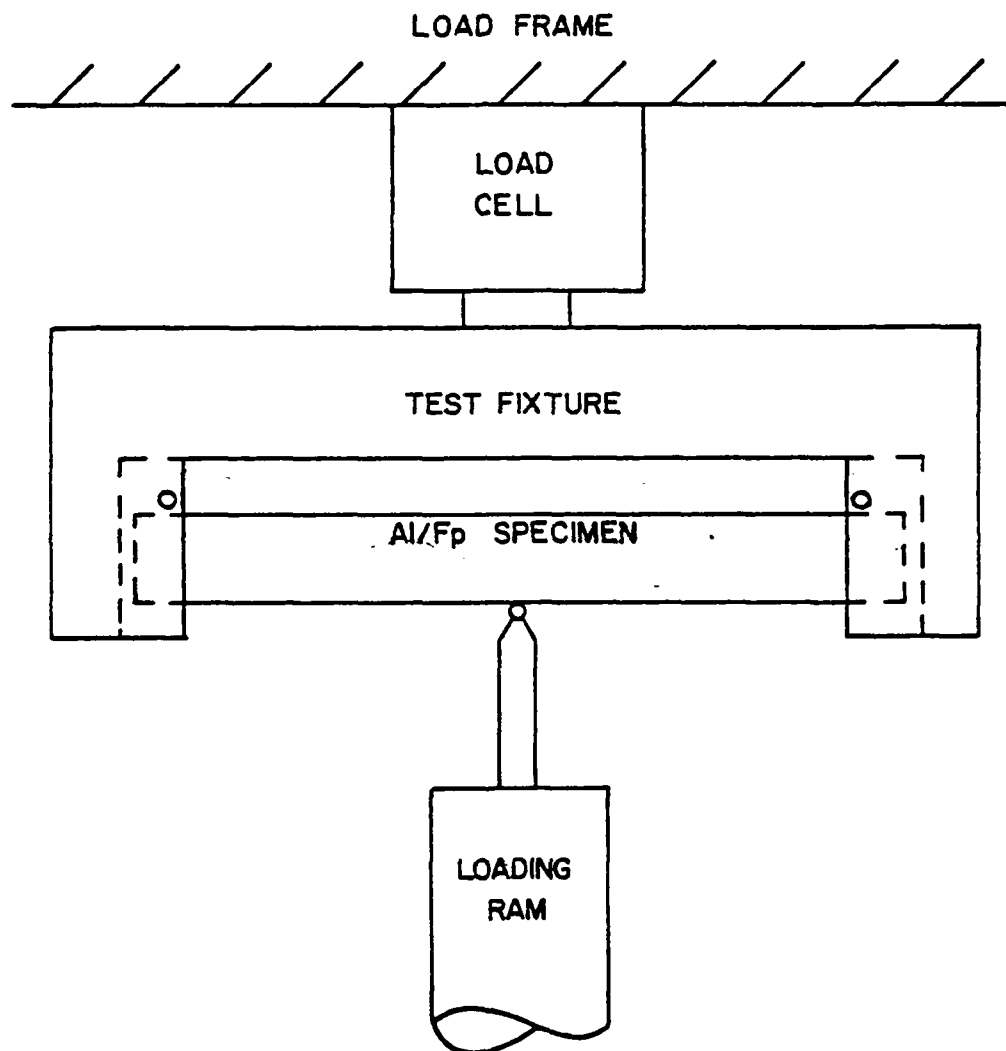


Figure 4: Schematic representation of the three point bend fixture

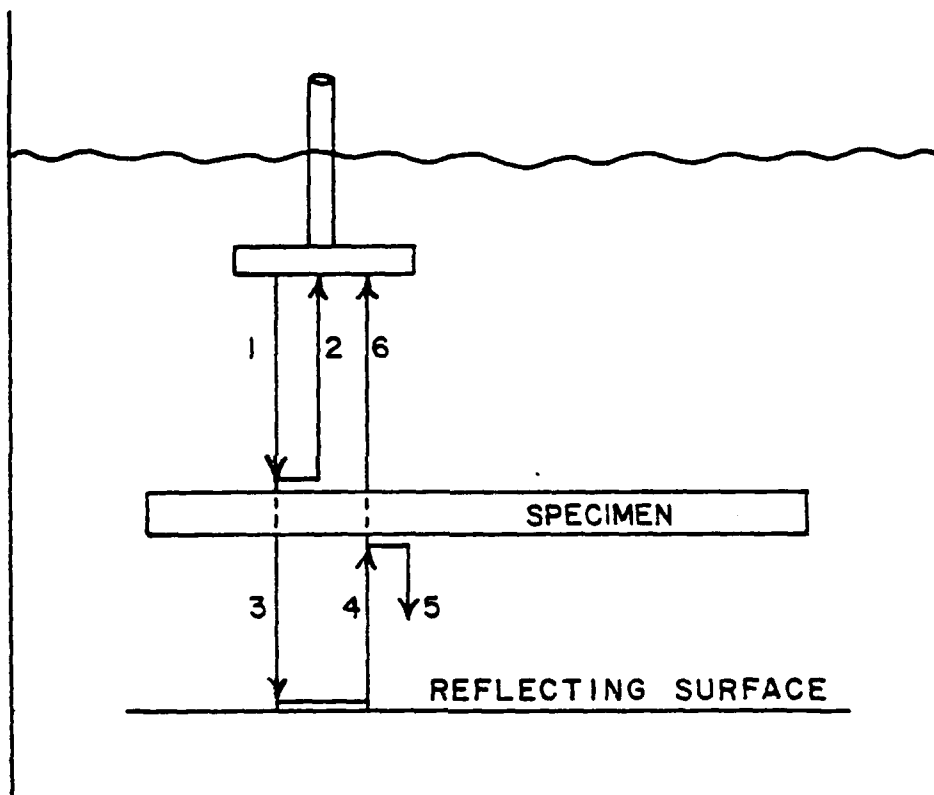


Figure 5: Schematic representation of the Ultrasonic C-scan echoes

If equilibrium is enforced we can write the normal stress in the familiar form

$$\sigma_1 = \frac{My}{I} \quad (2)$$

Similarly, the shear stress can be written

$$\tau_{12} = \frac{VQ}{It} \quad (3)$$

If the shear stress is assumed not to contribute to the vertical deflection of the beam, the deflection can be written as

$$\Delta = \frac{PL^3}{48EI}$$

For composite beams, Zweben, et al., [12] state that the shear deflection can be significant for length to span ratios as high as 60 to 1. Unlike polymer matrix composites, FP/Al beams have high ratios of shear modulus to extensional modulus which compensates for low length to depth ratios (11.90 for 55% V_f , 11.04 for 45% V_f). The ratio of the shear deflection to the deflection due to pure bending is given by Zweben et al., [12] as

$$\frac{\Delta_s}{\Delta_b} = 1.2 \left(\frac{E_1}{G_{12}} \right) \left(\frac{h}{L} \right)^2$$

For FP/Al composite beams, this ratio is 0.041 and 0.045 for 55% V_f and 45% V_f specimens, respectively. Therefore, the assumption neglecting shear deformation creates less than a 5% error in the apparent flexural modulus, E_f defined as

$$E_f = \frac{PL^3}{48I\Delta} \quad (4)$$

Changes in the flexural modulus are due to changes in the material stiffness values E_1 and/or G_{12} .

Another parameter needed for analysis is the modulus of rupture (σ_R) defined as

$$\sigma_R = \frac{M_{FL} b}{2I}$$

The modulus of rupture is the stress at the failure location calculated assuming that equation (2) is valid. Since many materials have non-linear stress-strain plots this parameter is used to give a value of "failure stress" for the purposes of comparison only.

It is also important to note that the expressions for bending stresses in laminated beams, such as those derived by Pagano [13] and Whitney [14], reduce to the classical beam theory expressions described here when the material is considered homogeneous. For this work the assumption of homogeneous behavior on a macroscopic level was used.

2.2.3 Fatigue Testing

Specimens underwent fatigue testing in three point bending to initiate and grow damage. All fatigue tests were performed at a frequency of 10 Hz with a maximum to minimum load ratio of ten ($\bar{R}=0.1$). The intermediate loading stages at which the specimen was removed for nondestructive evaluation were 10K, 50K, 100K, 150K, 250K, 400K, 600K, 800K, and 1000K cycles (K = 1000 cycles).

2.3 Nondestructive Evaluation Methods

Various nondestructive evaluation (NDE) techniques were used to characterize the development of damage in the specimens. Some of the techniques were performed only during initial mechanical testing while other techniques were used during intermediate fatigue stages. These

are described and discussed for the present work in the following sections.

2.3.1 X-Ray Radiography

At each intermediate fatigue stage, every specimen was radiographed using a Hewlet-Packard 43805N Faxitron, X-ray system. The X-ray source located approximately 21 inches above the specimen, was supplied with a constant voltage of 30 kV and a constant current of 2.80 ma. For additional detail, exposure times varied from 5 and 7.5 minutes for the 55% V_f specimens to 7.5 and 10 minutes for the 45% V_f specimens. Kodak M-5 X-ray film was developed in Kodak X-ray developer and prints were made on high contrast paper to enhance any variation of X-ray absorption.

To increase the probability of detecting any fatigue crack development, tetrabromoethane (TBE), which is opaque to X-rays, was used as a penetrant. To make the solution even more X-ray absorbent, a small amount of Renografin 60 was added. The penetrant was applied to the tensile side of the specimen while it was under a static load equal to 95% of the maximum fatigue load. The penetrant was allowed to soak in for approximately one minute and the load was then removed. The specimen was left overnight to allow further penetrant absorption. Excess TBE was removed from the surface of the specimen just prior to X-raying.

Each specimen was X-rayed alongside of the standard specimen previously described in Sec. 2.1. The region of FP/A1 radiographed through the holes in the aluminum plate are compared for gray level from test-to-test. This is to prevent any variation in machine performance or procedure to be misinterpreted as a change in the charac-

teristics of the specimen.

2.3.2 Ultrasonic C-Scan

Ultrasonic C-scan was another technique used to monitor the extent of damage during intermediate fatigue stages. Initial defects and fatigue damage can inhibit the ability of a material to transmit ultrasonic energy. To distinguish between initial defects and fatigue damage, a careful experimental procedure was developed so that any change would be due to material damage.

An initial pulse was generated from a 10 MHz, 1/4 inch diameter transducer. The pulse propagated through the coupling medium, water, to the top of the specimen as shown by pulse 1 in Figure 5. Pulse 1 was then partially reflected as pulse 2 and partially transmitted through the specimen as pulse 3. Because of the relatively small thickness of the specimen, internal reflections were indistinguishable from pulse 2 on the CRT display. Therefore, in order to achieve sufficient time delay of the echo, an aluminum plate was used as a reflecting surface some distance below the specimen. Careful examination of the reflecting qualities of the plate assured that the same proportion of the wave was reflected by the plate as pulse 4. Pulse 4 was then partially reflected from and transmitted through the specimen as shown by pulses 5 and 6. The amplitude of returning pulse 6 was of primary importance, and was therefore used for triggering the C-scan recording mechanism. If the amplitude of the gated pulse (pulse 6) exceeded a preset trigger level, the C-scan pen was activated and recorded a black region. Whenever the amplitude of the gated pulse fell below the selected trigger level,

the pen was turned off and a white region appeared.

To insure consistency of C-scan results, the previously described standard specimen (Sec. 2.1) was used. For each C-scan, the maximum amplitude of the gated pulse passing through the 1/4 inch (6.4 mm) hole on the standard was amplified to a level of 8 divisions on the CRT display. Several scans were run with trigger levels of 5 1/2, 6, 6 1/2, and 7 divisions on the CRT display. The different trigger levels provided a composite picture of the relative attenuation at different locations on the specimen.

A Sperry 721 Reflectoscope with pulse length always set to 1 and the filtering level constant was used to generate and receive the ultrasonic pulses. The sensitivity level was the only control varied to obtain the desired amplitude level on the echo in the standard specimen. The transducer was focused so that the beam was perpendicular to and on the top surface of the 1/2 inch thick aluminum reflecting surface without the specimen present. The focal length for the 10 MHz, 1/4 inch diameter transducer was approximately 3/4 inches. The specimen was suspended 1/4 inch above the reflecting surface so as to provide a convenient time spacing of ultrasonic pulses. The horizontal displacement of the transducer was 0.05 inches per pass across the specimen. Calibration of the system showed that this spacing provided the maximum resolution possible for the transducer used.

2.3.3 Ultrasonic Attenuation

According to Hayford and Henneke [15] the development of delaminations and transverse cracks in graphite-epoxy laminates correlates

well with a change in ultrasonic attenuation. Also, Hayford et al., [2] showed that a correlation exists between attenuation and shear strength of graphite-polyimide. Because of the successes by Hayford in polymer matrix composites, considerable effort was made to develop a consistent technique to measure ultrasonic attenuation in metal matrix composites.

The first technique tried was identical to the technique used by Hayford et al., [2]. A modified delay rod, pulse-echo technique with a 5 MHz, 1/2 inch diameter transducer was used. A fused quartz rod was used as a delay block to provide ample spacing of ultrasonic pulses on the cathode ray oscilloscope. Ultrasonic attenuation was then calculated by a technique which compensated for any attenuation generated by the block-transducer coupling agent [2]. A fixture was developed to aid in consistently measuring attenuation over the length of a specimen. The fixture consisted of a guide which enabled accurate and repeatable transducer positioning at twelve locations along the specimen. The attenuation of each section was measured five times and then averaged to give the average attenuation at each point along the specimen.

The second technique involved the use of a 1/4 inch, 10 MHz transducer operating in a standard pulse-echo mode (i.e., no delay block). Due to smaller diameter and higher frequency this transducer provided better resolution of the pulses. The attenuation was calculated by comparing the amplitude of the first and third returning pulses. This method was used for all tests performed during static loading. Also this technique was used to measure attenuation initially and during each intermediate fatigue stage. The transducer was centered on the central load point and placed so that it was flush with the tensile edge of

the specimen.

Other techniques such as pitch-catch and the use of shear waves were attempted with little success. Also, the transmission of ultrasonic pulses through the length and width of the specimen was tried. However, the only direction which provided sufficient specimen-transducer coupling was the transmission of ultrasonic pulses through the thickness of the specimen.

2.3.4 Thermography

Surface thermal patterns resulting from the dissipation of thermal energy were monitored with real-time thermography using an AGA thermographic camera, model 680. Vibro-thermography was performed on specimens attached to an ultrasonic shaker vibrating at frequencies between 10 and 30 KHz. Real-time video-thermography was also performed on specimens during fatigue testing. Thermal patterns can be caused by strain energy release or by the rubbing together of internal surfaces such as cracks or delaminations. To eliminate thermal reflections and have a uniform surface emissivity, each specimen was painted with flat-black spray paint.

2.3.5 Replication

Replication here refers to the process of making a surface impression of a specimen on acetone-softened acetate film. Replicas which will locate a surface crack can be taken of a material under load. In this study, replicas were taken during axial tests at 40 ksi load and during bend tests at 20 lbs. less than the maximum fatigue load. The limitation of replication is evident. Only exposed surfaces can be

examined. However, replication offers a quick, inexpensive and permanent record of the surface of the specimen.

2.3.6 Stiffness Change

According to O'Brien [16] (boron-epoxy) and Dvorak [17] (boron aluminum) stiffness change is a good indication of damage development in composite materials. Therefore careful stiffness measurements were made to determine if stiffness reduction correlates with the development of damage in the material. Both axial modulus and flexural rigidity were taken initially and during each intermediate fatigue stage.

Flexural rigidity was calculated from the slope of a secant line in the load-deflection curve. To provide consistent measurements, the secant line was bounded by the minimum and maximum fatigue loads. The slope of the secant line was then substituted for P/Δ in equation (4).

Axial modulus was also measured using the slope of the secant line between 0 and 40 ksi. To insure repeatability, considerable care was used to mount the extensometer in the same manner and location during each axial stiffness measurement. The strain reading was taken over a one inch gauge length centered about the central load point during bend testing.

One specimen of each volume fraction was tested to failure under cyclic loading while monitoring only the flexural rigidity. These specimens were used to examine the correlation between cyclic and static measurements and to eliminate idiosyncrasies in the test procedure that might prevent good flexural rigidity results.

There was a certain difficulty that occurred during all bend tests in which a virgin specimen was loaded. A small amount of permanent deformation occurred around all load points. Therefore, the stroke did not return to the starting point, making the initial modulus calculations difficult. To overcome this problem, several quasi-static load cycles were performed. After this, the material no longer underwent significant permanent deformation and the initial stiffness measurement could be taken from an elastic curve. Therefore, when examining initial load-deflection curves such as Figure 9, consideration of the local deformation must be made.

Another precaution taken to ensure accuracy during all static stiffness measurements was that no reading was accepted if permanent deformation occurred.

2.3.7 Eddy Current

Using a Nortec model NDT-3 eddy current instrument, which operates at 100K Hz the reactance and resistance of FP/Al composite specimens were measured. A 1/4 inch diameter pencil probe (Nortec Model 3550) was used to generate the eddy currents. A technique was established for monitoring the damage created by bending fatigue. Initial values of reactance and resistance were measured at six locations along the specimen. Readings were also taken at the same locations after intermediate stages of fatigue. From Table 1 it can be seen that the reactance and resistance cannot be effectively measured near the specimen edge. For this reason, a fixture to hold the probe a minimum distance of 2 mm from the edge of the specimen was constructed. Measurements were taken at three locations 2 mm from the tensile edge on both sides of the specimen.

Table 1: Values of resistance (R) and reactance (X) across the width of FP/A1.

Distance from Edge (mm)	Specimen 17/4		Specimen 23/5	
	X	R	X	R
Air	5.67	5.37	5.61	5.36
0.0	5.53	5.62	5.48	5.50
0.5	5.49	5.74	5.39	5.88
1.0	5.44	5.80	5.36	5.91
1.5	5.38	5.95	5.35	5.92
2.0	5.36	5.96	5.32	5.96
2.5	5.33	5.97	5.32	5.95
3.0	5.31	5.95	5.31	5.95
3.5	5.30	5.97	5.30	5.96
4.0	5.29	5.98	5.31	5.98
4.5	5.28	6.00	5.30	5.99
5.0	5.27	6.01	5.30	5.99
5.5	5.27	6.02	5.29	5.99
6.0	5.28	6.03	5.29	5.99
6.5	5.26	6.04	5.28	6.00
7.0	5.24	6.04	5.30	5.99
7.5	5.22	6.07	5.31	5.99
8.0	5.21	6.08	5.30	6.00
8.5	5.26	6.05	5.31	6.00
9.0	5.21	6.12	5.30	5.99
9.5	5.21	6.15	5.31	5.97
10.0	5.22	6.16	5.33	5.94
10.5	5.24	6.18	5.38	5.88
11.0	5.28	6.20	5.46	5.83
11.5	5.36	6.15	5.53	5.70
12.0	5.53	5.90	5.60	5.58
12.5	5.53	5.61		

Width of specimen 17/4 is 12.6 mm. Width of specimen 23/5 is 11.7 mm.

The locations were at the center load point and 5 mm on each side of this load point.

2.3.8 Acoustic Emission

It has been shown by Henneke, et al., [7] among others, that increases in acoustic emission correspond to damage initiation or development in composite materials. Matrix cracking, matrix plasticity, fiber breakage, fiber-matrix debonding, delamination growth or any combination of the above, are possible sources of acoustic emission in composites. The important thing to note is that acoustic emission indicates local energy release due to loading inside the specimen.

For all acoustic emission tests, the same set-up used by Henneke, et al., [7] was employed. Signals detected by the piezoelectric transducer were sent into a signal amplifying system where high (> 300 KHz) and low (< 10 KHz) frequencies were filtered out. The amplified signal (approximately 80 dB amplification) was then transferred to a signal analyzer where the number of counts exceeding a pre-set trigger level was counted. The trigger level was carefully chosen to eliminate all background noise. Stopcock grease was used as a coupling agent between the specimen and the transducer which were securely held in contact by several rubber bands.

2.4 Test Procedure

The objective of the test program was to characterize initial defects, initiate damage by loading the specimen, characterize the damage by NDE, initiate more damage or cause it to grow by additional loading, and so on. In particular the following sequence was followed:

1. Initial Nondestructive Evaluation
 - X-ray radiography
 - C-scan
 - Eddy current
 - Ultrasonic attenuation
2. Initial Axial Testing
 - Acoustic emission monitored (0-70 ksi)
 - Ultrasonic attenuation monitored (0-70 ksi)
 - Axial modulus measured (0-40 ksi)
 - Replication performed (40 ksi)
3. Bend Testing (all tests performed within the fatigue load range)
 - Acoustic emission monitored
 - Ultrasonic attenuation monitored on tension and compression sides of the specimen
 - Initial flexural rigidity measured
 - Fatigue testing to 10K cycles
 - Final flexural rigidity measured
4. Damage Characterization
 - X-ray radiography with penetrant
 - C-scan
 - Eddy current
 - Ultrasonic attenuation
 - Axial modulus measured (0-40 ksi)
 - Replication performed (40 ksi)

5. Further Bend Testing

- Flexural rigidity prior to fatigue increment
- Fatigue testing to next increment
- Flexural rigidity after fatigue increment

6. Steps 4 and 5 are repeated until fracture

The fatigue tests were interrupted at the levels 10K, 50K, 100K, 150K, 250K, 400K, 600K, 800K and 1000K cycles in order for the NDE tests to be performed. If the specimen had not failed by 1000K cycles of loading, it was failed quasi-statically after the final damage characterization.

2.5 Notched Specimens

Several specimens were notched to create a large stress concentration in a localized region. This was done to examine transverse crack growth in the material during loading, to further localize the region where damage may occur and to determine the effects of large normal and shear stresses near the ply interfaces. Figure 6 shows the geometry of the notch. The notch depth (a) and test performed on each notched specimen are given in Table 2. To determine the strength reduction created by the notch, one specimen of each volume fraction was loaded quasi-statically to failure. Then, the other specimens were fatigued 10K cycles at a time at increasing load increments as given in Table 3.

After cycling the first pair of specimens (21/4 and 21/5) to failure, the effects of notch depth were investigated. Two pairs of specimens (12/5, 23/5 and 16/4, 17/4) with different notch depths were fatigued at loads corresponding to the same stress intensity factor (K_I). For example, the initial load for specimen 12/5 was 87 pounds and the

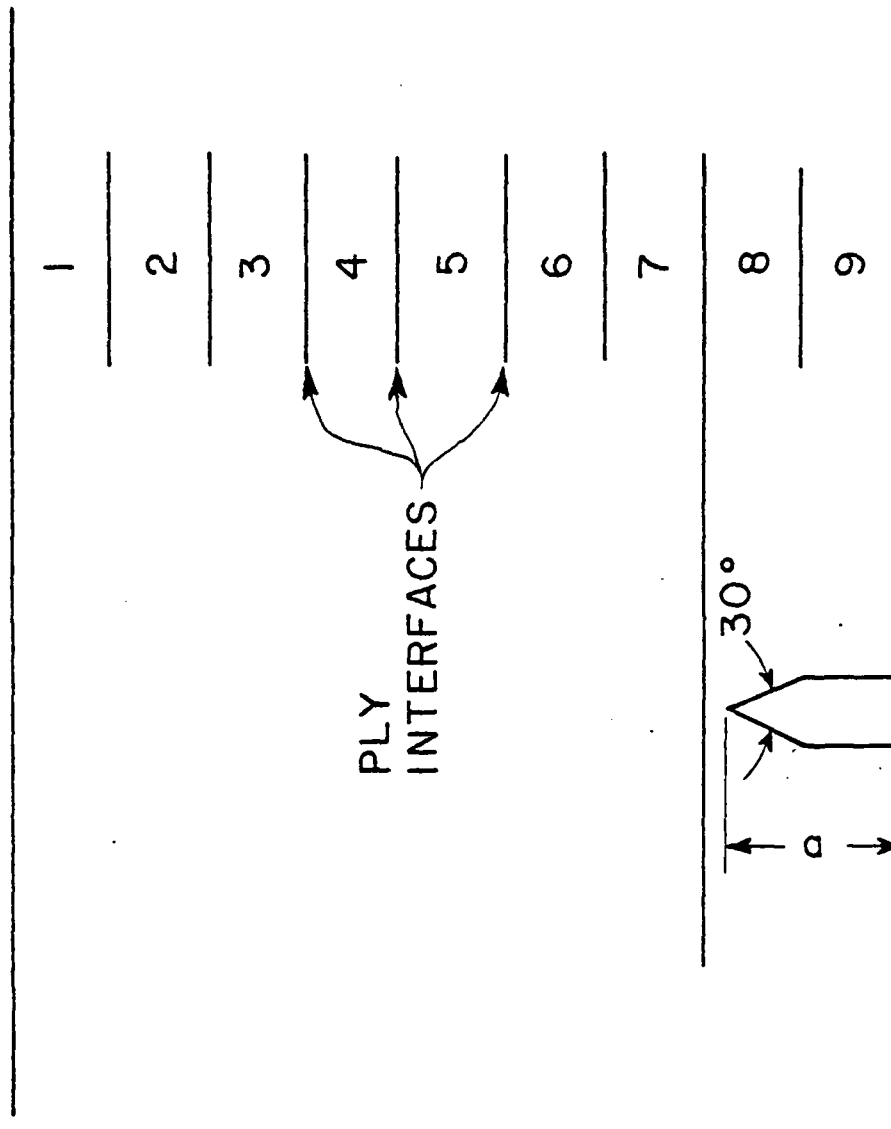


Figure 6: Geometry of the notch

Table 2: Notch depth, normalized stress intensity factor and tests performed on notched specimens.

Specimen	a (in.)	K_I/P (in.) ^{-3/2}	Test Performed
12/5	.060	345.7	fatigue
20/5	.090	428.2	static
21/5	.090	428.2	fatigue
23/5	.090	428.2	fatigue
16/4	.100	389.5	fatigue
17/4	.065	309.7	fatigue
20/4	.100	389.5	static
21/4	.100	389.5	fatigue

Table 3: Test matrix of fatigue load increments

Specimen K Cycles	Maximum Fatigue Load (Lbs.)					
	12/5	23/5	21/5	16/4	17/4	21/4
10	87	70	75	70	88	75
20	99	80	80	80	101	80
30	112	90	85	90	113	85
40	124	100	90	100	126	90
50	136	110	95	110	138	95
60	149	120	100	120	151	100
70	161	130	105	130	163	105
80	173	140	110	140	176	110
90	186	150*	120	150	189	120
100	198		130	160	201	130
110	211		140	170	214	140
120	223*		150*	180	226	150
130				190	239	160
140				200*	252*	170
150						180
160						190
170						200
180						210*

*Failure occurred at this load increment

initial load for specimen 23/5 was 70 lbs., which made the common value of K_I equal to 30 ksi (in)^{1/2}. The stress intensity factors were calculated from the following expression for a notch under pure bending [18].

$$K_I = F \cdot \frac{6 M a^{1/2}}{b h^2} \quad (5)$$

where:

$$F = 1.99 - 2.47 \left(\frac{a}{h} \right) + 12.97 \left(\frac{a}{h} \right)^2 - 23.17 \left(\frac{a}{h} \right)^3 + 24.80 \left(\frac{a}{h} \right)^4$$

For each specimen the normalized stress intensity factor (K_I/P) is given in Table 2.

The NDE performed on these specimens consisted of X-ray radiography, C-scan and replication. For specimens 21/4 and 21/5 X-ray radiography was performed at every intermediate fatigue stage, replication was performed at fatigue loads after a crack was detected and ultrasonic C-scan was performed initially and after fatigue loading at 100 and 190 pounds. The other specimens (16/4, 17/4, 12/5, 23/5) were replicated at each fatigue stage and X-rayed and C-scanned at every alternate fatigue stage.

3. RESULTS

3.1 Mechanical Tests

Table 4 gives a complete list of specimens and the test performed on each. "Static" tests indicate tests where the load was increased until failure occurred. Fatigue tests include NDE at intermediate stages as described in the previous chapter.

3.1.1 Axial Tension Tests

Axial quasi-static tension tests were performed to characterize the material properties. Figure 7 shows a typical stress-longitudinal strain plot with a plot of transverse strain versus longitudinal strain superimposed. This plot is typical of the behavior found in both volume fractions. FP/A1 behaved in a linear fashion until apparently the matrix yield point was reached. After the yield point, the axial modulus E_A gradually decreased until failure. Similar behavior was found in the Poisson's ratio. An initial value, a sudden change then a gradual increase in the value of Poisson's ratio (ν) was recorded. It is important to note that the change occurs at approximately the same stress in both plots.

Table 5 gives values for the modulus, E_A , Poisson's ratio, ν and the yield strength, σ_{YP} , along with the values of ultimate stress, σ_{ULT} , ultimate strain, $(\epsilon_L)_{ULT}$ and $(\epsilon_T)_{ULT}$, modulus, $(E_A)_{ULT}$, and Poisson's ratio, ν_{ULT} , which occurred at failure. The large discrepancy in the strength of specimens 9/5 and 10/5 is believed to have been caused by the gripping mechanism since specimen 10/5 failed well within the grips.

During the axial tests initially performed on the fatigue speci-

Table 4: Test Matrix

<u>Specimen</u>	<u>Test Performed</u>
4/5	Fatigue (240 lbs.)
5/5	Fatigue (240 lbs.)
6/5	Fatigue (270 lbs.)
7/5	Fatigue (285 lbs.)
8/5	Static Bend Test
9/5	Static Axial Test
10/5	Static Axial Test
11/5	Stiffness Fatigue (255 lbs.)
12/5	Notch Fatigue
13/5	Static Bend Test
14/5	Fatigue (240 lbs.)
15/5	Fatigue (240 lbs.)
16/5	Fatigue (240 lbs.)
17/5	Fatigue (255 lbs.)
18/5	Fatigue (255 lbs.)
19/5	Flaw Fatigue
20/5	Notch Static
21/5	Notch Fatigue
22/5	Standard
23/5	Notch Fatigue
2/4	Fatigue (280 lbs.)
3/4	Fatigue (280 lbs.)
4/4	Fatigue (280 lbs.)
5/4	Static Bend Test
6/4	Static Axial Test
7/4	Fatigue (280 lbs.)
8/4	Fatigue (260 lbs.)
9/4	Fatigue (260 lbs.)
10/4	Fatigue (260 lbs.)
11/4	Fatigue (240 lbs.)
12/4	Fatigue (240 lbs.)
13/4	Fatigue (240 lbs.)
14/4	Not Tested
15/4	Stiffness Fatigue
16/4	Notch Fatigue
17/4	Notch Fatigue
18/4	Static Bend Test
19/4	Static Axial Test
20/4	Notch Static
21/4	Notch Fatigue
22/4	Standard

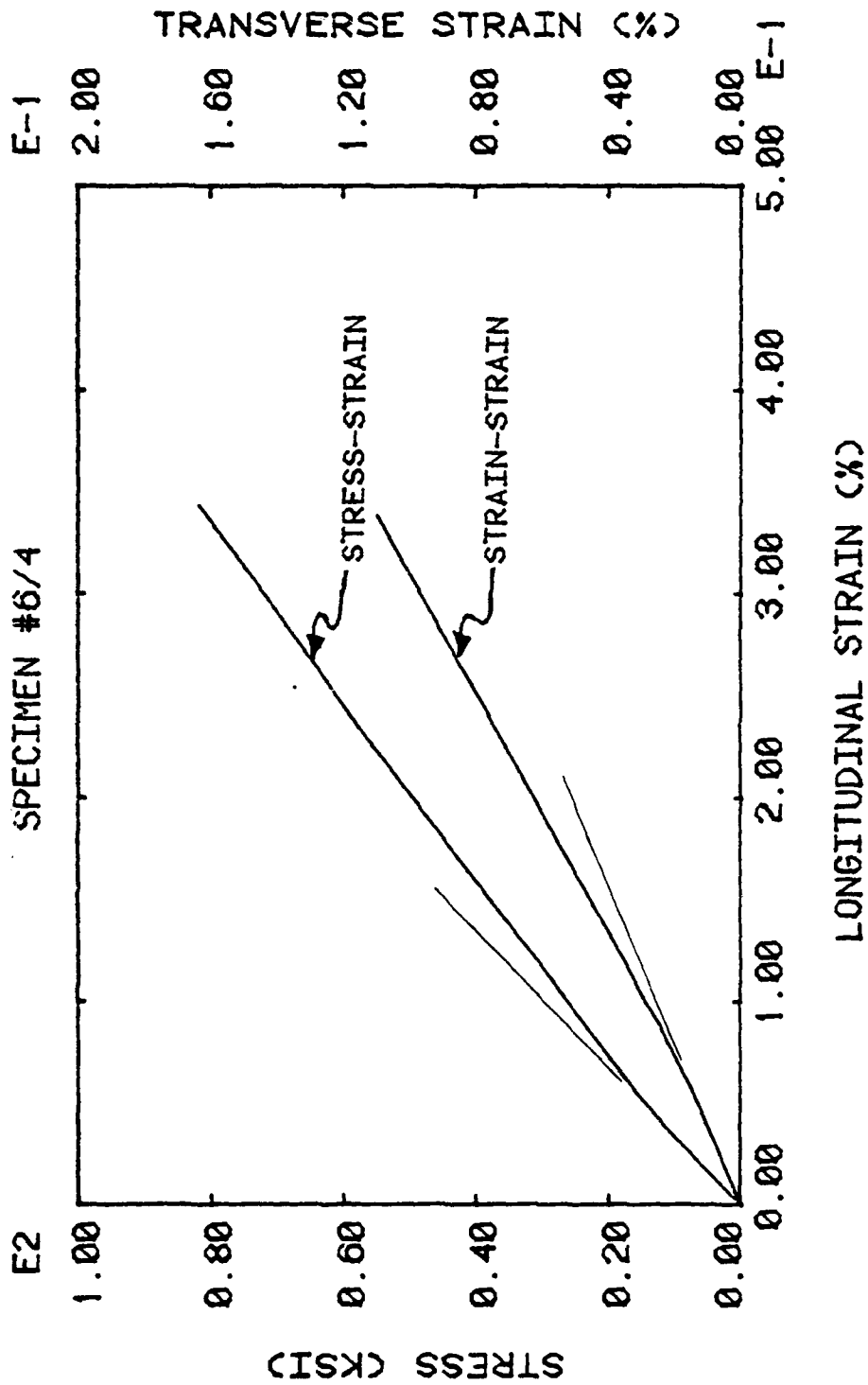


Figure 7: Stress and Transverse Strain versus Longitudinal Strain for Tension Test.

Table 5: Quasi-Static Tension Test Results

Property/Specimen No.	6/4	19/4	9/5	10/5
E_A (Msi)	29.2	30.2	30.9	29.8
$(E_A)_{ULT}$ (Msi)	20.1	22.1	20.8	20.7
ν	0.26	0.28	0.23	0.25
ν_{ULT}	0.33	0.43	0.33	0.36
σ_{yp} (Ksi)	12.4	11.5	12.9	17.2
σ_{ULT} (Ksi)	82.0	81.7	93.4	77.3
$(\epsilon_L)_{ULT}$ (μ in/in)	3550	3450	3280	2940
$(\epsilon_T)_{ULT}$ (μ in/in)	-1120	-1420	-980	-1030

mens, similar stress-strain behavior was recorded. That is, an initial linear region was followed by a nonlinear region up to the maximum applied load. However, after this first loading, the material behaved linearly elastic for all subsequent axial tests. These tests indicate that the behavior of 45% and 55% V_f FP/Al is strongly influenced by the matrix material. The yield point for the aluminum matrix is approximately 6 ksi. Therefore, assuming the matrix modulus is 10 Msi, the strain at the onset of matrix plasticity is 0.06%. Assuming an axial modulus of 30 Msi for the FP/Al composite specimens the rule of mixtures predicts the approximate yield strength of the composite to be 18 ksi. Thus, the knee in the stress-strain curve corresponds to yielding of the aluminum matrix.

3.1.2 Static Bend Tests

Static bend tests were used to determine the flexural characteristics of FP/Al. Figure 8 shows an applied moment-strain plot for the point located at the midspan and at the outer edge of the specimen. This point is subjected to the maximum bending moment and hence for this case has the maximum tensile stress. The outer edge strain is recorded by a strain gauge, while the applied moment is equal to $PL/4$. Similar to the axial stress-strain plots, this plot has an initial linear range that becomes nonlinear as the stiffness gradually decreases. Figure 9, a typical initial (bending) load-deflection curve, again shows a region of constant stiffness, followed by a non-linear region indicating stiffness decrease.

Table 6 gives the ultimate values of load (P_{ULT}), strain (ϵ_{ULT}),

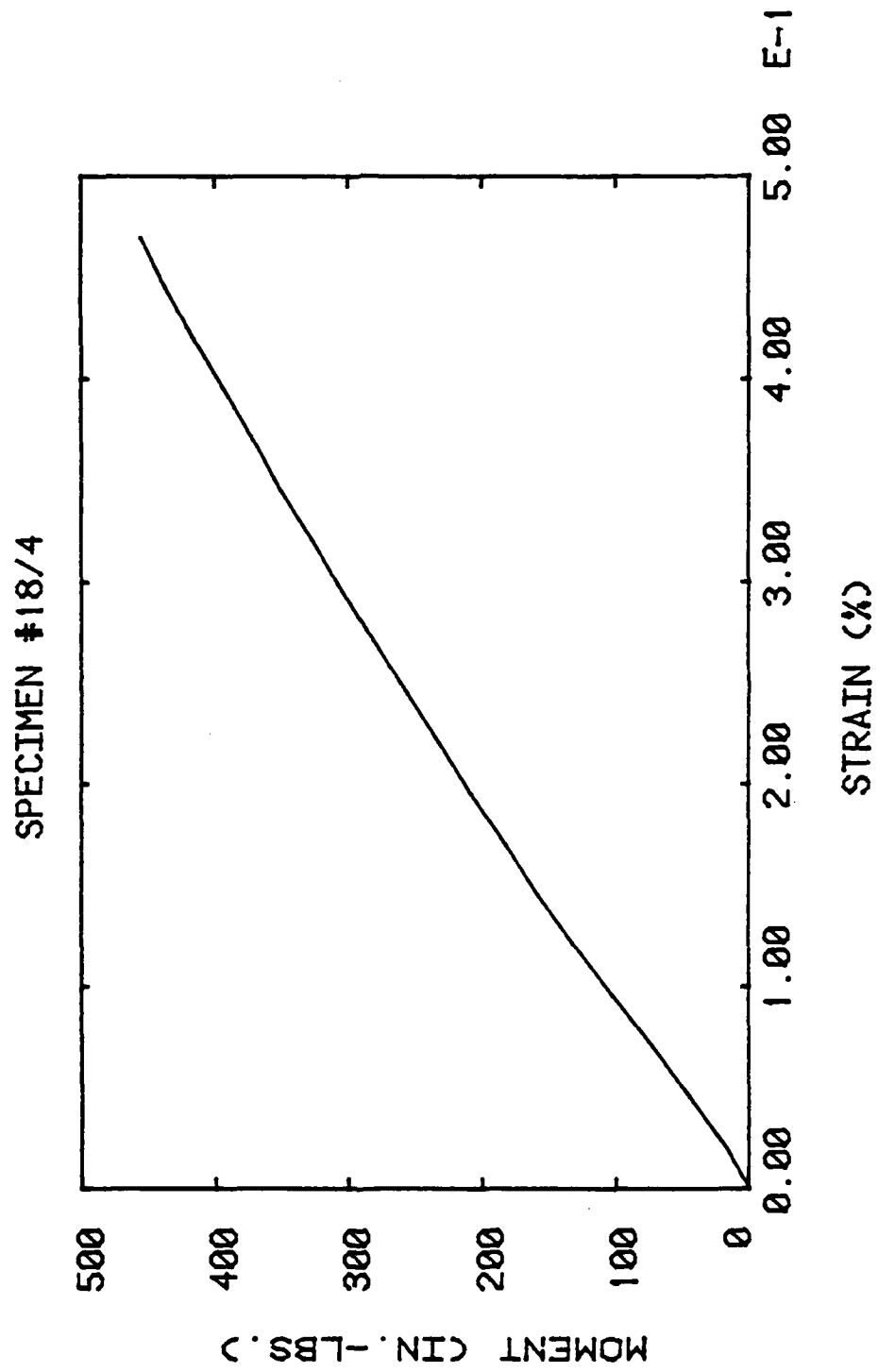


Figure 8: Maximum Moment versus Strain during Bend Test

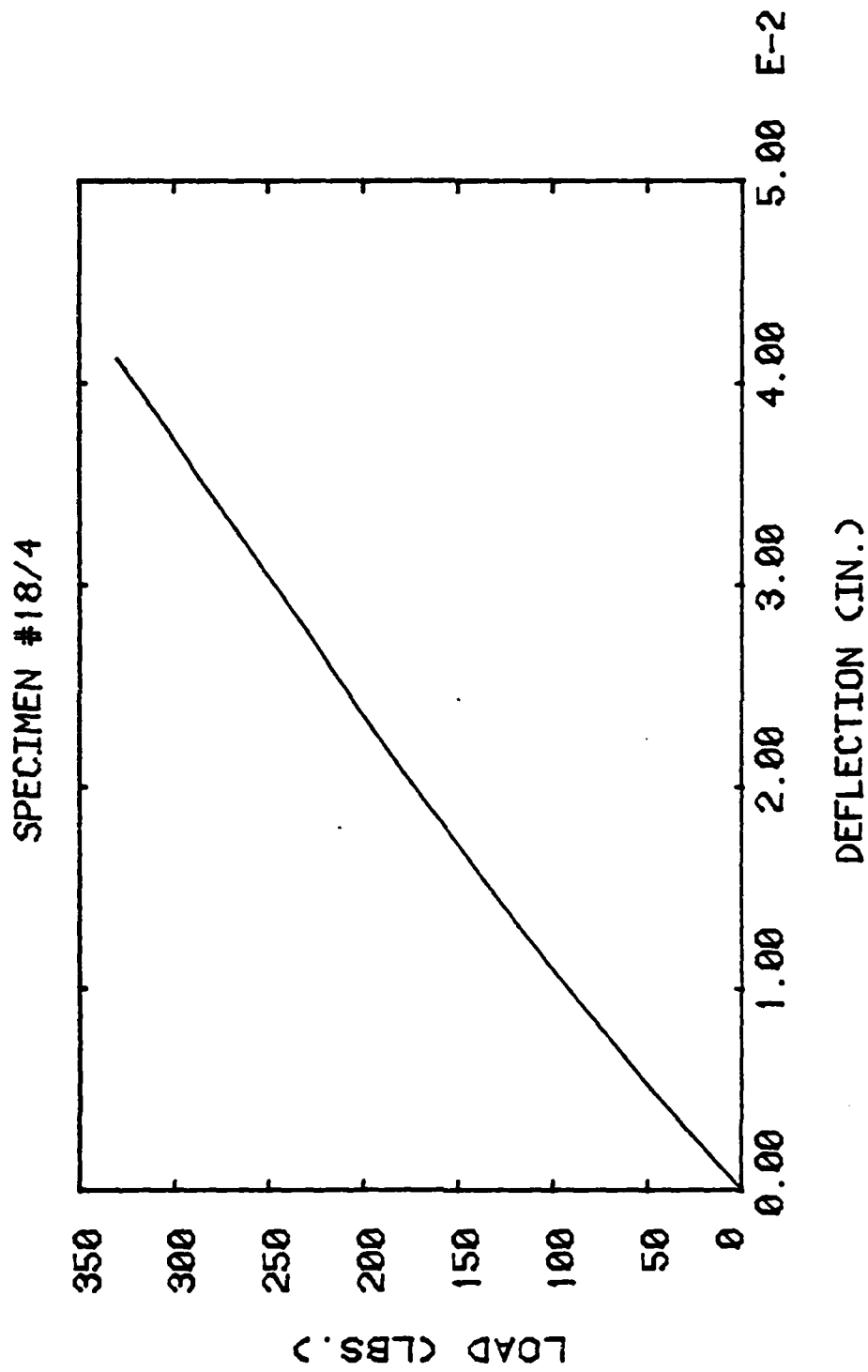


Figure 9: Load versus Deflection for Bend Test.

deflection (Δ_{ULT}) and moment (M_{ULT}) for all specimens that underwent quasistatic bend tests to fracture. Also, the location of fracture point (FL), the fracture point moment (M_{FL}) and the modulus of rupture (σ_R) are given. FL represents the distance between the central load point and the fracture point.

It is important to recall that the modulus of rupture is not the actual stress at the failure location but an approximate value assuming that the stress-strain curve behaves linearly. However, for the first load cycle the stress-strain curve does not behave linearly, therefore the modulus of rupture is not the actual stress at the failure point for quasi-static bending tests.

3.1.3 Fatigue Tests

A complete listing of the results of fatigue testing is given in Table 7. The maximum fatigue load, cycles to failure, failure point location and the modulus of rupture are given. Note that after a few load cycles the material behaved linearly, therefore the modulus of rupture is approximately the same as the failure point stress for fatigue specimens. Figure 10 gives a plot of the approximate value of the modulus of rupture versus the number of cycles to failure. Where the stress was greater than 85 ksi, a large number of early failures occurred. However, the three specimens that were tested below 80 ksi lasted 400K cycles before a residual strength bend test was performed. The residual strengths were 346, 348 and 310 pounds for specimens 11/4, 12/4 and 13/4 respectively. This indicates (Table 6) that after 400K cycles at 240 pound maximum fatigue load, these specimens were not

Table 6: Quasi-Static Bend Test Results

<u>Property/Specimen No.</u>	<u>5/4</u>	<u>18/4</u>	<u>8/5</u>	<u>13/5</u>
P_{ULT} (lbs.)	367	342	315	292
ϵ_{ULT} (μ in/in)	*	4350	4350	4680
Δ_{ULT} (in)	0.0535	0.0465	0.0480	0.0485
M_{ULT} (in-lbs.)	504	470	433	402
FP (in)	0.41	0.00	0.06	0.03
M_{FP} (in-lbs.)	428	470	424	397
σ_R (Ksi)	102.8	112.6	117.8	110.5

*Gauge Failure

Table 7: Fatigue Test Results

Specimen Number	Maximum Fatigue Load (lbs)	Cycles to Failure (K)	Failure Location (in)	Modulus of Rupture (Ksi)
5/5	240	24	0.05	90.1
6/5	270	100	0.29	92.4
7/5	285	29	0.12	103.1
14/5	240	50*	0.15	86.8
15/5	240	486	0.16	86.5
16/5	240	1028	0.00	91.8
17/5	255	3.5	0.10	94.0
18/5	255	4.8	0.00	97.5
2/4	280	26	0.14	87.5
3/4	280	90	0.00	92.2
7/4	280	31	0.09	84.1
8/4	260	50	0.05	84.1
9/4	260	150	0.00	85.6
10/4	260	250**	0.00	85.6
11/4	240	400*	0.21	73.0
12/4	240	400*	0.05	77.6
13/4	240	400*	0.08	76.7

*Residual Strength Measurement

**Load Exceeded During Stiffness Measurement

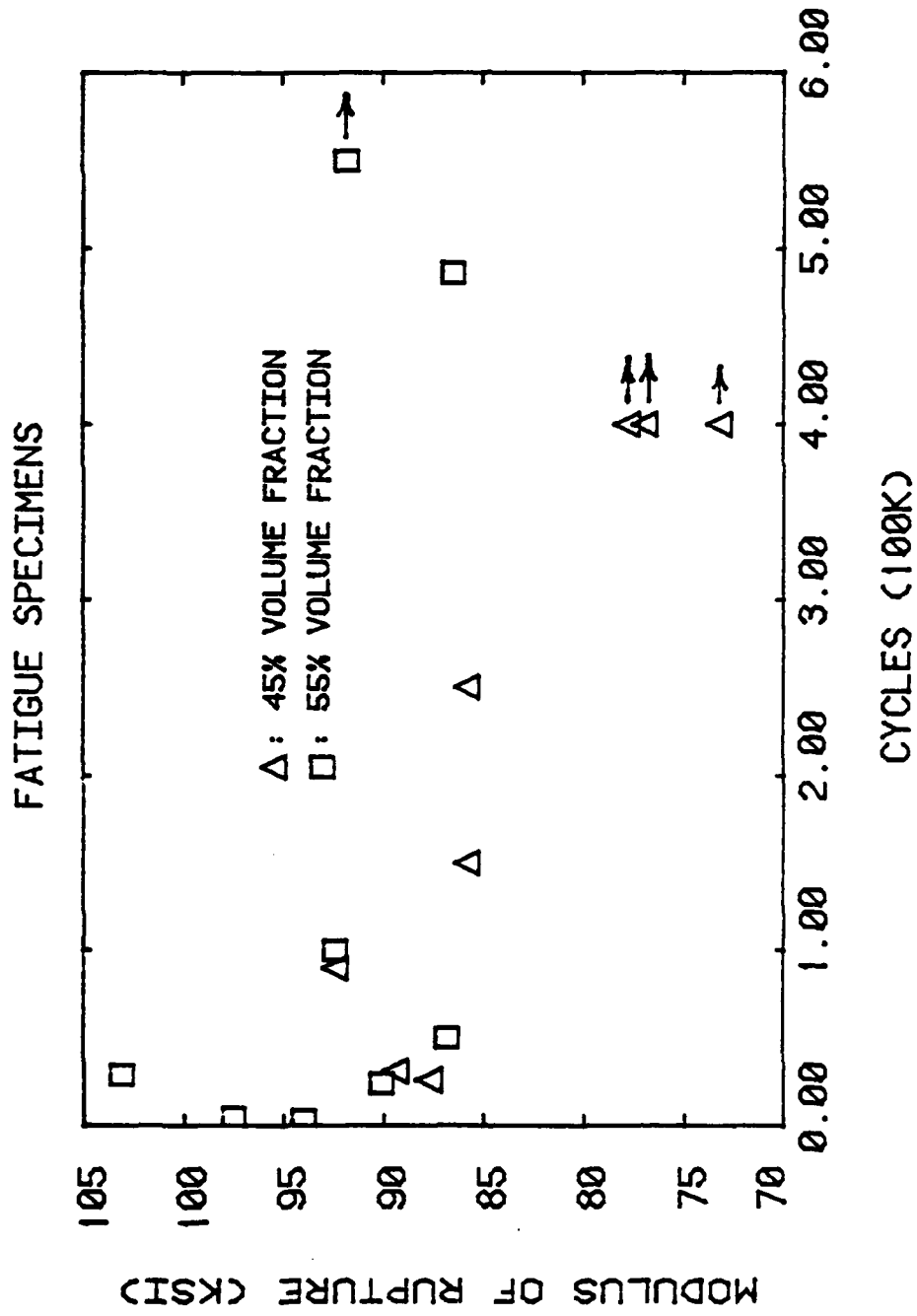


Figure 10: Modulus of Rupture versus the Number of Cycles to Failure.

substantially weakened. The point farthest to the right is specimen 16/5 which failed after 1028K cycles at a maximum fatigue load of 240 pounds.

Other specimens whose tests are worthy of note are specimens 4/5, 4/4 and 8/4. Specimen 4/5 twisted sideways in the bend fixture during static preload and broke at 236 pounds. After this occurred, the bend fixture was modified to prevent this mode of failure. After withstanding two initial 70 ksi tests, specimen 4/4 failed under a quasi-static tension load of 40 ksi during the initial replication process. As in specimen 10/5 this failure occurred well inside the grips and is believed to have been partially caused by the gripping mechanism. After 50K cycles, specimen 8/4 broke during the axial stiffness measurement; this failure was caused by damage created at the load point.

3.2 Evaluation of NDE Results

3.2.1 X-Ray Radiography

X-ray radiography indicated the presence of several interesting characteristics. From examination of Figure 11 several things are immediately evident. Near the top of each specimen a region that impedes the transmission of X-rays (i.e., the dark area) exists. This region is believed to have been caused by the matrix injection process during the manufacture of the material. The presence of longitudinal striations along the entire length of the specimen is also evident. The striations appear more distinct in the 55% V_f than in the 45% V_f specimens. Again, it is believed that manufacturing processes caused this characteristic. In particular, it is believed that these striations are related to the original plies of material that were laid up to form

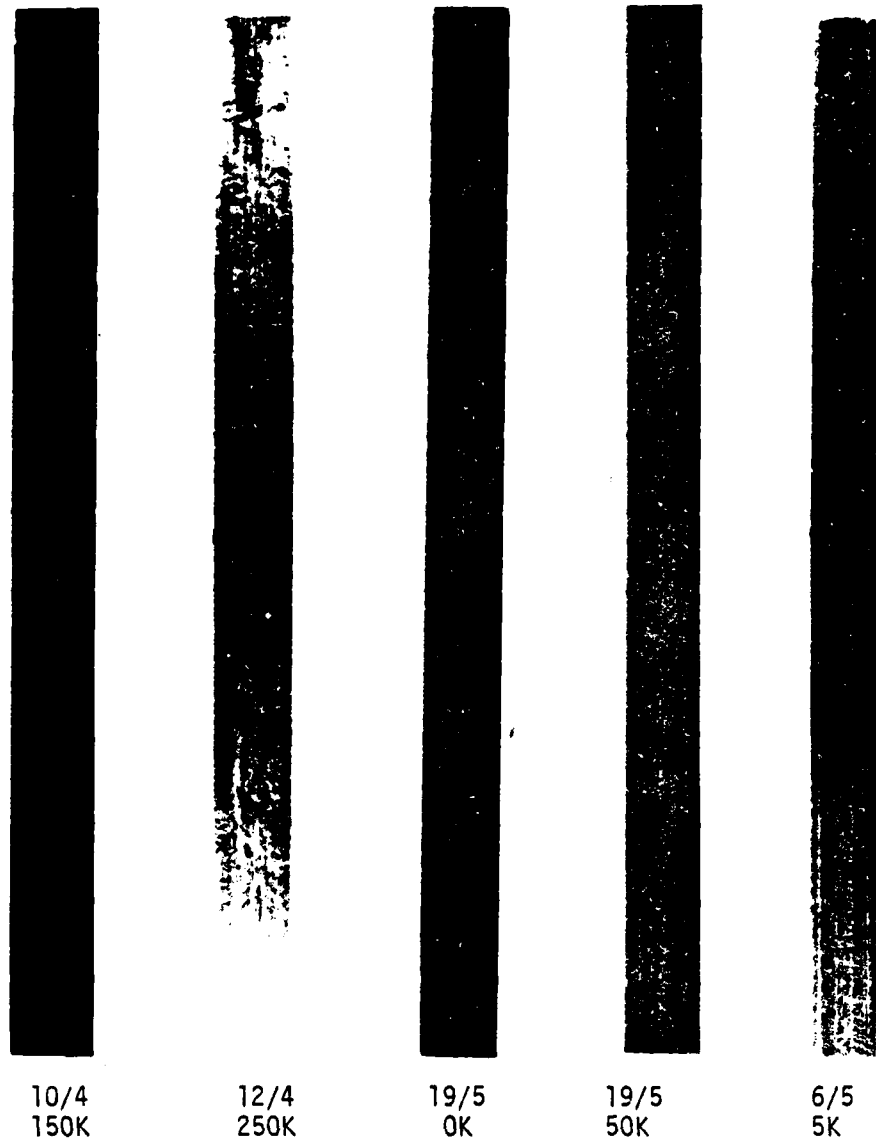


Figure 11: Typical X-ray radiographs of specimens after fatigue loading to indicated number of cycles.

the laminate prior to matrix injection. Finally, damage created by the load points is evident.

Approximately 1/4 inch below the central load point on specimen 19/5, a manufactured flaw was detected on the radiographs. Radiographs of this flaw are shown in Figures 11 and 12. Similar flaws were detected in other specimens but never in a region near the maximum tensile stress induced by bend testing. Therefore, a special test was developed for specimen 19/5. Fifty thousand cycles of loading were performed at each of three load levels (200, 220 and 240 pounds) before failure occurred at 256 pounds during a static preloading. Figure 12 gives the location of failure with respect to the central load point. Notice that failure occurred at the end of the flaw which was subjected to the maximum tensile stress. After failure, specimen 19/5 was sectioned to characterize and to observe the flaw under a microscope. The flaw was determined to be a region void of matrix.

Besides the local deformation under the load points, only in one fatigue test was any other damage detected by X-ray radiographs. Two radiographs of specimen 11/4 are given in Figure 13. After 400K cycles a small dark spot appeared at the exact location of the final failure. This spot does not appear in or before the 250K cycle radiograph. Penetrant is believed to have entered a surface exposed matrix void making the spot observable. The matrix void was probably opened to the surface by the formation of a small matrix fatigue crack.

It should be noted that the radiograph width is slightly narrower than the specimen. Each edge of the specimen diffracts the X-rays creating an over-exposed region underneath the edge. Therefore, any

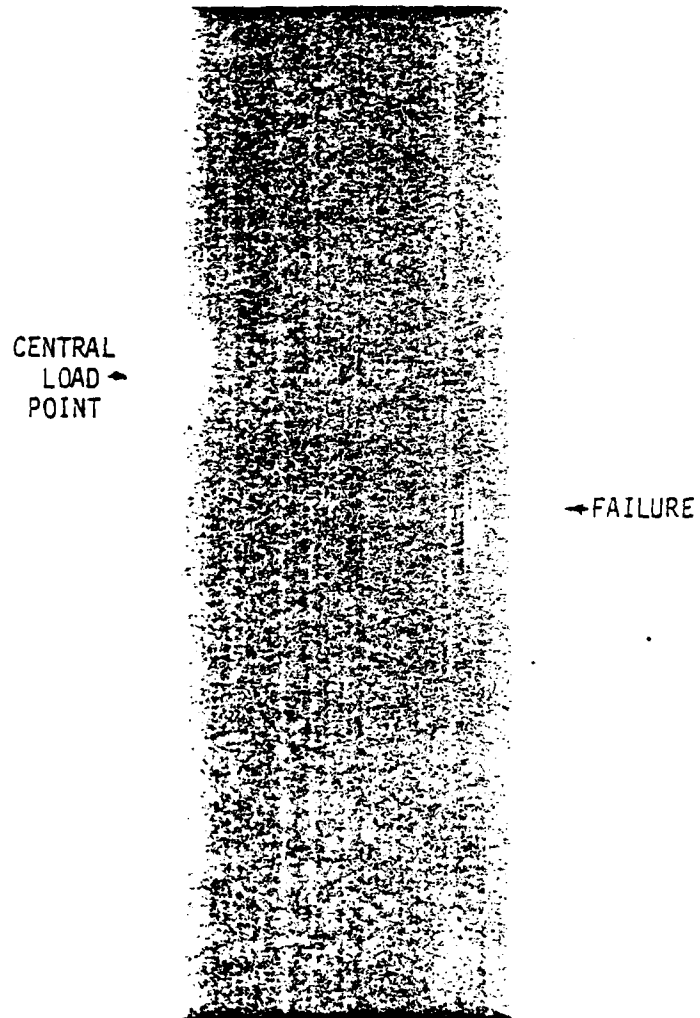
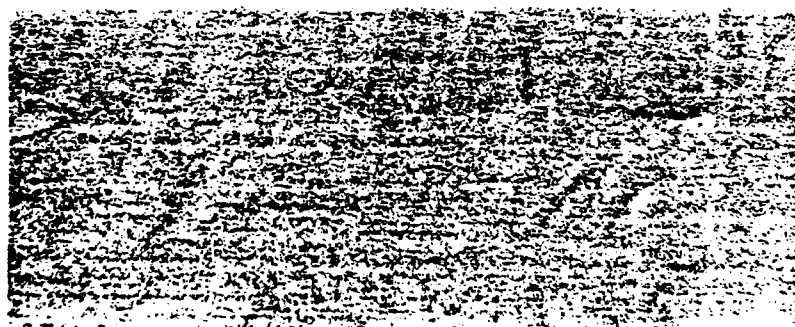


Figure 12: Enlarged Radiograph of the Flaw in specimen 19/5



250K

↑
Load Point

Failure Location
↓



400K

↑
Load Point

Figure 13: X-Ray of Specimen 11/4 after 250K and 400K cycles of Fatigue.

fatigue crack near the specimen edge cannot be detected by this method.

3.2.2 Ultrasonic C-Scan

Results similar to the initial radiographs were found in the initial C-scans. Longitudinal striations such as seen in Figure 14 were evident to some degree in all specimens. Figures 15 and 16 show a comparison between X-ray radiograph and C-scan results. Comparing the top of specimen 11/5, shown in Figure 15, it is evident that the region of X-ray absorption previously discussed also attenuates ultrasonic waves. In addition, towards the bottom of specimen 11/5 a region of matrix void is apparent by both NDE methods. Similarly, in Figure 16 the matrix void (shown in the radiograph in Figure 12) can be seen in the C-scan. It should be noted that the top of specimen 19/5 does not absorb X-rays or ultrasonic waves to the degree found in specimen 11/5. It was verified that the flaw in specimen 19/5 was indeed a matrix void by the process of sectioning and observation of the flaw under a microscope.

It is interesting to note that where large matrix voids existed, no ultrasonic pulse propagated through the specimen. This indicates the presence of a region of very high ultrasonic attenuation. On the radiograph, the corresponding light region indicates that fewer X-rays were absorbed. This is not surprising because when compared to FP/A1, the void, even if it contains air, is a very poor medium for transmission of ultrasonic waves but absorbs relatively few X-rays. Hence, by comparing the radiographs to the C-scans, voids can be identified in FP/A1.

Some damage development was detected by ultrasonic C-scan. The

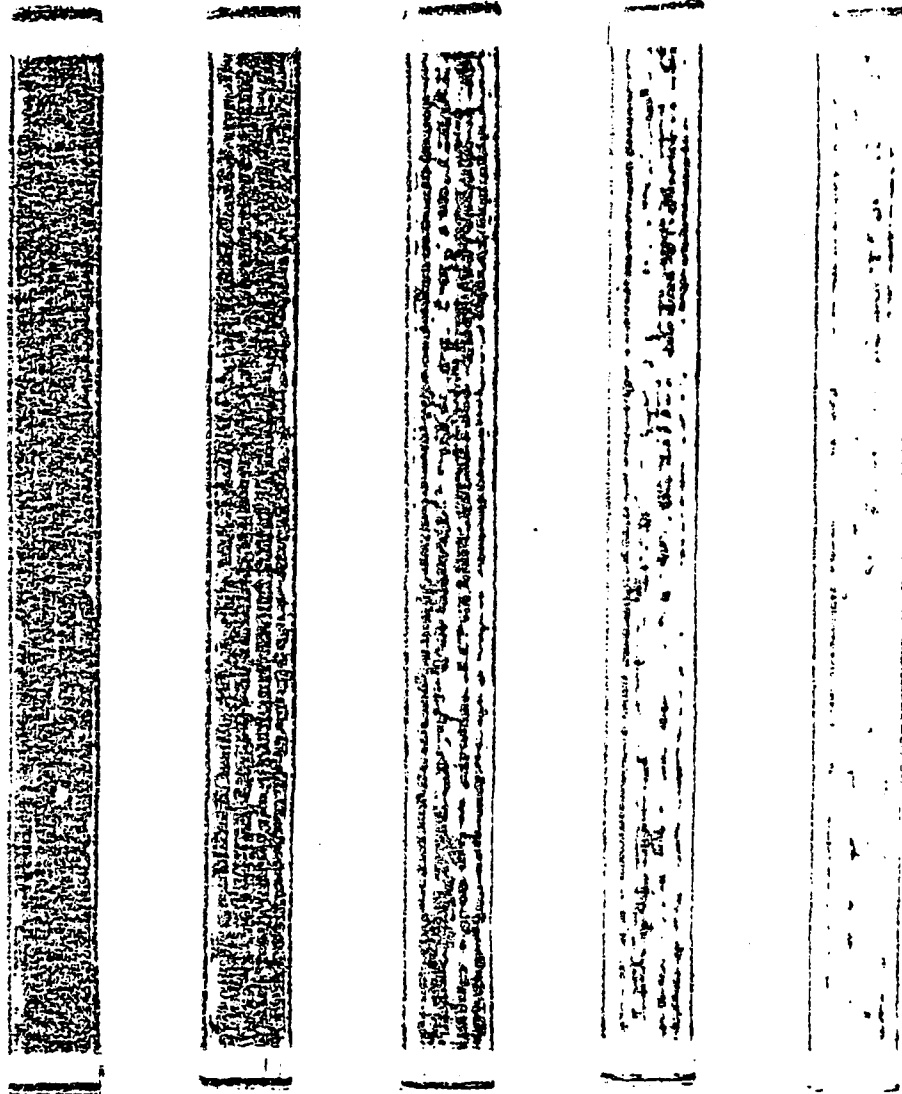


Figure 14: C-scans of specimen 14/4 showing longitudinal striations.

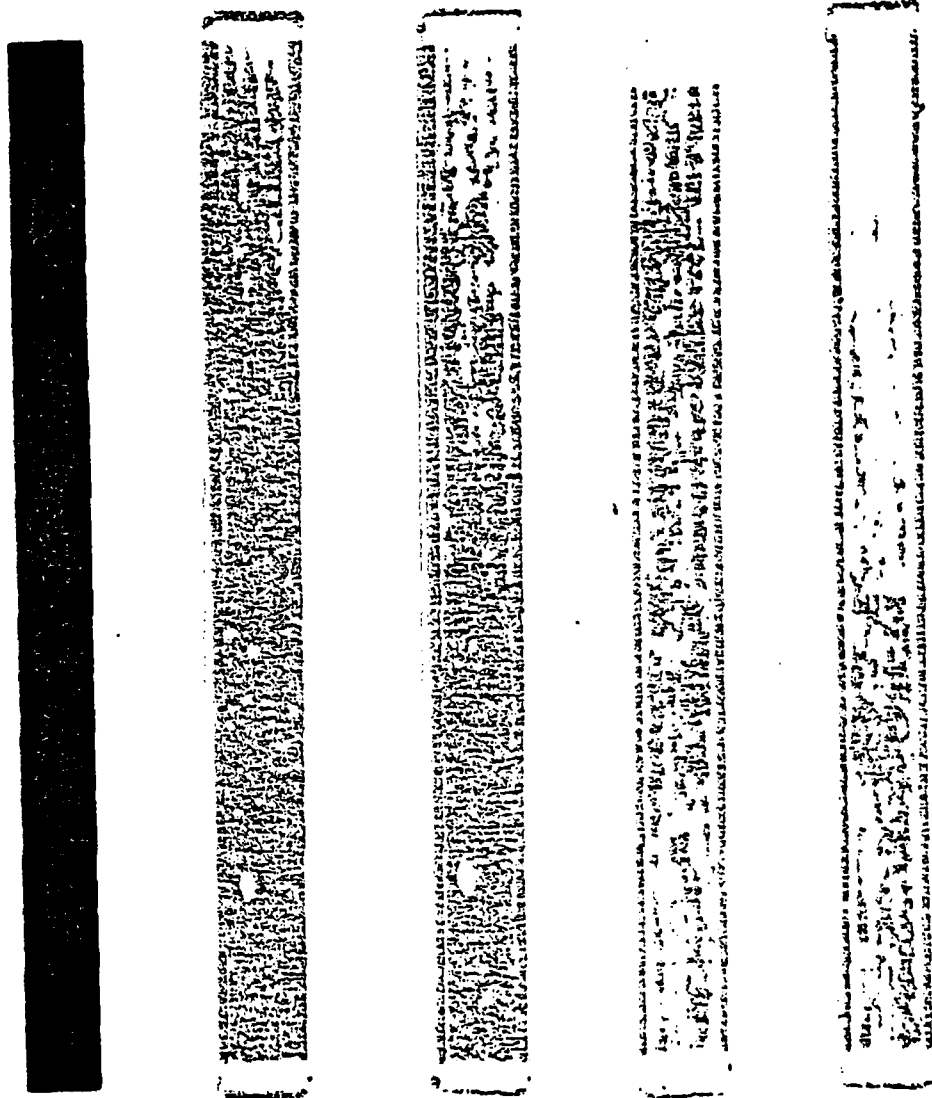


Figure 15: X-ray and C-scan of specimen 11/5.

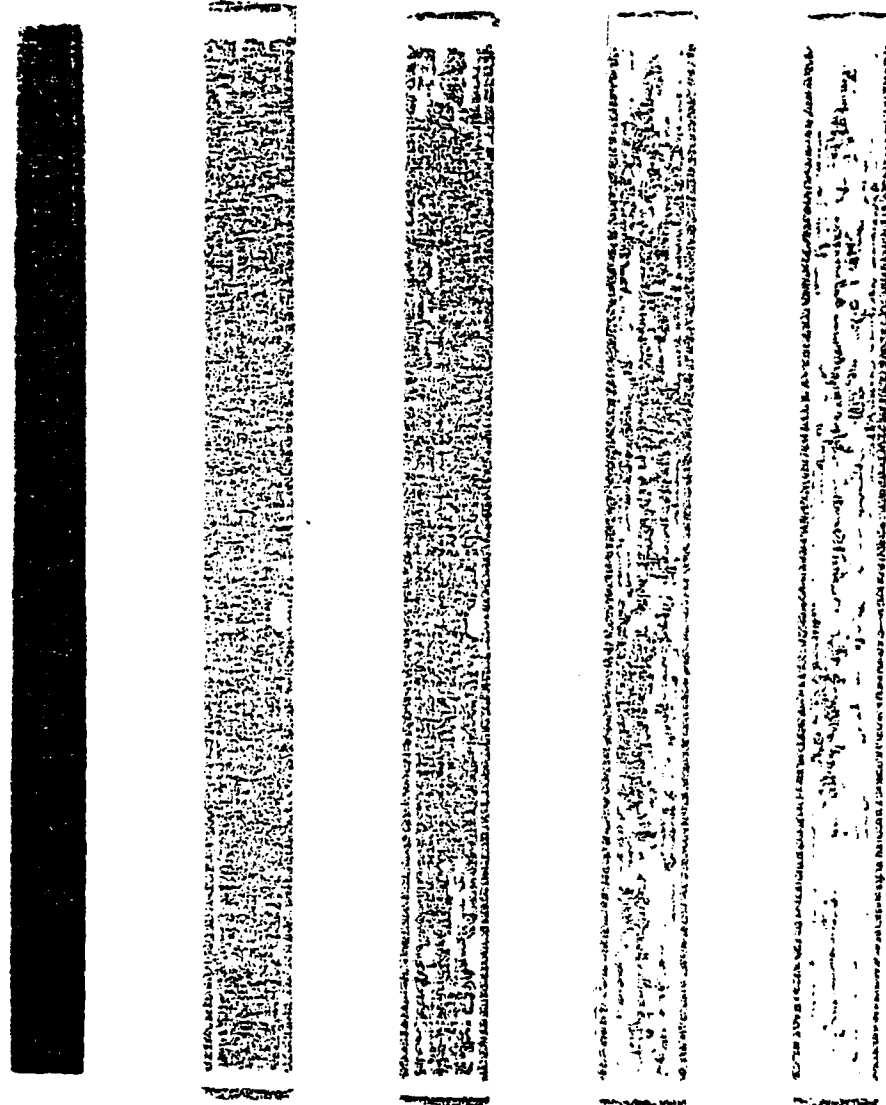


Figure 16: X-ray and G-scan of a flaw in specimen 19/5.

C-scans indicated the local damage induced by the load points. Local increases in attenuation along the tensile side were seen in several specimens. One such specimen (15/5) is shown in Figure 17. During fatigue loading the eventual failure location showed an increase in attenuation. Because a similar phenomenon did not occur in X-ray radiography, it is believed that either local matrix cracking or matrix strain hardening caused this slight increase in attenuation.

As in X-ray radiography a region near the edge could not be effectively C-scanned by the present technique. This is because the ultrasonic beam has a finite width which is distorted near the edge of the specimen. This distortion creates a dark and a light region as the transducer moves across the edge. The dark region is created by the passage of a portion of the ultrasonic wave around the specimen. As the transducer moves inward a light region caused by edge reflection usually appears. Therefore, when examining C-scans some consideration of this "edge effect" should be noted.

3.2.3 Ultrasonic Attenuation

Many problems were encountered when measuring ultrasonic attenuation by the pulse echo technique described in Section 2.3.3. The primary problem was in obtaining a consistent coupling between the transducer and the specimen. Attenuation readings were virtually impossible to repeat one day to the next. However, some consistency was established in the relative attenuation amplitudes measured during the application of load.

A plot obtained by measuring and averaging the attenuation five

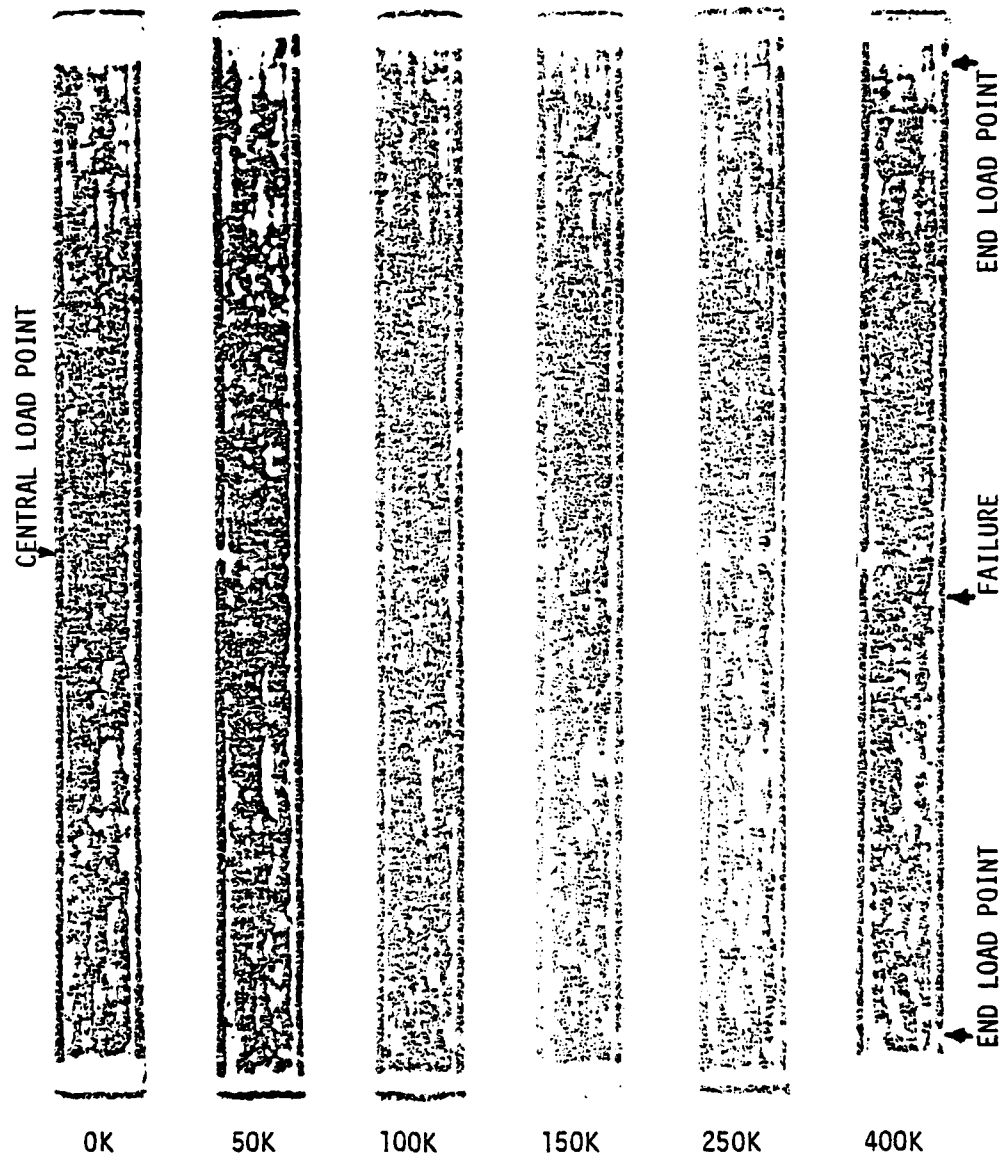


Figure 17: C-scan setting 6/8 for various fatigue cycles on specimen 15/5.

times in each of twelve locations along specimen 8/5 is given in Figure 18. On the top of Figure 18 a C-scan is shown for comparison. The regions with the highest attenuation, located between the zero inch and one inch point correspond to white or high attenuation spots on the C-scan. Also, the dark zones on the C-scan correspond to regions with lower attenuation.

The comparison of the results from ultrasonic attenuation measurements and ultrasonic C-scanning demonstrates several advantages of the C-scan technique. First, ultrasonic C-scan gives very fine resolution. This is primarily due to the smaller C-scan beam width. The 1/2 inch beam generated by the transducer used for the A-scan spreads as it travels through the quartz delay block while the 1/4 inch beam generated by the C-scan transducer is focused and hence narrows as it passes through the coupling medium, water. Therefore, with an approximate specimen width of 1/2 inch it is easy to see why C-scanning provides much better resolution. Secondly, the C-scan data is much more repeatable. There is no problem obtaining consistent coupling with the C-scan technique but for attenuation measurements, the coupling was inconsistent. An important advantage of attenuation measurement is obtaining the actual attenuation instead of having the qualitative statement that the returning pulse is less than or greater than the preset trigger level. However, by running multiple trigger level C-scan sets with the standard specimen, small changes in relative attenuation can be monitored. Therefore, since ultrasonic C-scanning was more detailed, more repeatable and easier to perform, the C-scan method was used more frequently than the A-scan. The latter was in fact applied only to a

SPECIMEN #8/5

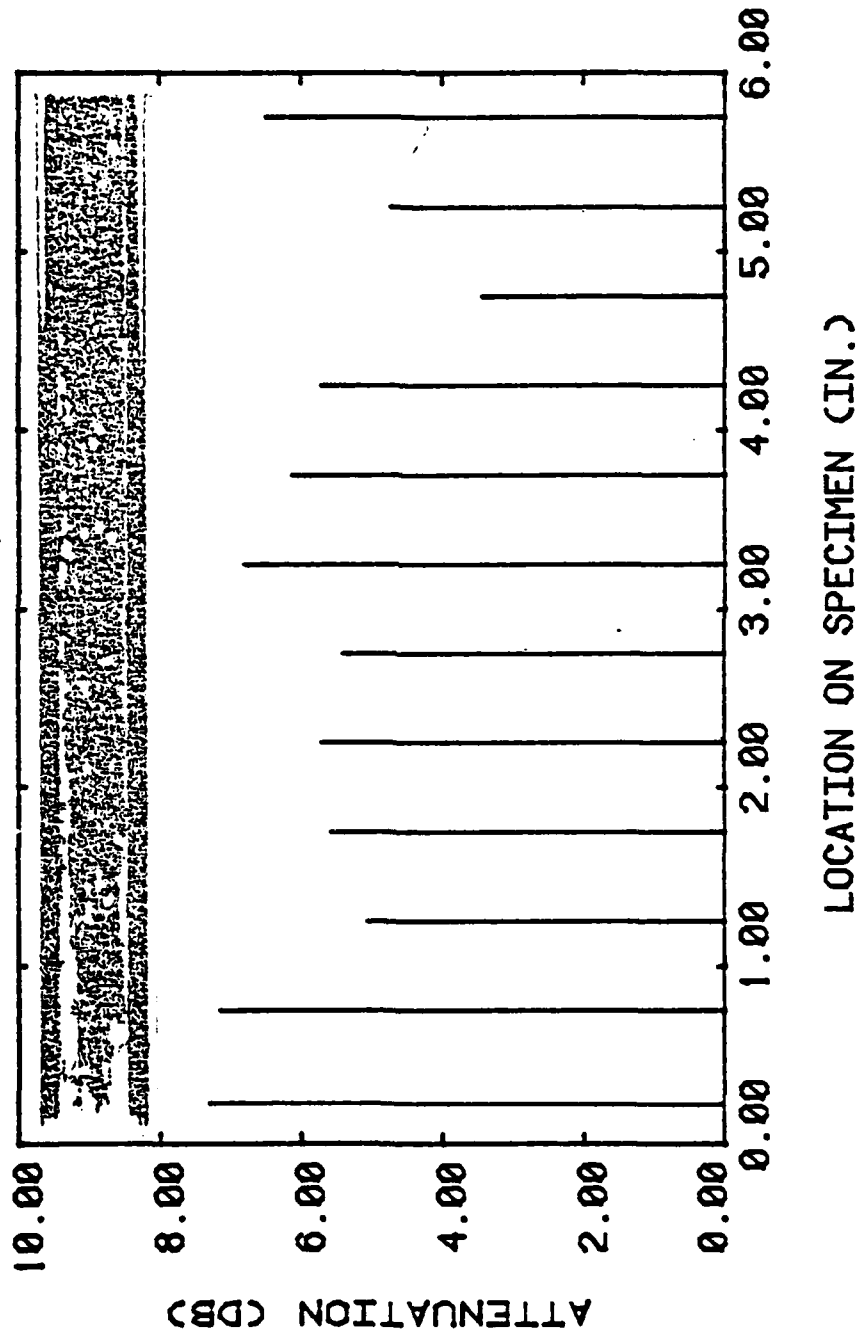


Figure 18: Comparison of Ultrasonic Attenuation and Ultrasonic C-Scan.

few initial tests.

Using the smaller 1/4 inch transducer without a delay block, similar problems were encountered. Ultrasonic attenuation measurements were so couplant sensitive in this case that comparisons were meaningless. Therefore, after trying this technique for several fatigue tests and finding the attenuation measurement on the standard specimens varying by more than 100%, this technique was abandoned.

When ultrasonic attenuation was plotted against load in axial tests various types of results occurred. For some tests, with an increase in load, the ultrasonic attenuation increased (Figure 19). For other tests, the attenuation decreased (Figure 20). A possible explanation for this is that the Poisson effect changed the location of the returning pulse thus altering the attenuation reading in a variety of ways. However, similar results have been observed in graphite epoxy laminates [15].

One additional empirical observation is worthy of note. A slight increase in wave speed was thought to occur after a few fatigue cycles. This might be due to the increase in moduli noticed during fatigue testing. However, no attempt was made to quantify or verify this observation.

3.2.4 Thermography

No significant thermal patterns were detected by real-time video-thermography when the specimen was subjected to either ultrasonic vibrations or fatigue loading. This was primarily due to the high thermal conductivity of the aluminum matrix. It was noticed that the

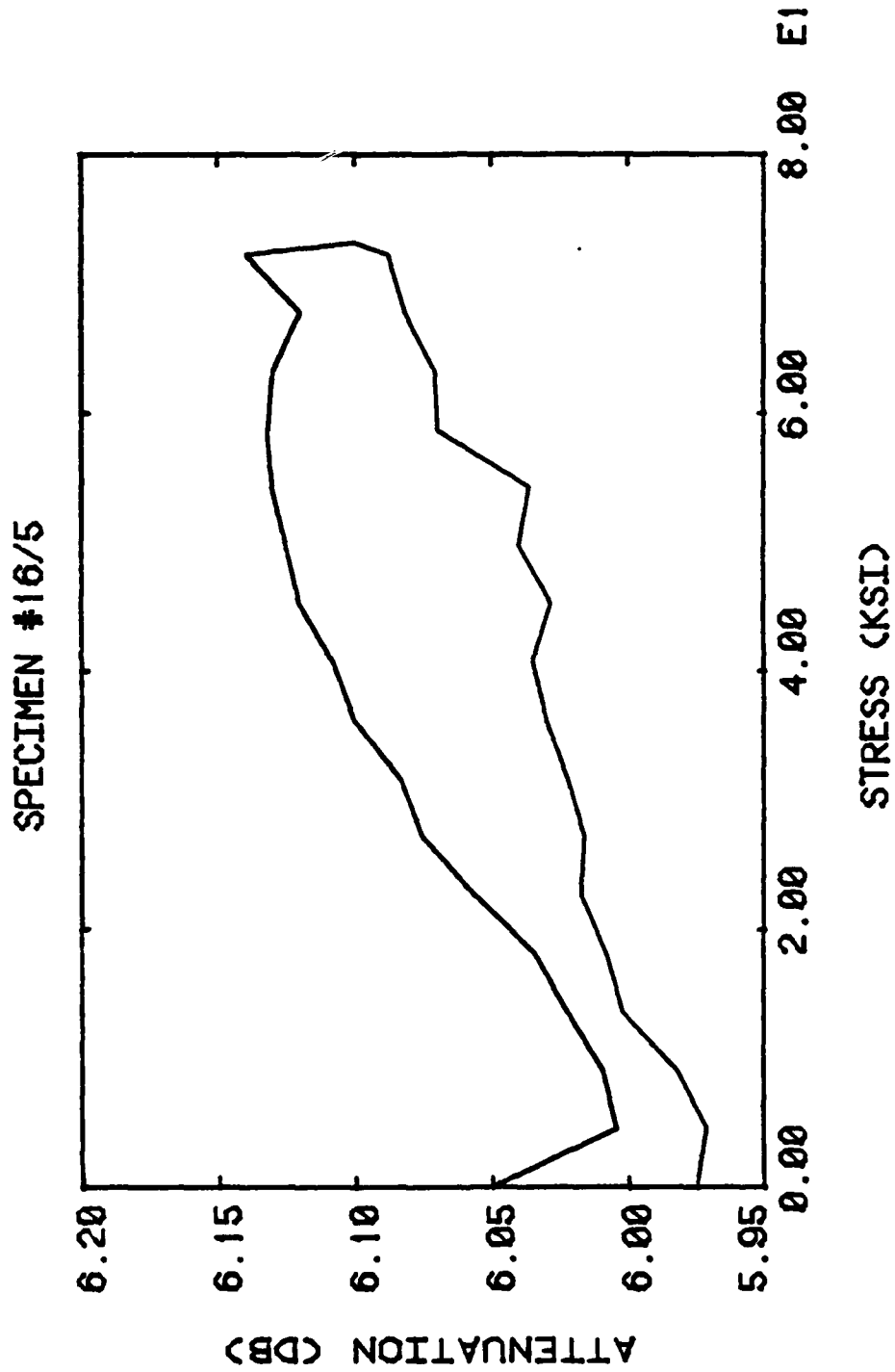


Figure 19: Ultrasonic Attenuation measured during Quasi-Static Tension Test.

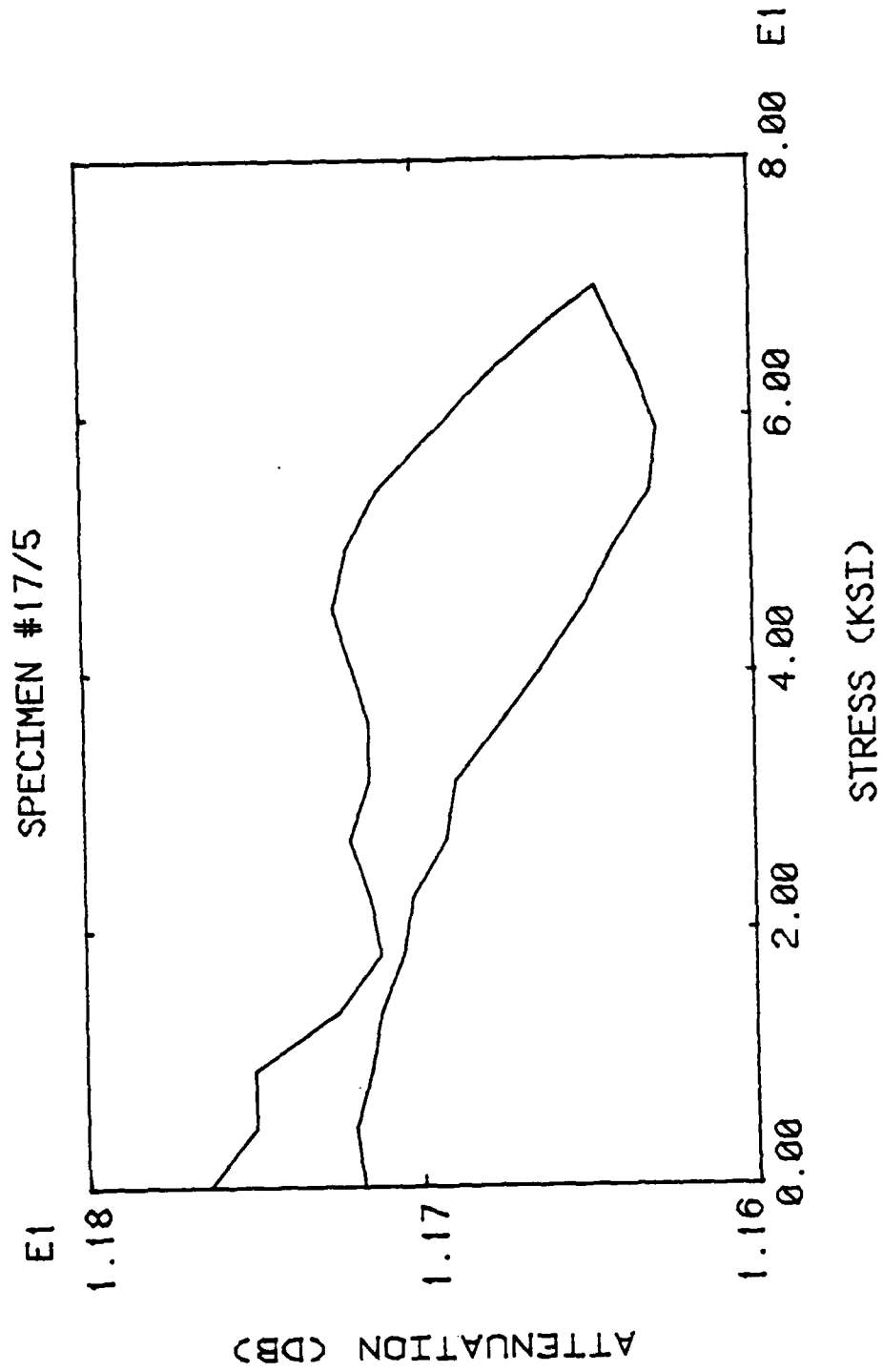


Figure 20: Ultrasonic Attenuation measured during Quasi-Static Tension Test.

compression side of the specimen was slightly hotter than the tension side. The only other thermal patterns detected appeared at the instant of failure and then dissipated very rapidly. This implies that the failure process is rapid. Therefore, in order to use thermography as an NDE technique for FP/Al, additional work will need to be done to determine if any other thermographic techniques, such as external heating, might be appropriate for this material.

3.2.5 Replication

Using the technique of replicating the edge and the side of the specimen during an axial load of 40 ksi at intermediate fatigue increments, nothing significant was found. No fatigue cracks were apparent because they were either non-existent, not exposed to the surface, or not opened by the axial loading.

3.2.6 Stiffness Change

Several interesting phenomena occurred while monitoring stiffness during intermediate stages of fatigue. After the first few fatigue cycles, the stiffness increased considerably. In FP/Al the initial stiffness increase is primarily due to the matrix work hardening. After additional fatigue cycles a gradual stiffness decrease occurred. The stiffness reduction might be accounted for by matrix cracking, matrix splitting, fiber-matrix debonding, fiber breakage or most probably, a complex combination of these.

Tables 8A and B show typical stiffness data obtained for fatigue specimens. Initial stiffness increases followed by a gradual stiffness reduction occurred for both specimens. Notice that the flexural modulus,

Table 8A: Longitudinal Stiffness, E_A , and Flexural Stiffness, E_B , for Specimen 16/5

Cycles (K)	E_A (Msi)	E_B (Msi)	E_A % Change	E_B % Change
0	32.3	30.4	---	---
10	33.2	31.5	3.1	3.6
50	34.2	32.6	5.9	7.4
100	33.4	33.0	3.4	8.6
150	33.7	33.5	4.3	10.2
250	34.3	33.8	6.2	11.2
400	33.0	32.8	2.2	7.9
600	32.7	33.2	1.2	9.2
800	32.9	32.6	1.9	7.2
1000	32.5	32.8	0.6	7.9

Table 8B: Longitudinal Stiffness, E_A , and Flexural Stiffness, E_B , for Specimen 12/4

Cycles (K)	E_A (Msi)	E_B (Msi)	E_A % Change	E_B % Change
0	30.9	28.6	---	---
10	31.8	30.6	2.8	4.8
50	31.7	30.4	2.4	5.8
100	32.5	31.0	5.1	8.2
150	32.3	29.7	4.6	3.6
250	31.4	30.0	1.6	4.5
400	31.8	29.4	2.7	2.4

E_B , is in general slightly less than the longitudinal modulus, E_A . This is because the deformation due to shearing stresses is neglected. The few places where E_B is greater than E_A occur after several fatigue increments. Therefore, local work hardening concentrated away from the neutral axis increased the value recorded for E_B more than for E_A . Also, inside the gauge length a slight deformation due to the central load point reduces the cross-sectional area which might have affected the axial stiffness. The values of percent stiffness given in Tables 8A and B are also plotted in Figures 21 and 22.

Figure 21 shows the large stiffness increase found in specimen 16/5. In the axial plot the sharp decrease at 100K and 150K cycles is believed to be due to improper extensometer calibration. The extensometer was found to have been out of calibration and was recalibrated after 250K cycles. Tests of the accuracy of the stiffness measurements indicated that the error could be held consistently to within one percent for both axial and bending cases.

Specimens 11/5 and 15/4 were tested monitoring only flexural rigidity. The results obtained are given in Table 9. The percent stiffness changes are plotted in Figures 23 and 24. Again, after 10K cycles both specimens showed large stiffness increases. However, the stiffness of specimen 11/5 (Figure 23) appeared to be stabilized before additional work hardening occurred. Just before failure at 810K cycles, a small additional stiffness change was measured. This stiffness reduction could indicate damage initiation or propagation. In specimen 15/4 (Figure 24) no significant stiffness change occurred after 150K cycles. When a residual strength test was performed after 1500K cycles,

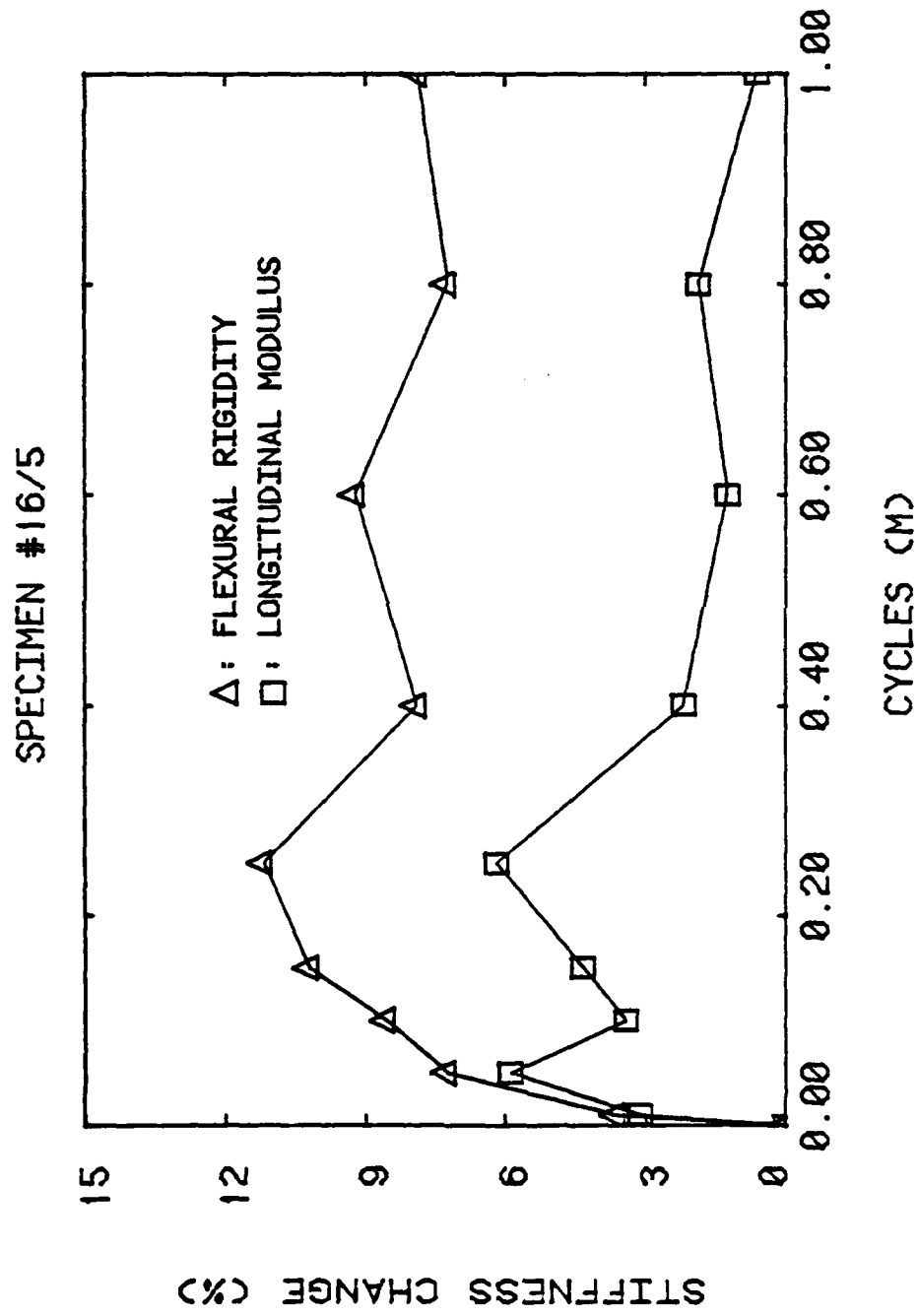


Figure 21: Stiffness Change versus Cycles of Loading in Bend Test

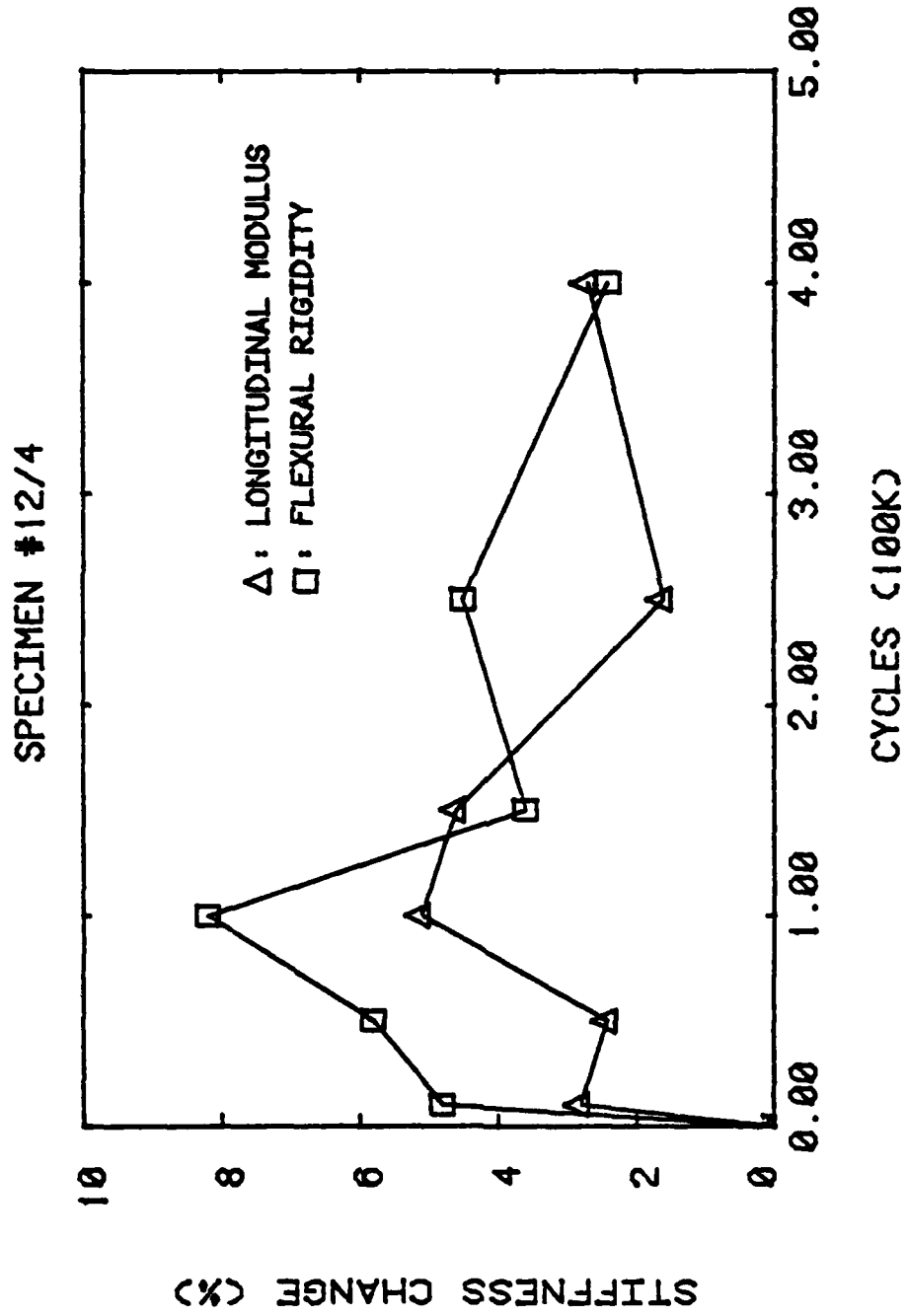


Figure 22: Stiffness Change versus Cycles of Loading in Bend Test.

Table 9: Flexural Stiffness for Specimens 15/4 and 11/5

Cycles K	Specimen 11/5		Specimen 15/4	
	E_B (Msi)	E_B % Change	E_B (Msi)	E_B % Change
0	31.8	---	28.8	---
10	32.5	2.2	30.1	4.5
50	32.2	1.3	30.0	4.2
100	32.3	1.6	30.0	4.2
150	32.2	1.3	30.4	5.6
250	32.6	2.5	30.3	5.2
400	33.1	4.1	30.3	5.2
600	33.5	5.3	30.7	6.6
800	33.1	4.1	30.7	6.6
1000	---	---	30.5	5.9
1500	---	---	30.6	6.3

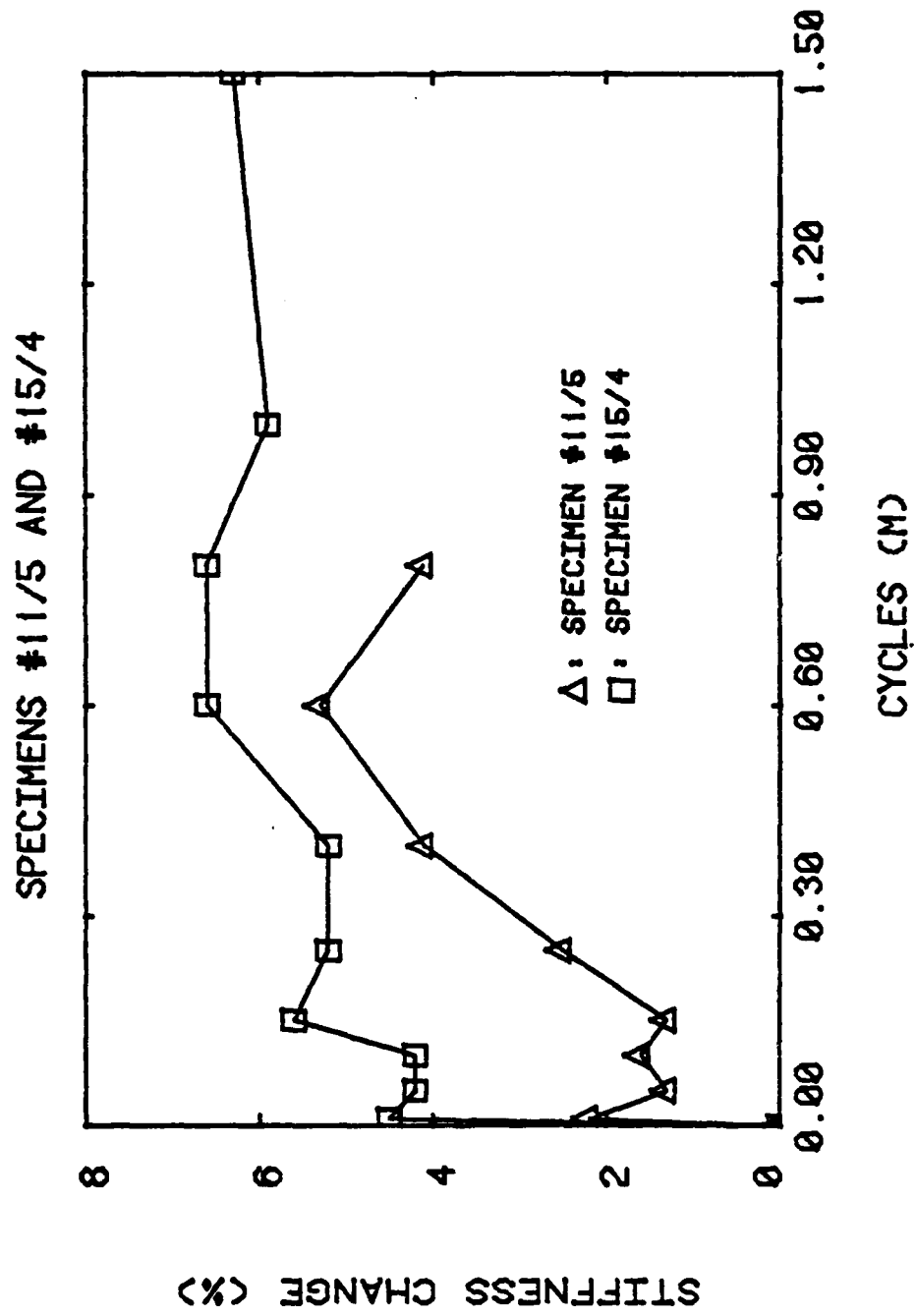


Figure 23: Stiffness Change versus Cycles of Loading in Bend Test

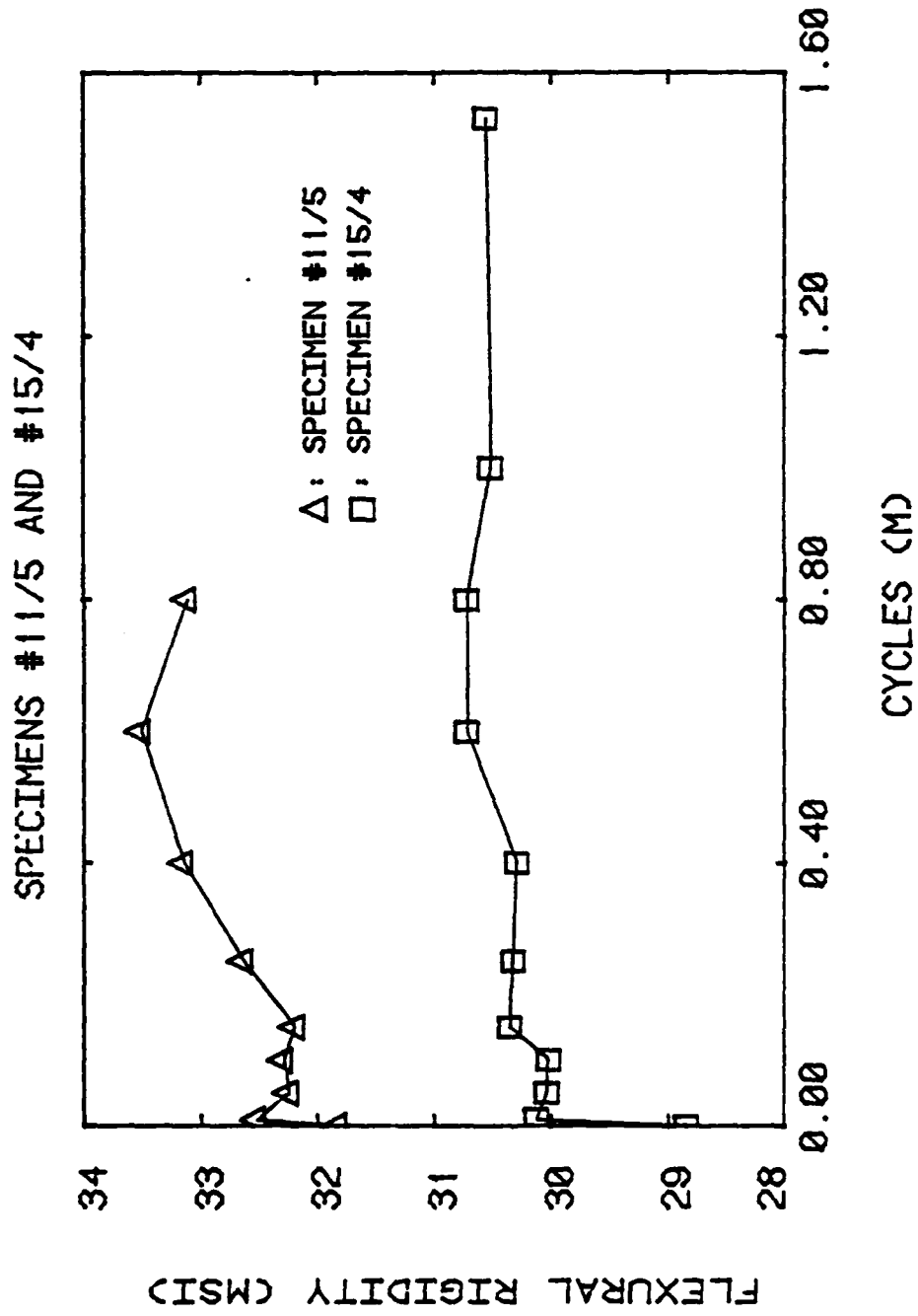


Figure 24: Flexural Rigidity versus Cycles of Loading in Bend Test

the quasi-static failure load was 376 pounds. This was the maximum failure load for any quasi-static failure. Since no stiffness reduction occurred and no apparent reduction in initial strength can be inferred, the damage that occurred due to fatigue was not significant.

3.2.7 Eddy Current

Results of the eddy current testing showed that the system used was not sensitive enough to find any significant variations in reactance and resistance. Tables 10 and 11 give the reactance and resistance across the surface of two specimens. Notice there is very little variance in the values recorded. On the 45% V_f specimen (Table 10), reactance ranged from 516 to 521 while resistance ranged from 621 to 630. Similarly for the 55% V_f specimen (Table 11), reactance varied from 516 to 524 and resistance varied from 620 to 624.

When analyzing results from intermediate fatigue stages over a period of several days, large differences occurred in the reactance and resistance of air. Therefore, to compensate for these environmental differences, all data were corrected by subtracting the reactance and resistance of a standard aluminum block. By doing this, environmental effects such as temperature and humidity, could be partially eliminated. The results obtained by correcting eddy current data for specimen 15/5 are shown in Figures 25, 26 and 27. All three locations are plotted with measurements taken from the "red" (front) and "black" (back) sides appearing on the same graph. Note the pattern that develops. Regardless of location or side, all three reactance plots and all three resistance plots behave similarly, respectively. This indicates that

Table 10: Reactance (X) and Resistance (R)
Measured Across the Surface of a
45% V_F FP/Al Specimen by Eddy
Current Technique

X—	519	521	521	518	518
R—	627	623	622	627	623
	519	521	520	518	516
	625	621	622	626	623
	519	517	518	517	517
	626	623	623	627	625
	518	518	517	517	517
	626	625	626	626	626
	519	517	517	517	517
	626	625	627	627	627
	519	519	518	517	517
	626	625	628	627	627
	519	519	518	517	517
	625	626	627	627	628
	518	518	518	518	518
	626	625	627	626	627
	520	519	518	517	517
	626	626	626	627	627
	519	519	518	517	517
	627	626	625	627	627
	520	519	519	518	517
	626	626	626	627	626
	519	519	518	518	518
	627	627	626	626	626
	519	519	518	518	518
	627	625	627	627	627
	519	519	518	519	518
	627	625	626	627	627
	520	518	519	517	518
	626	626	626	627	627
	520	517	519	519	518
	627	628	626	627	627
	519	518	518	518	518
	627	630	626	627	628

1/16 in

1/4 in

Table 11: Reactance (X) and Resistance (R)
Measured Across the Surface of a
55% V_p FP/Al Specimen by Eddy
Current Technique

X-	518	518	518	520
R-	622	624	621	623
	518	517	518	519
	622	623	621	623
	518	516	518	519
	622	623	623	623
	518	518	518	520
	623	624	622	624
	518	518	518	520
	623	624	622	624
	518	518	518	520
	623	623	622	624
	518	518	519	520
	624	623	622	624
	519	519	519	520
	624	624	621	624
	518	519	520	521
	624	622	621	622
	519	518	520	521
	623	623	622	623
	519	520	520	522
	623	623	621	622
	520	520	521	522
	623	623	621	623
	520	521	522	522
	623	623	620	623
	521	521	522	523
	622	622	621	623
	521	522	524	524
	623	622	622	623
	522	522	522	523
	623	620	620	622
	522	522	524	524
	622	621	621	622

← $\frac{1}{16}$ in →

↓ $\frac{1}{4}$ in ↑

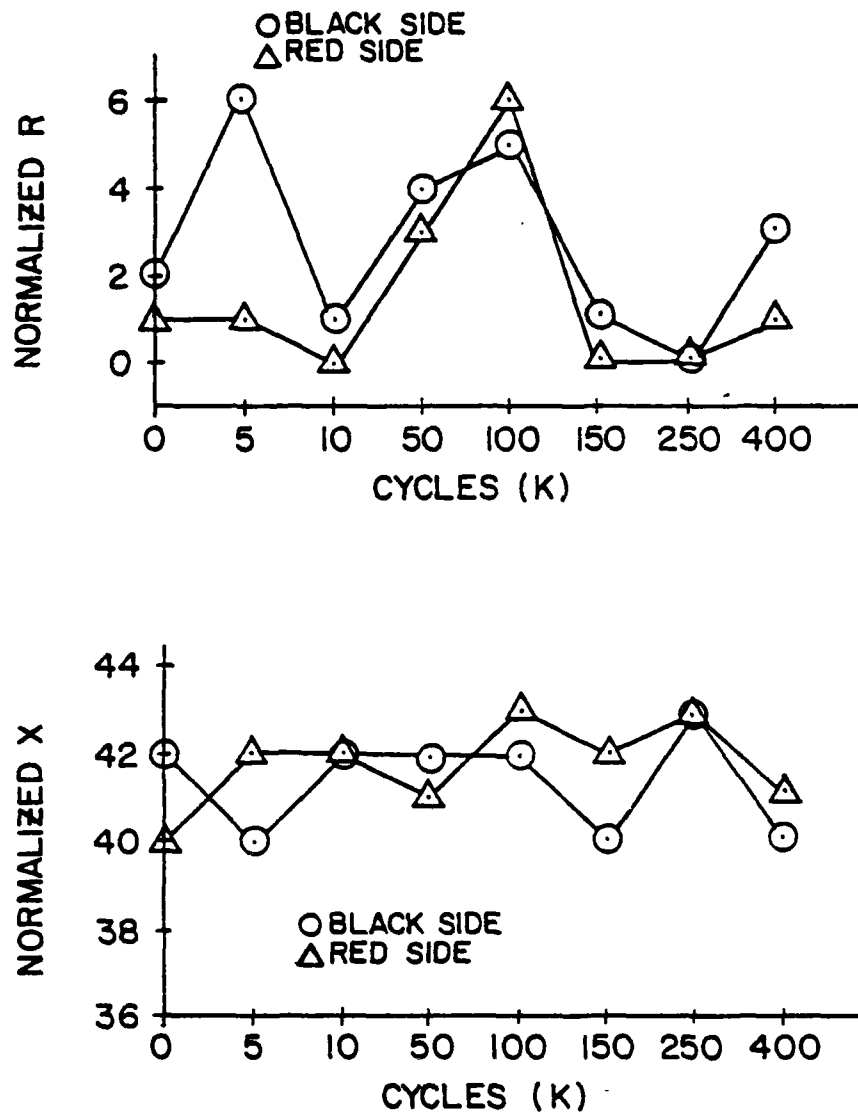


Figure 25: Normalized Values of Resistance (R) and Reactance (X) measured by Eddy Current versus Cycles of Bending Fatigue, Location (1).

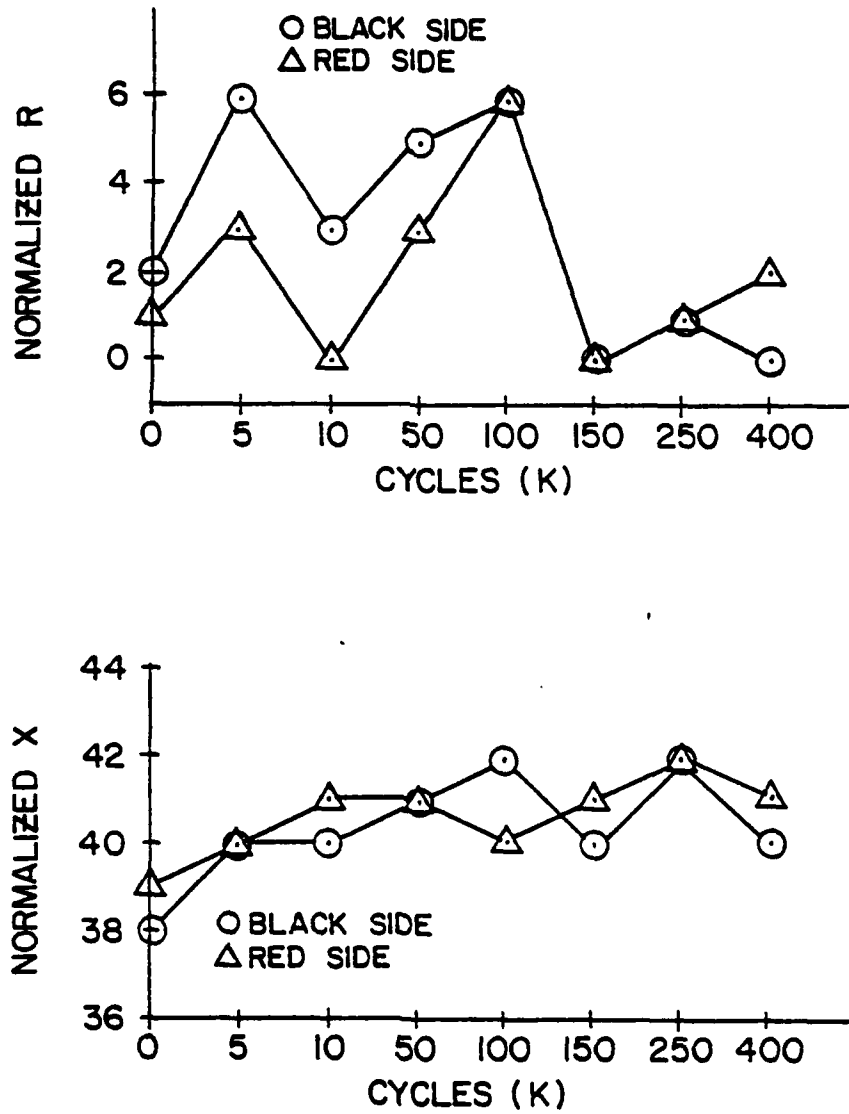


Figure 26: Normalized Values of Resistance (R) and Reactance (X) measured by Eddy Current versus cycles of Bending Fatigue, Location (2).

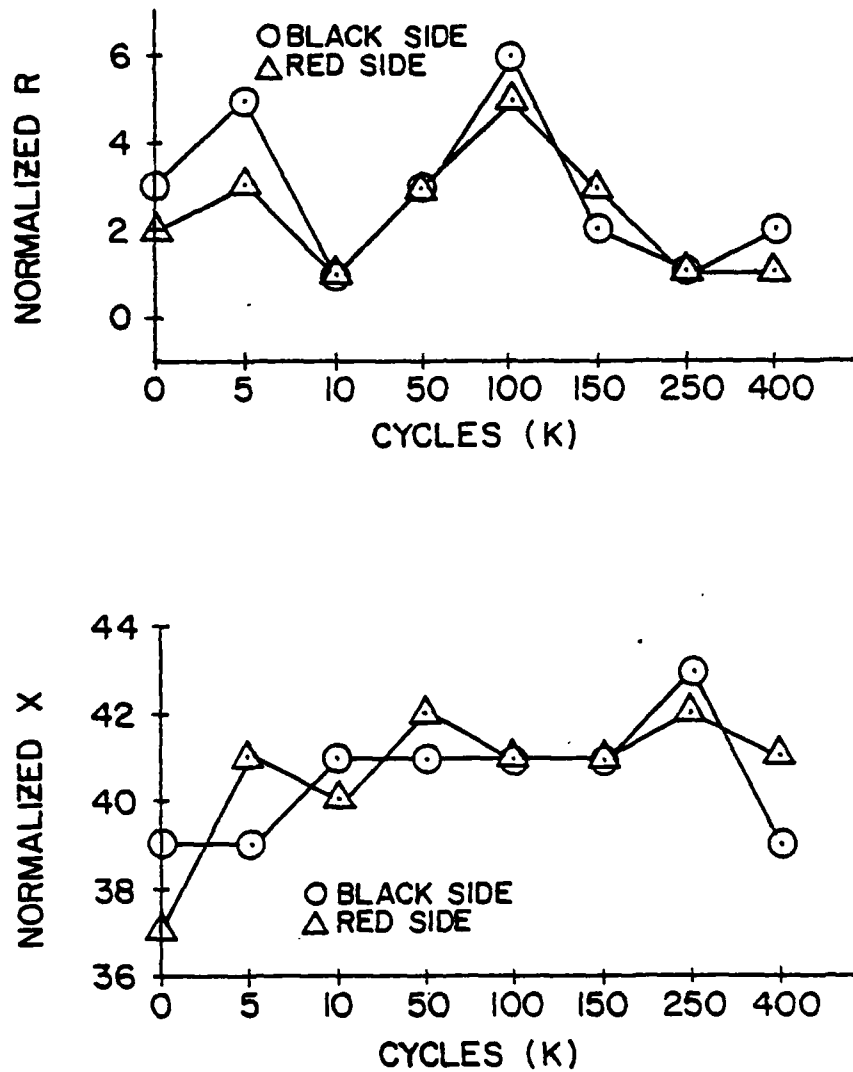


Figure 27: Normalized Values of Resistance (R) and Reactance (X) measured by Eddy Current versus Cycles of Bending Fatigue, Location (3).

what little variance existed was primarily due to environmental effects.

Further testing indicated that the eddy current system used was not sensitive enough to locate flaws such as discussed in Sections 3.2.1 and 3.2.2. This may be due to the fact that the testing frequency used (100 kHz) to drive the probe is not optimum for FP/A1. Also, limitations due to edge effects as discussed in chapter two make the detection of an edge crack suspect.

3.2.8 Acoustic Emission

Several interesting phenomena occurred while monitoring acoustic emission in FP/A1. Acoustic emission was concentrated in two regions of the loading curve, at the point where the matrix material yields and near the maximum applied load. When ultrasonic attenuation measurements were made while monitoring acoustic emission in a few initial tests, interference was encountered between the two testing systems. Therefore, AE and attenuation were monitored during different quasi-static tests.

Figures 28, 29 and 30 show typical acoustic emission behavior obtained during initial quasi-static axial tests for loads to 70 ksi. Notice that in general the emissions are concentrated in two load regions, one centered about 0.05% strain and the other centered about 0.25% strain. However, in Figure 28 (specimen 7/4) the initial AE concentration that appears in Figures 29 and 30 does not exist, even though the acoustic emission did initiate in this region. As the strain exceeded 0.15% the number of counts increased with strain until the maximum desired stress, 70 ksi, was obtained. For specimen 16/5 (Figure

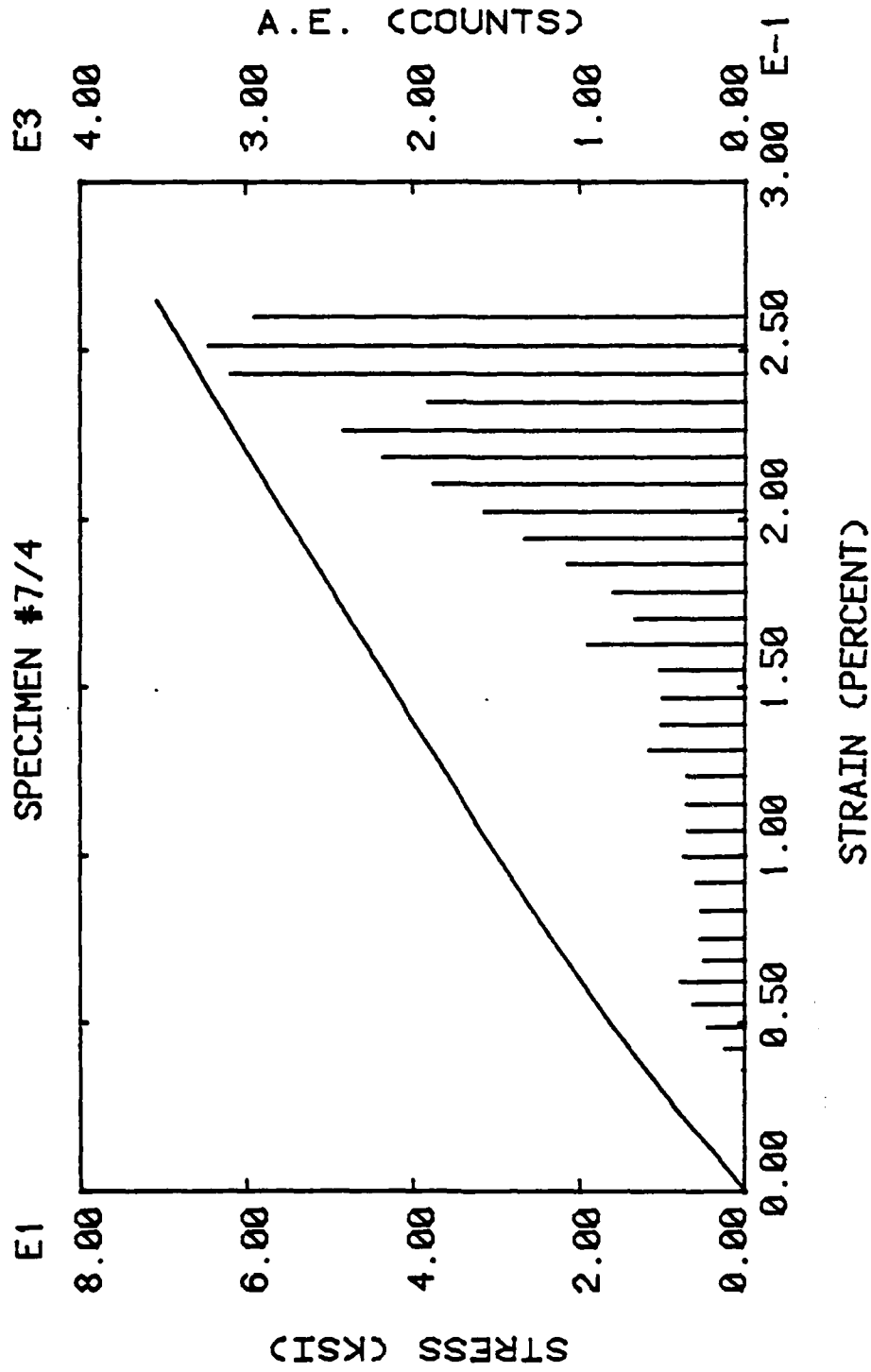


Figure 28: Stress and Acoustic Emission versus Strain for Axial Load.

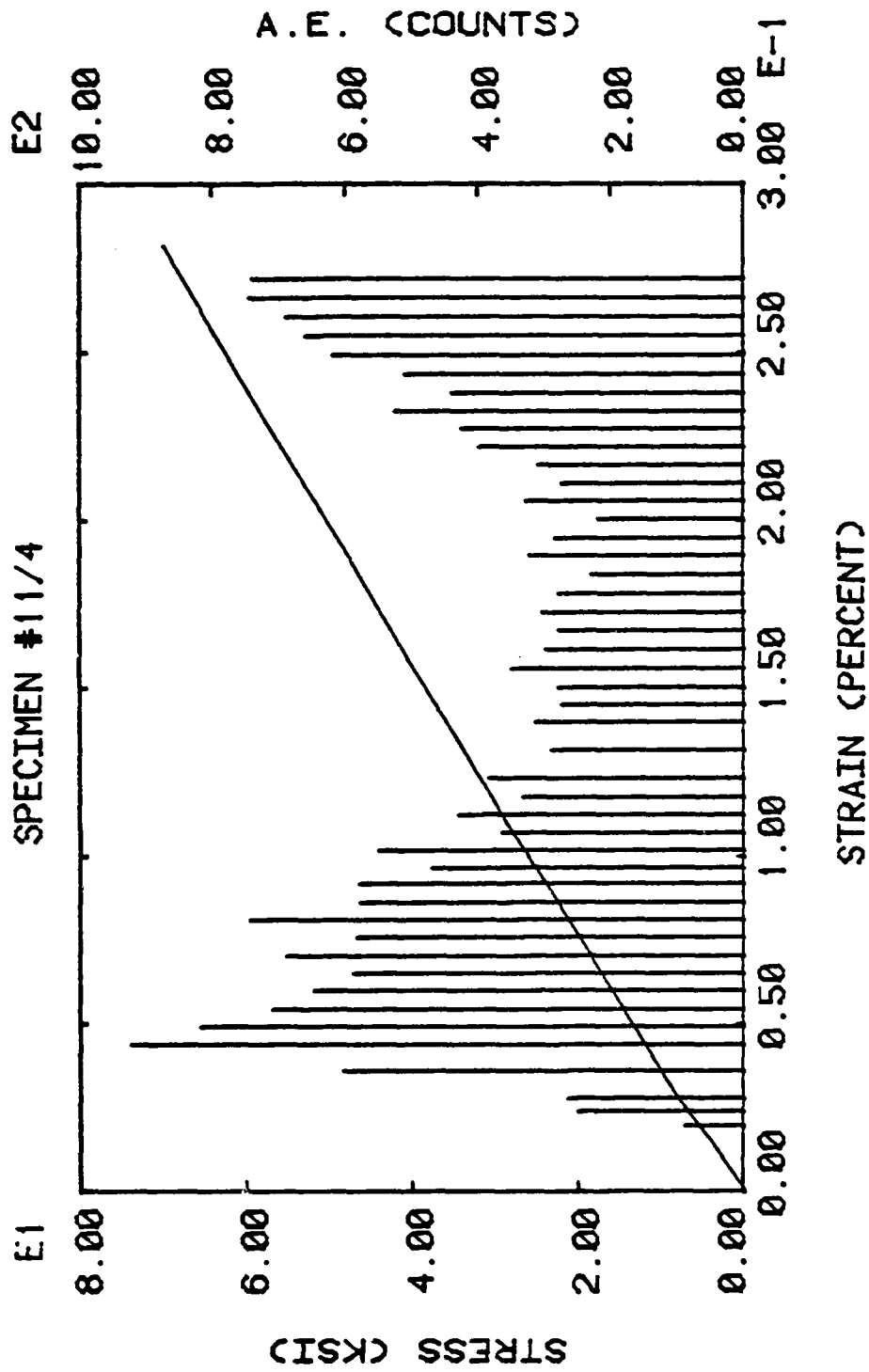


Figure 29: Stress and Acoustic Emission versus Strain for Axial Load.

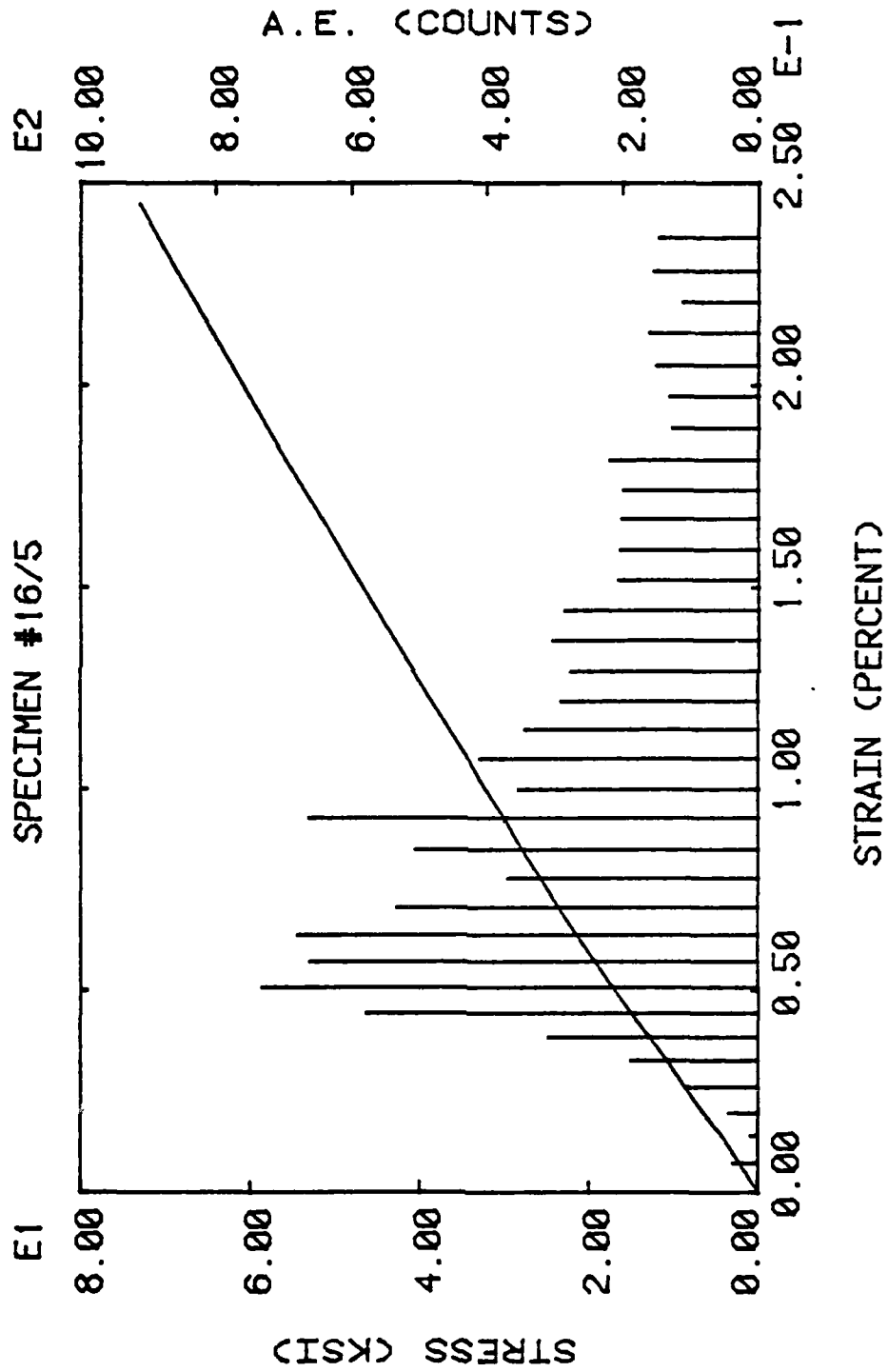


Figure 30: Stress and Acoustic Emission versus Strain for Axial Load.

30) this later increase in AE did not occur. However, it is important to note, that for other 55% V_f specimens this type of behavior was observed. There was no discernable reason for the lack of AE concentration in one or the other regions for a particular specimen, but this behavior was consistent with the bend test results discussed next.

Figures 31, 32 and 33 present typical acoustic emission data obtained during the initial quasi-static bend tests, the load-deflection curves obtained are also shown. The maximum load applied to each specimen corresponded to the maximum fatigue load later applied to each specimen. Figure 31 (specimen 3/4) displays AE peaks at the beginning and end of the load application, while Figure 32 (specimen 7/4) has only a final peak and Figure 32 (specimen 16/5) has only an initial peak. The same specimens 7/4 and 16/5 behaved similarly for both loading methods (compare Figure 28 with Figure 32 and Figure 30 with Figure 33, respectively). Note that the loads that correspond to an outer fiber stress of 20 ksi, are 61 pounds and 52 pounds for 45% and 55% V_f specimens, respectively. Therefore, the first AE concentration occurs just before the first matrix material apparently undergoes plastic deformation.

When comparing axial to bending AE, note that, in bending, after the outer fibers yield, the plastic zone moves inward toward the neutral axis. This explains the relatively constant emissions that occur. The AE increase that occurred in most tests at high loads is believed to have been caused by material damage. Specimen 16/5, for which low level AE occurred at the higher loads, did not fail until after enduring over one million fatigue cycles. This suggests that a "strong"

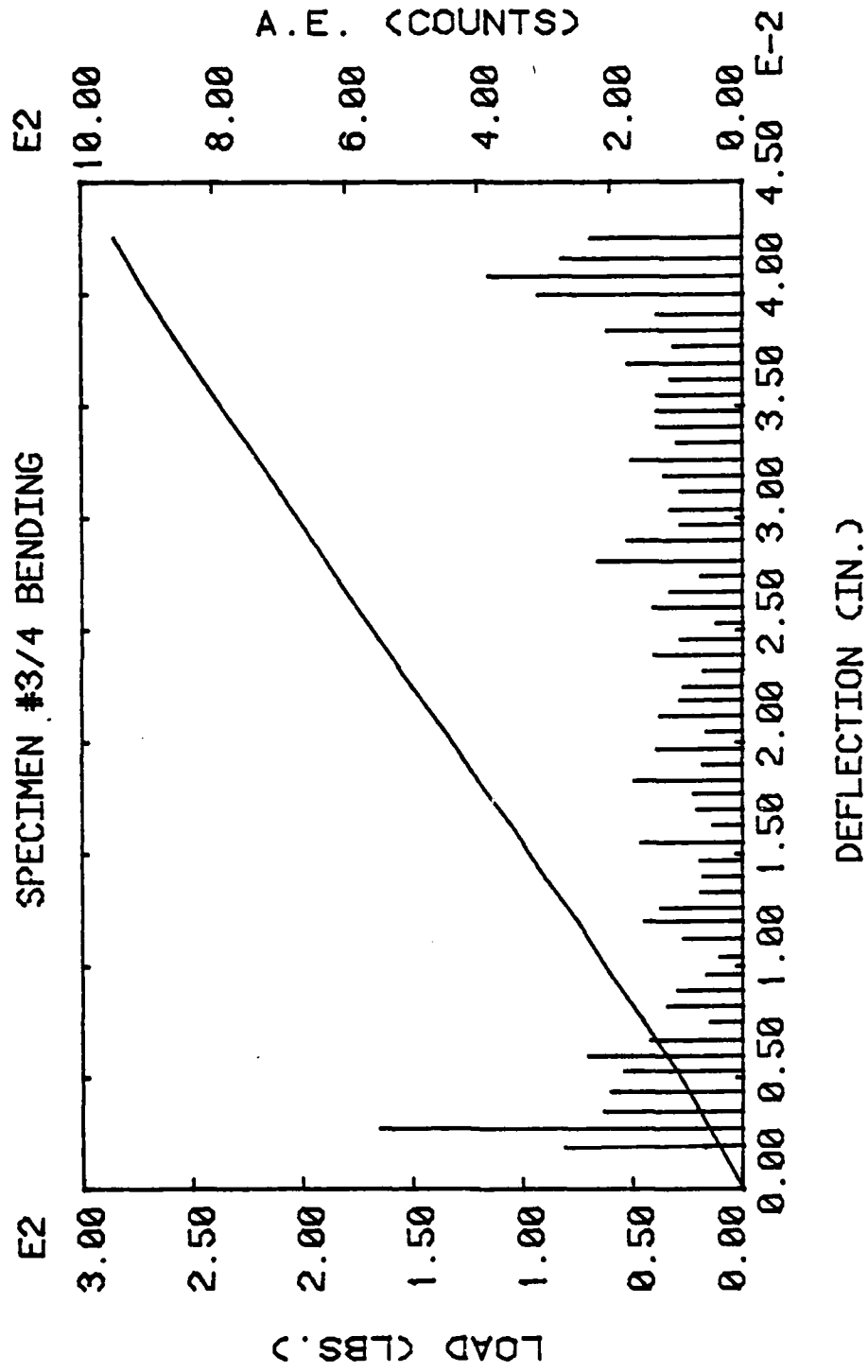


Figure 31: Load and Acoustic Emission versus Transverse Deflection for Flexural Load.

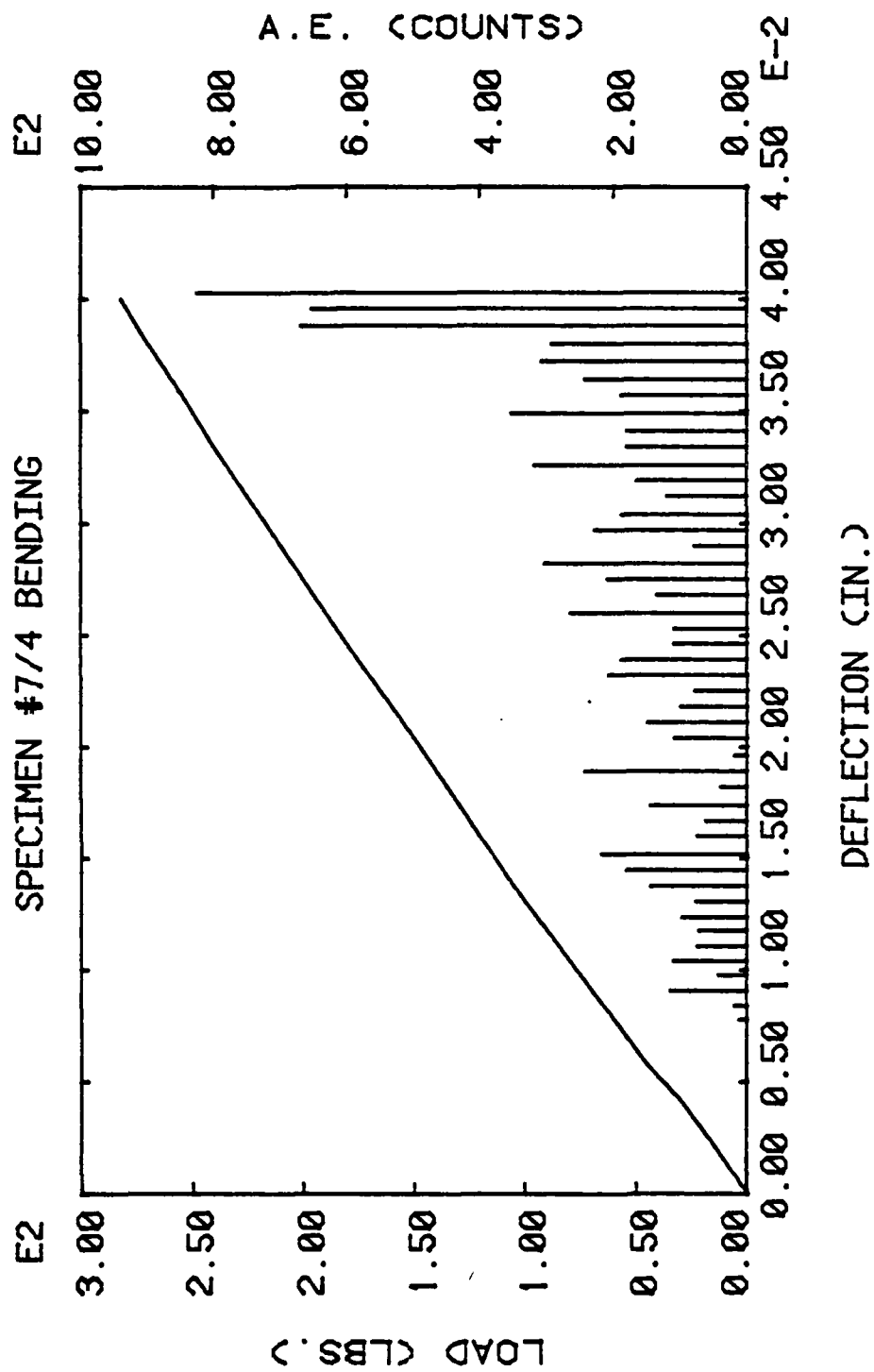


Figure 32: Load and Acoustic Emission versus Transverse Deflection for Flexural Load.

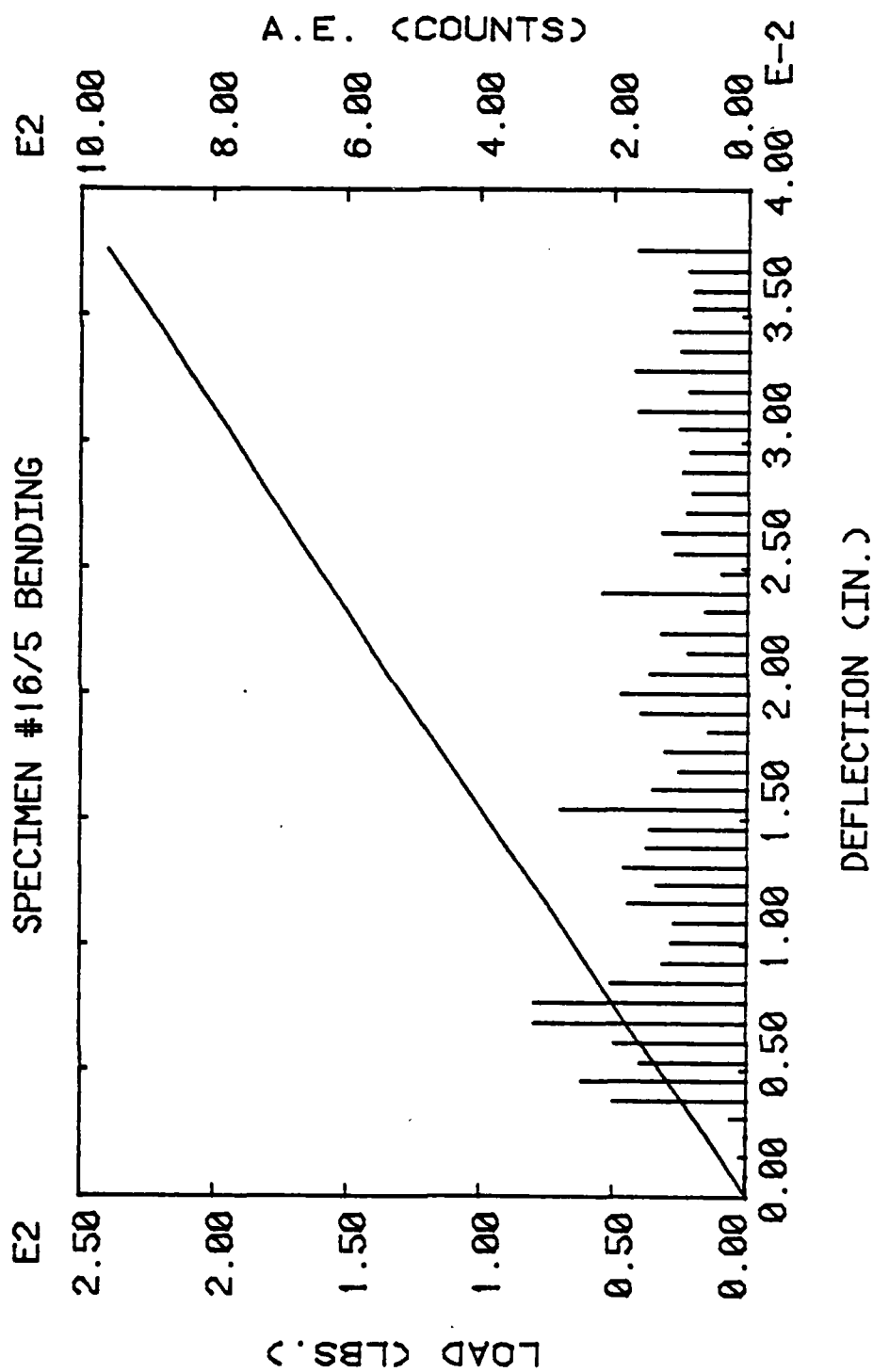


Figure 33: Load and Acoustic Emission versus Transverse Deflection for Flexural Load.

specimen may generate fewer acoustic emissions during initial testing.

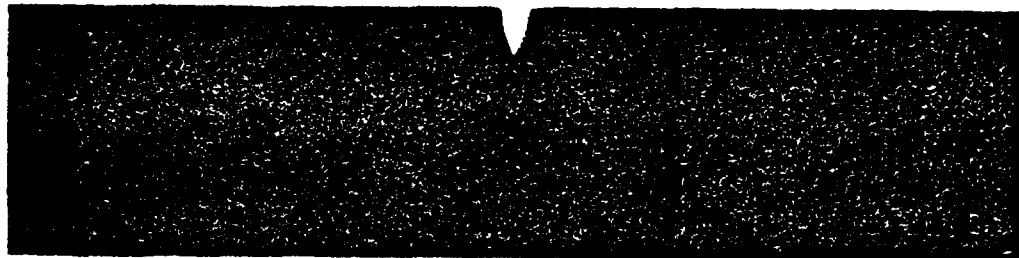
It should be noted that in several tests no useful AE data were obtained because of excessive background noise, transducer slippage or insufficient amplification.

3.3 Notched Specimens

Specimens 20/4 and 20/5 were quasi-statically loaded in the bend fixture until failure. Specimen 20/4 fractured at 113 pounds and specimen 20/5 fractured at 126 pounds. As expected, both failures occurred transversely, starting from the notch tip.

Following the two quasi-static failure tests, specimens 21/4 and 21/5 were fatigue tested to determine if crack growth could be detected using X-ray radiography. After specimen 21/4 underwent 10K cycles at 7⁵ 80, 85 and 90 pounds, a small longitudinal crack was detected growing in both directions from the notch tip. As the load and number of fatigue cycles were gradually increased, the longitudinal crack grew. Fatigue testing continued until transverse failure occurred 0.265 inches to the right of the notch tip (Figure 34E). The failure was initiated at the longitudinal split and propagated across the width of the specimen. Similar behavior was noted for specimen 21/5.

Figure 34A, B, C, D, E, F and G shows a history of the crack growth in specimen 21/4 using X-ray radiography. It should be noticed that the crack starts at the 90 pound fatigue stage and propagates gradually during each 10K fatigue increment. After 10K cycles at the 130 pound fatigue testing level, the penetrant apparently did not enter the entire crack making the crack appear shorter than it actually was (Figure 34D). Upon careful examination of the radiograph, the crack is visible beyond



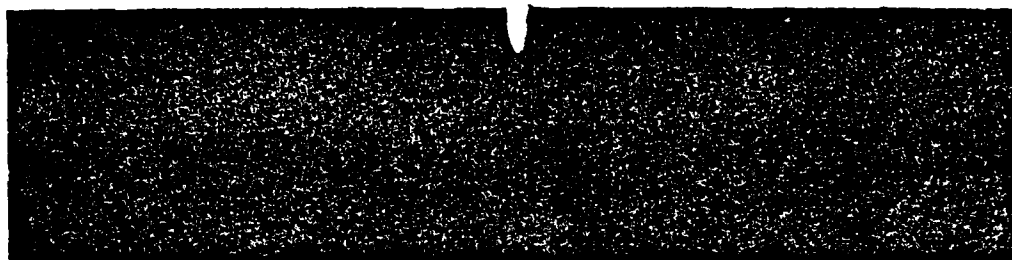
No Load



80 lbs.

Figure 34A: X-Ray Radiograph History of Specimen 21/4 showing Crack Growth.

80



90 lbs.

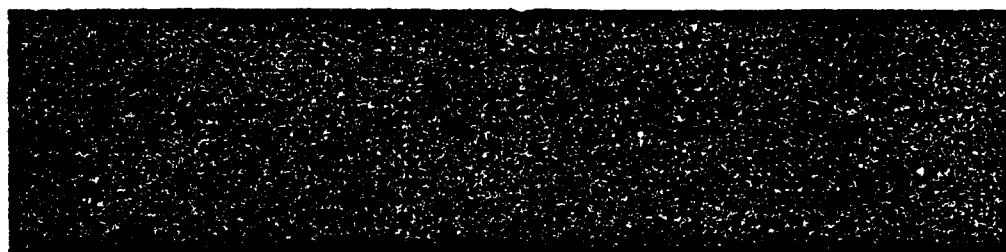


100 lbs.

Figure 348: X-Ray Radiograph History of Specimen 21/4 showing Crack Growth.

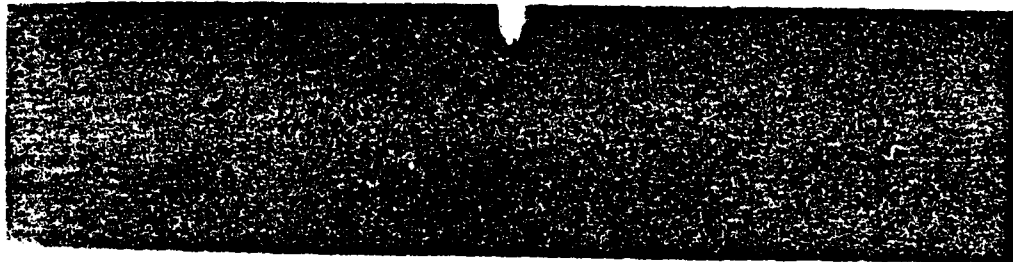


110 lbs.

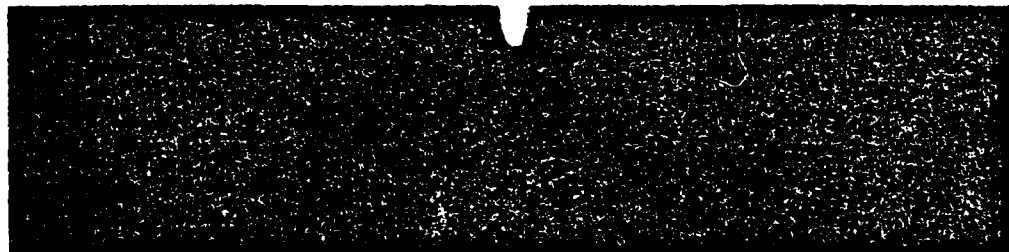


120 lbs.

Figure 34C: X-Ray Radiograph Histroy of Specimen 21/4 showing Crack Growth.

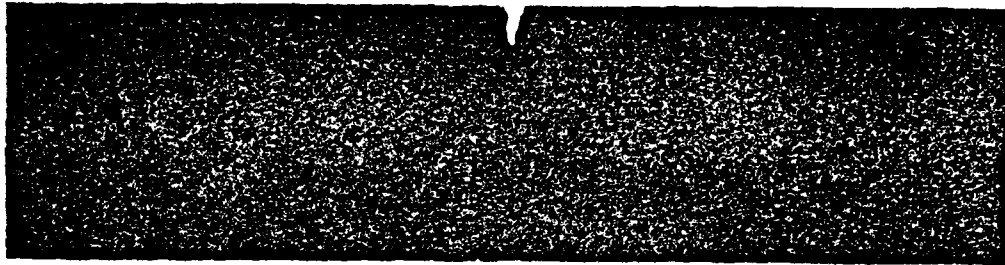


130 lbs.

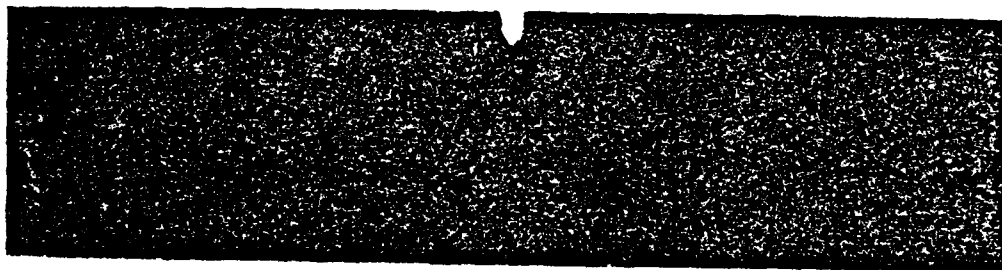


140 lbs.

Figure 34D: X-Ray Radiograph History of Specimen 21/4 showing Crack Growth.



150 lbs.



160 lbs.

Figure 34E: X-Ray Radiograph History of Specimen 21,4 showing Crack Growth.

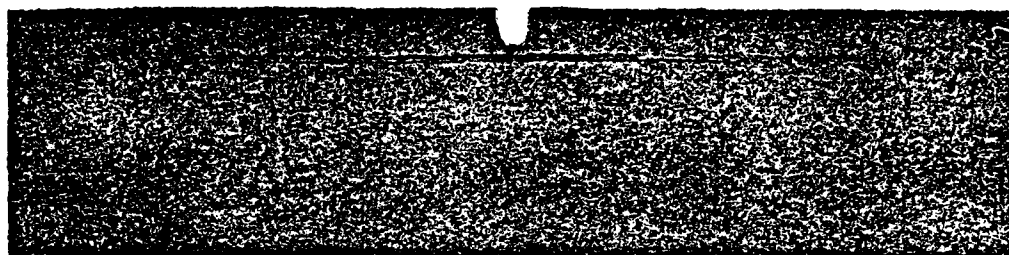


170 lbs.



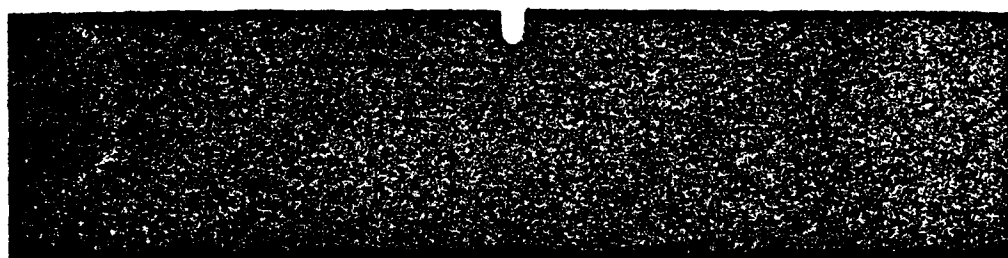
180 lbs.

Figure 34 F: X-Ray Radiograph Histroy of Specimen 21/4 showing Crack Growth.



190 lbs.

↓ FINAL FAILURE



200 lbs.

Figure 34G: X-Ray Radiograph History of Specimen 21/4 showing Crack Growth

the region darkened by the presence of the penetrant. The location of final failure is shown in Figure 35G on the last radiograph taken before failure.

Further NDE indicated that the longitudinal crack could be detected by ultrasonic C-scan, eddy current, ultrasonic pulse-echo and replication. Eddy current tests performed on specimen 16/4 showed that the reactance, X , increased from 518 to 538 and the resistance, R , decreased from 630 to 598 as the transducer was moved over the crack. Both of these values are approaching the readings for air, $X = 559$, and $R = 534$, which implies the presence of a crack. Ultrasonic pulse-echo indicated the presence of the crack when the 1/4 inch 10 MHz transducer was adequately coupled to the 1/10 inch edge of the specimen. The crack was detected using the pulse-echo technique and observing the time for the echo to return.

Video-thermography provided some interesting data during the notch fatigue tests. Figure 35A, B, C and D shows thermographs taken during the 210 pound fatigue test performed on specimen 21/4. In order to permanently record thermal changes, a video tape recorder was used to record the image from the thermographic monitor. Later, the tape could be replayed a frame at a time and photographed. This enabled the capture of changes within the framing rate of the thermographic camera (1/16 sec) and within a single fatigue cycle. Figures 35A and B show thermographs taken within the same fatigue cycle, about 1/2 second before failure. Figure 35A was taken near maximum fatigue load which generated heat (indicated by the red color band) on the compression side. Also a colder region (blue) can be noticed along the crack.

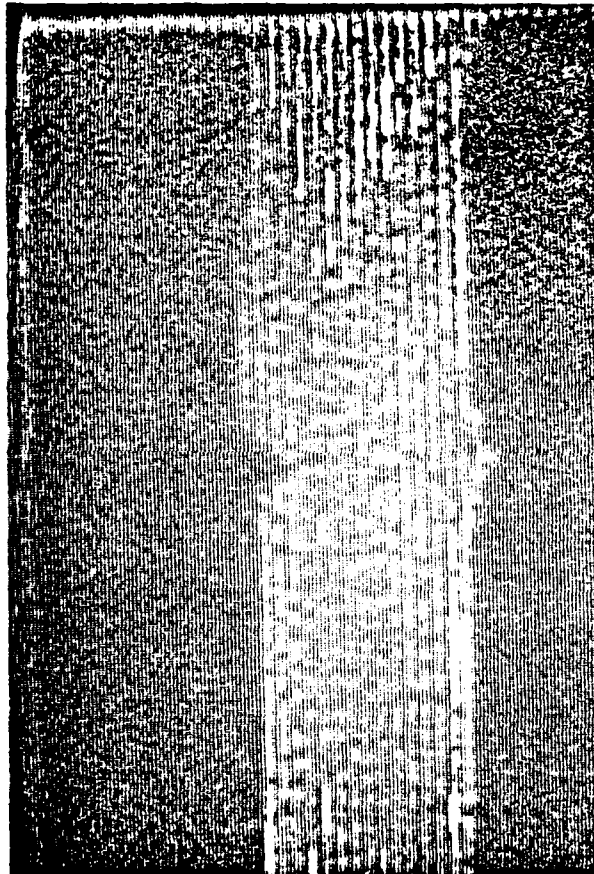


Figure 35A: Photograph of Video Recording of Thermographic Image
Taken just before failure and near maximum load (same
fatigue cycle as 8).

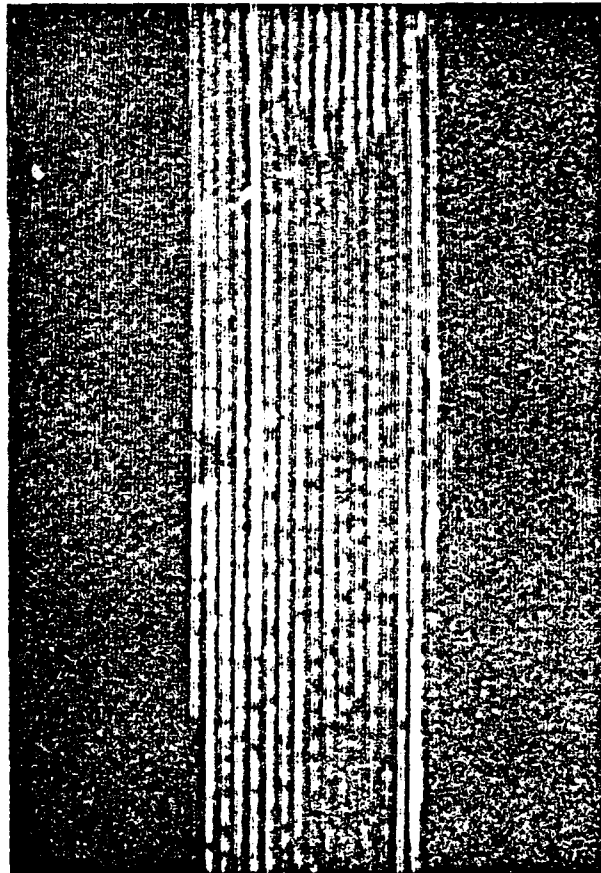


Figure 35B: Photograph of Video Recording of Thermographic Image
Taken just before failure and near minimum load (same as
fatigue cycle A).

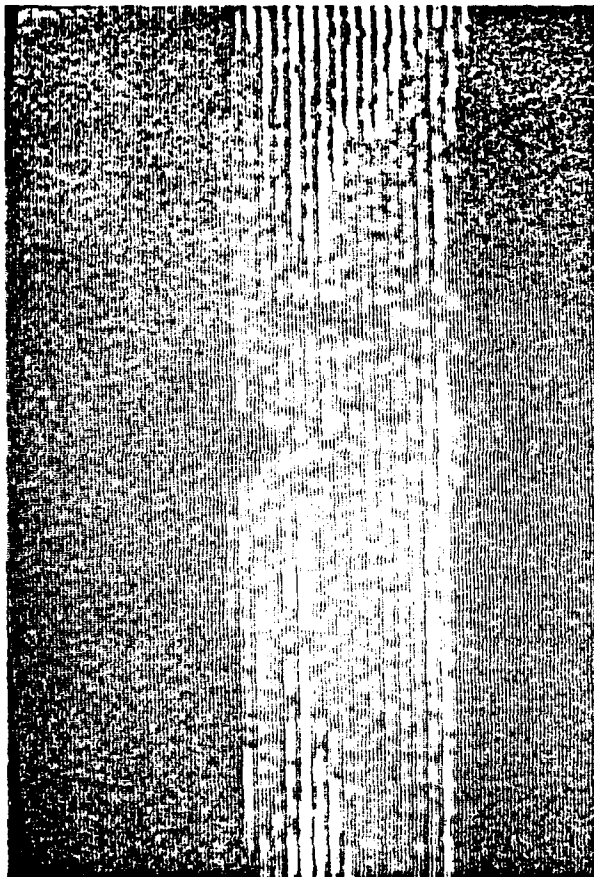


Figure 35C: Photograph of Video Recording of Thermographic Image
Taken at the instant of failure.

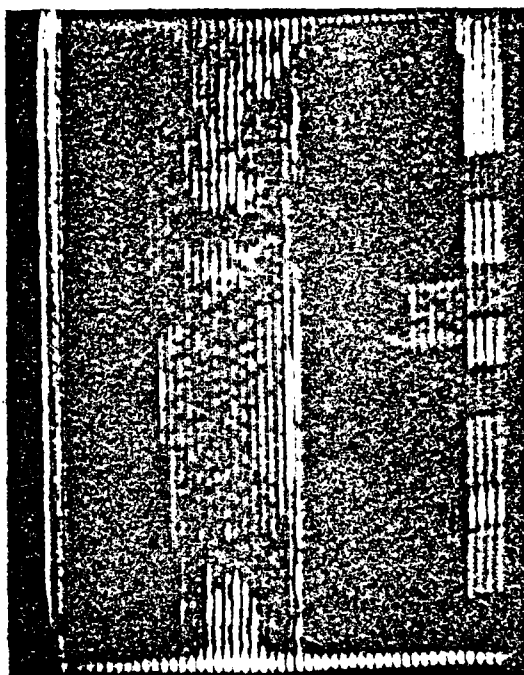


Figure 35D: Photograph of Video Recording of Thermographic Image
Taken about 1/2 second after failure.

Figure 35B shows the top (tension side) to be hotter near the minimum load. This heat is probably generated from friction effects in the crack surfaces. Figures 35C and D show thermographs at the first indication of failure and about 1/10 second thereafter, respectively. Notice the temperature scale at the bottom of Figure 35D. Each color change indicates a change of 0.2°C , the temperature increasing from left to right.

Several additional items must be noted here about the thermography. The thermal changes that occur in Figures 35A and B were detected with the video recording equipment. During fatigue of the unnotched specimens, the cyclic thermal pattern was not noticed because the video recording system was not implemented. However, the bottom of the specimen was generally observed to be hotter than the top. This implies that compression stresses as well as friction from the longitudinal crack interfaces generate heat.

Investigation of the longitudinal crack growth continued by examining the effects of notch depth and using more extensive NDE. The tests for specimens 16/4, 17/4, 12/5 and 23/5 were performed as explained in Section 2.5. Regardless of notch depth, a longitudinal crack grew in both directions from the notch tip. Therefore, the longitudinal crack was not directly related to the longitudinal striations. Tables 12, 13, 14 and 15 give the crack lengths detected by three NDE techniques, the flexural rigidity, percent stiffness change, fatigue load, and number of cycles for the four notched specimens, respectively. These values are plotted in Figures 36-47.

Figures 36 through 39 show the crack length detected by X-ray

Table 12: Bend Test Results for Notched Specimen 16/4

Cycles (K)	Load (lbs)	Crack Length (in)			E_f (Msi)	Stiffness % Change
		Replica	C-Scan	X-Ray		
0	---	---	---	---	25.55	---
10	70	---	---	---	26.36	+ 3.17
20	80	---	---	---	26.90	+ 5.28
30	90	.025	---	---	26.95	+ 5.48
40	100	.055	.105	.135	26.58	+ 4.03
50	110	.070	---	---	25.27	- 1.10
60	120	.225	.325	.300	24.74	- 3.17
70	130	.365	---	---	24.54	- 3.95
80	140	.515	.635	.570	24.08	- 5.91
90	150	.615	---	---	23.32	- 8.81
100	160	.715	.870	.810	22.14	-13.35
110	170	1.015	---	---	21.36	-16.40
120	180	1.110	1.275	1.125	20.44	-20.00
130	190	1.325	---	---	19.58	-23.37
131*	200	---	---	---	---	---

*Failure

Table 13: Bend Test Results for Notched Specimen 17/4

Cycles (K)	Load (lbs)	Crack Length (in)			E_f (Msi)	Stiffness % Change
		Replica	C-Scan	X-Ray		
0	---	---	---	---	26.42	---
10	88	---	---	---	28.46	+ 7.72
20	101	---	---	---	29.07	+10.03
30	113	---	---	---	29.57	+11.92
40	126	---	---	---	29.39	+11.24
50	138	.127	---	---	28.29	+ 7.08
60	151	.203	.250	.085	28.16	+ 6.59
70	163	.272	---	---	27.50	+ 4.09
80	176	.406	.475	.310	27.30	+ 3.33
90	189	.529	---	---	26.02	- 1.51
100	201	.738	.790	.755	24.96	- 5.53
110	214	.844	---	---	24.08	- 8.86
120	226	1.084	1.110	1.100	23.45	-11.24
130	239	1.229	---	---	23.26	-11.96
130.2*	252	---	---	---	---	---

*Failure

Table 14: Bend Test Results for Notched Specimen 12/5

Cycles (K)	Load (lbs)	Crack Length (in)			E_f (Msi)	Stiffness % Change
		Replica	C-Scan	X-Ray		
0	---	---	---	---	29.16	---
10	87	---	---	---	31.45	+ 7.85
20	99	---	---	---	31.38	+ 7.61
30	112	.035	---	---	31.57	+ 8.26
40	124	.180	.195	.125	31.39	+ 7.65
50	136	.235	---	---	29.27	+ 0.38
60	149	.385	.455	.410	28.73	- 1.47
70	161	.590	---	---	28.37	- 2.71
80	173	.730	.750	.745	27.96	- 4.12
90	186	.960	---	---	26.82	- 8.02
100	198	1.180	1.235	1.245	25.90	-11.18
110	211	1.555	---	---	24.57	-15.74
111.1*	223	---	---	---	---	---

*Failure

Table 15: Bend Test Results for Notched Specimen 23/5

Cycles (K)	Load (lbs)	Crack Length (in)			E_f (Msi)	Stiffness % Change
		Replica	C-Scan	X-Ray		
0	---	---	---	---	26.49	---
10	70	---	---	---	29.32	+10.68
20	80	---	---	---	29.08	+ 9.78
30	90	.010	---	---	28.83	+ 8.83
40	100	.050	.115	.105	28.18	+ 6.38
50	110	.140	---	---	27.10	+ 2.30
60	120	.315	.400	.440	26.18	- 1.17
70	130	.518	---	---	24.64	- 6.98
80	140	.716	.805	.770	23.11	-12.76
80.4*	150	---	---	---	---	---

*Failure

radiography, C-scan and replication. It can be noted that a correlation exists between the measured crack length and the respective NDE technique. For instance the length detected by ultrasonic C-scan was generally slightly longer than the crack length detected by X-ray radiography, which was in turn slightly longer than length detected by replication. These differences will be discussed in more detail later. The crack growth rate (slope of Figures 36-38) increases with the number of cycles. This increase is consistent with the fact that the fatigue load is increased with increments of cycles.

Figures 40 through 43 show the percent stiffness change plotted versus the total number of fatigue cycles. As found in the unnotched specimens the stiffness at first, increases with fatigue due to matrix work-hardening. After additional fatigue cycles the stiffness drops, primarily due to the growth of the longitudinal crack.

To show the effect of the longitudinal crack, the flexural rigidity, E_f , was plotted against crack length in Figures 44 through 47. Assuming the crack of length C reduces the effective moment of inertia of the beam to I_E and applying beam theory; the maximum deflection can be written as:

$$\Delta = \frac{PL^3}{48EI} + \frac{PL^3}{48E} \left(\frac{1}{I_E} - \frac{1}{I} \right) \left\{ 4 \frac{C}{L} - 4 \frac{C^2}{L^2} + \frac{C^3}{L^3} \right\} \quad (6)$$

I_E is the effective moment of inertia considering the reduction of the beam height by the longitudinal crack depth. Substituting the value of deflection from equation (6) into equation (4), the theoretical curves shown in Figures 44 through 47 are developed. These curves show the

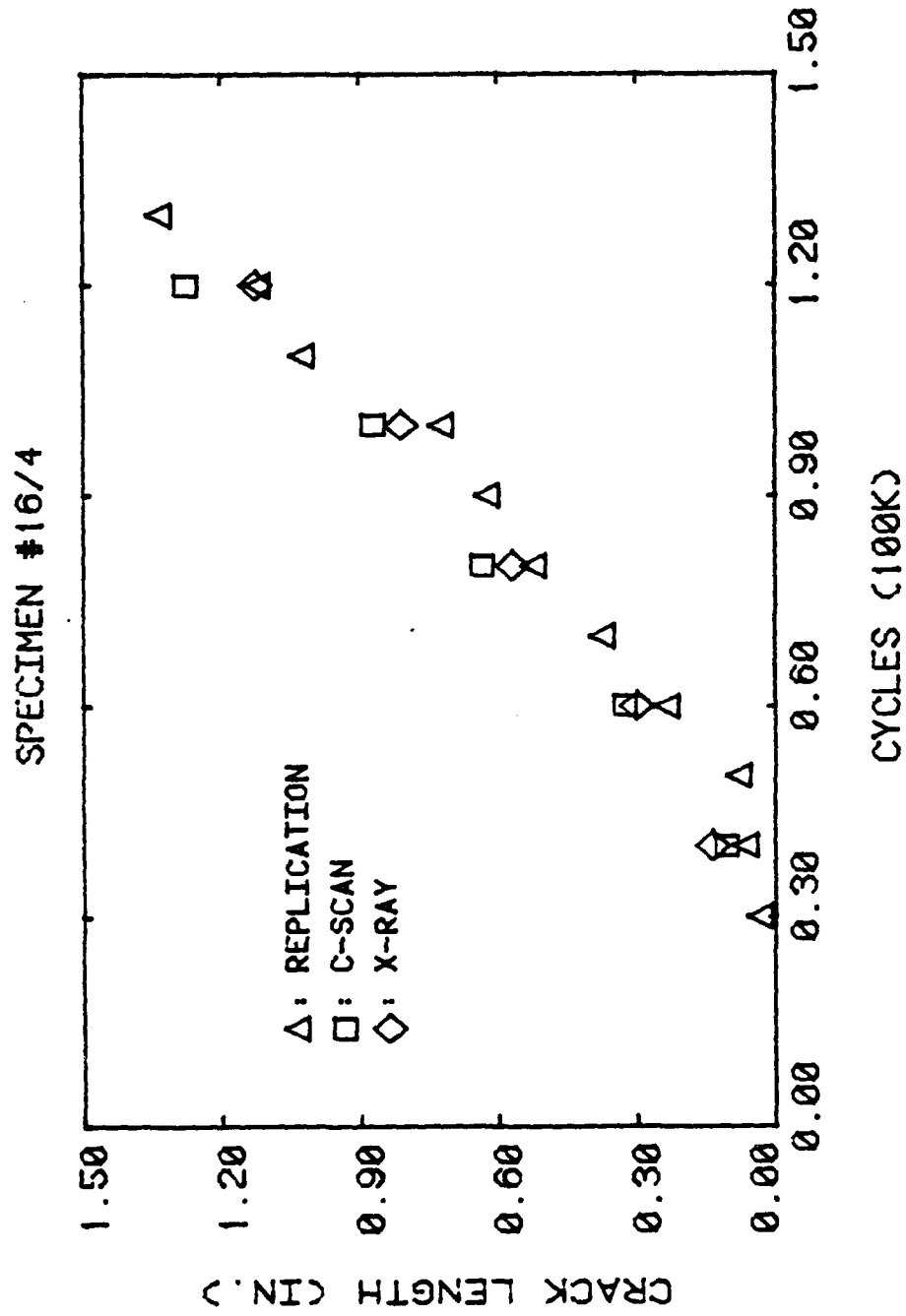


Figure 36: Longitudinal Crack Length detected by three NDE Techniques

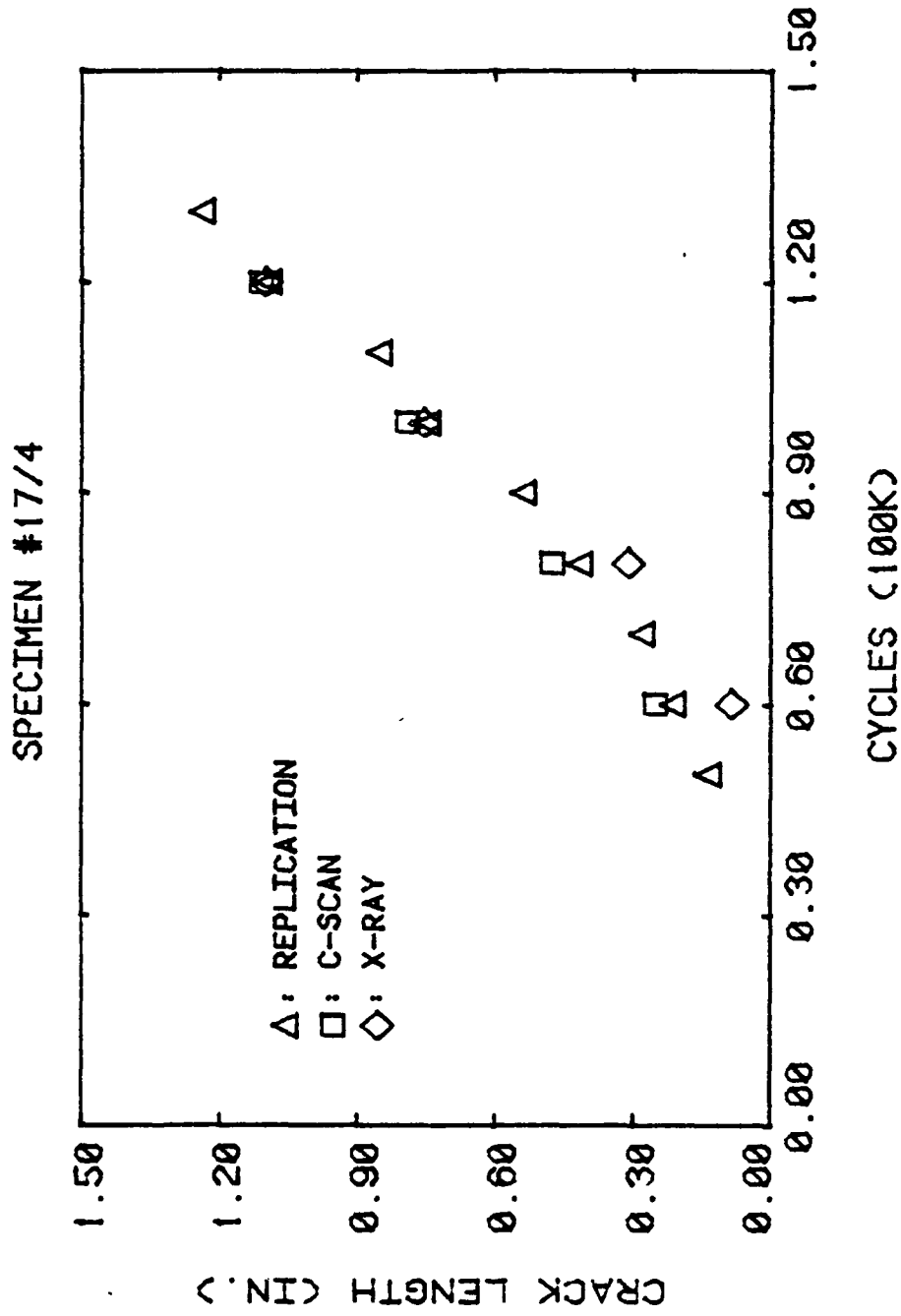


Figure 37: Longitudinal Crack Length detected by three NDE Techniques

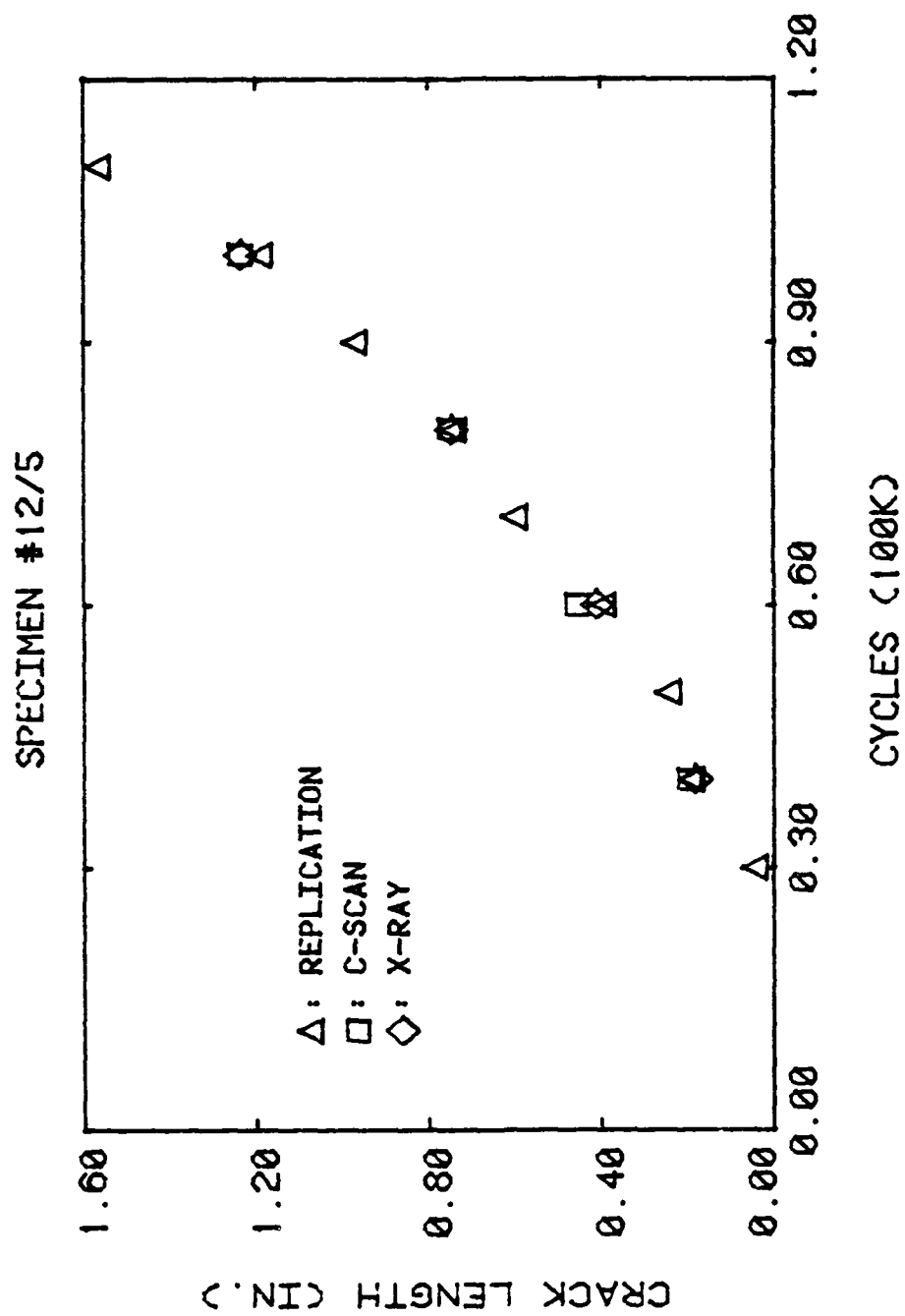


Figure 38: Longitudinal Crack Length detected by three NDE Techniques

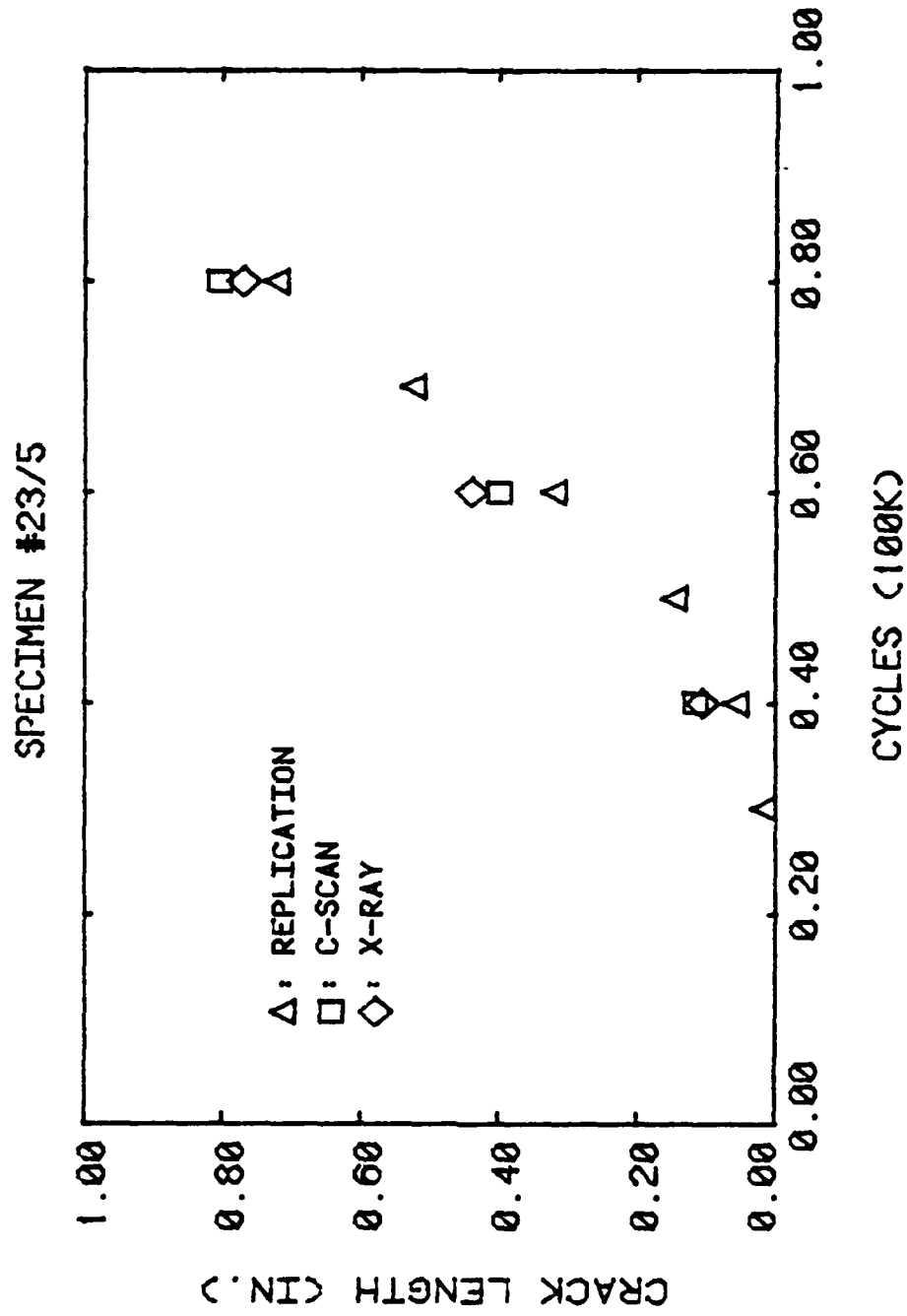


Figure 39: Longitudinal Crack Length detected by three NDE Techniques

SPECIMEN #16/4

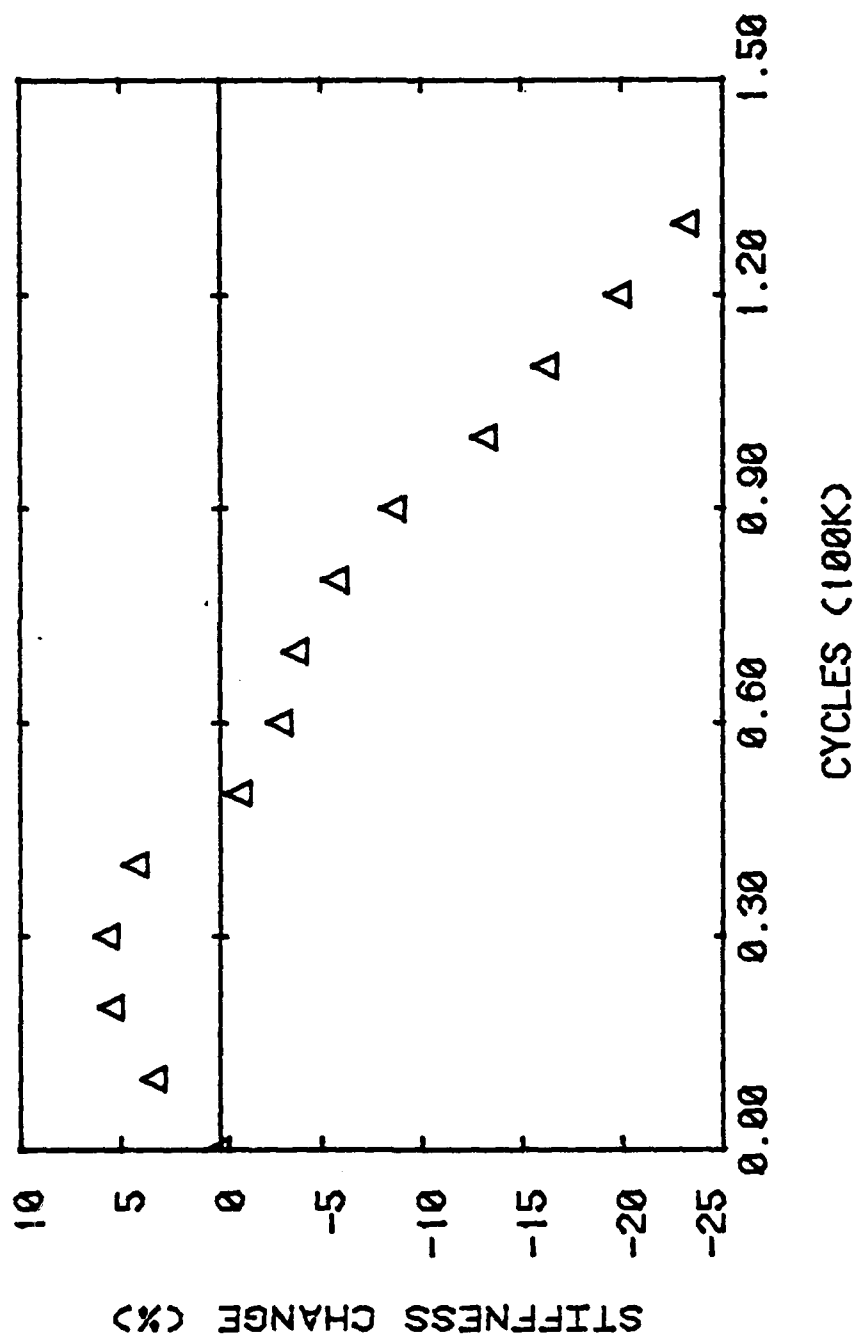


Figure 40: Percent Stiffness Change versus Cycles of Loading in Bend Test

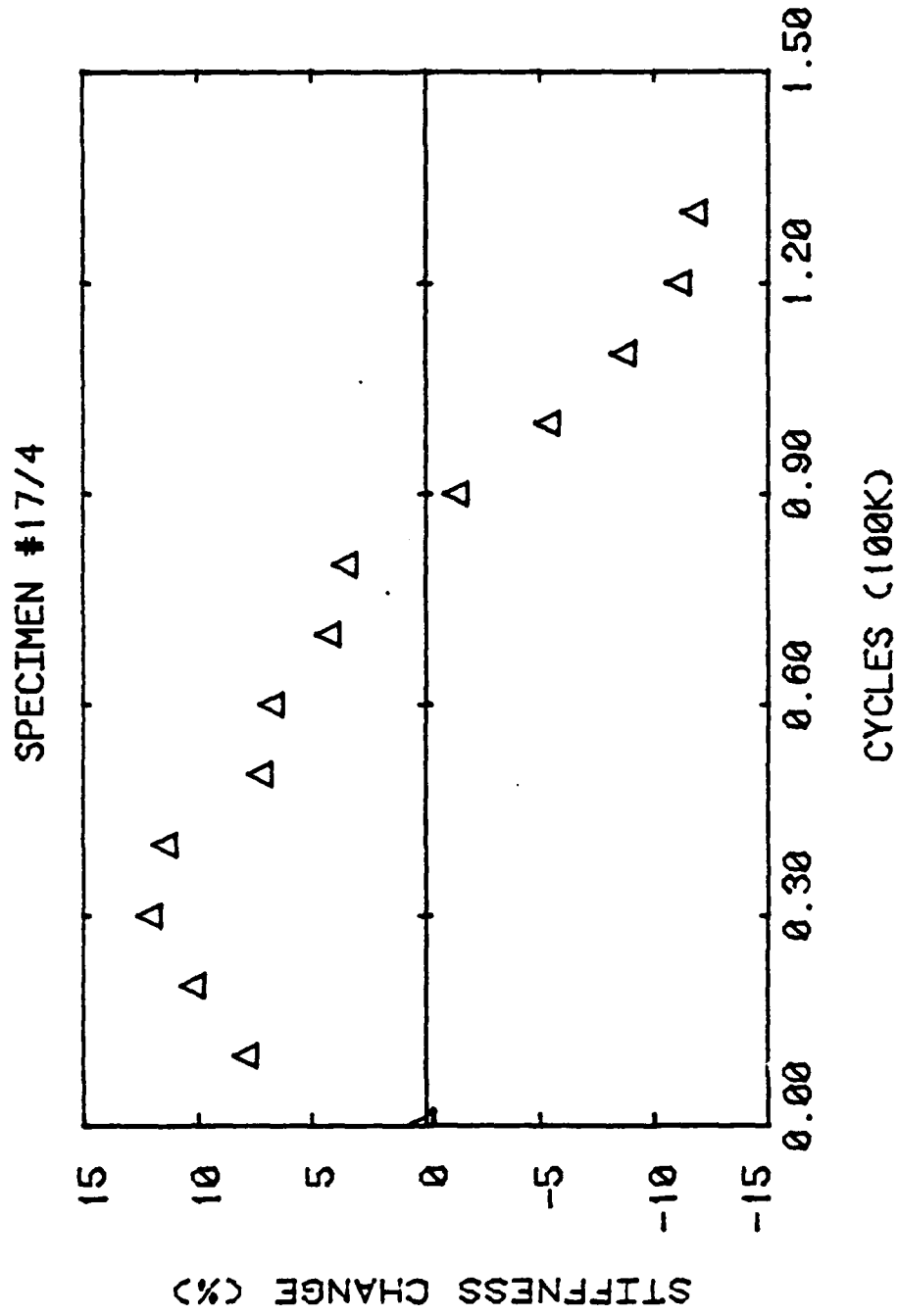


Figure 41: Percent Stiffness Change versus Cycles of Loading in Bend Test

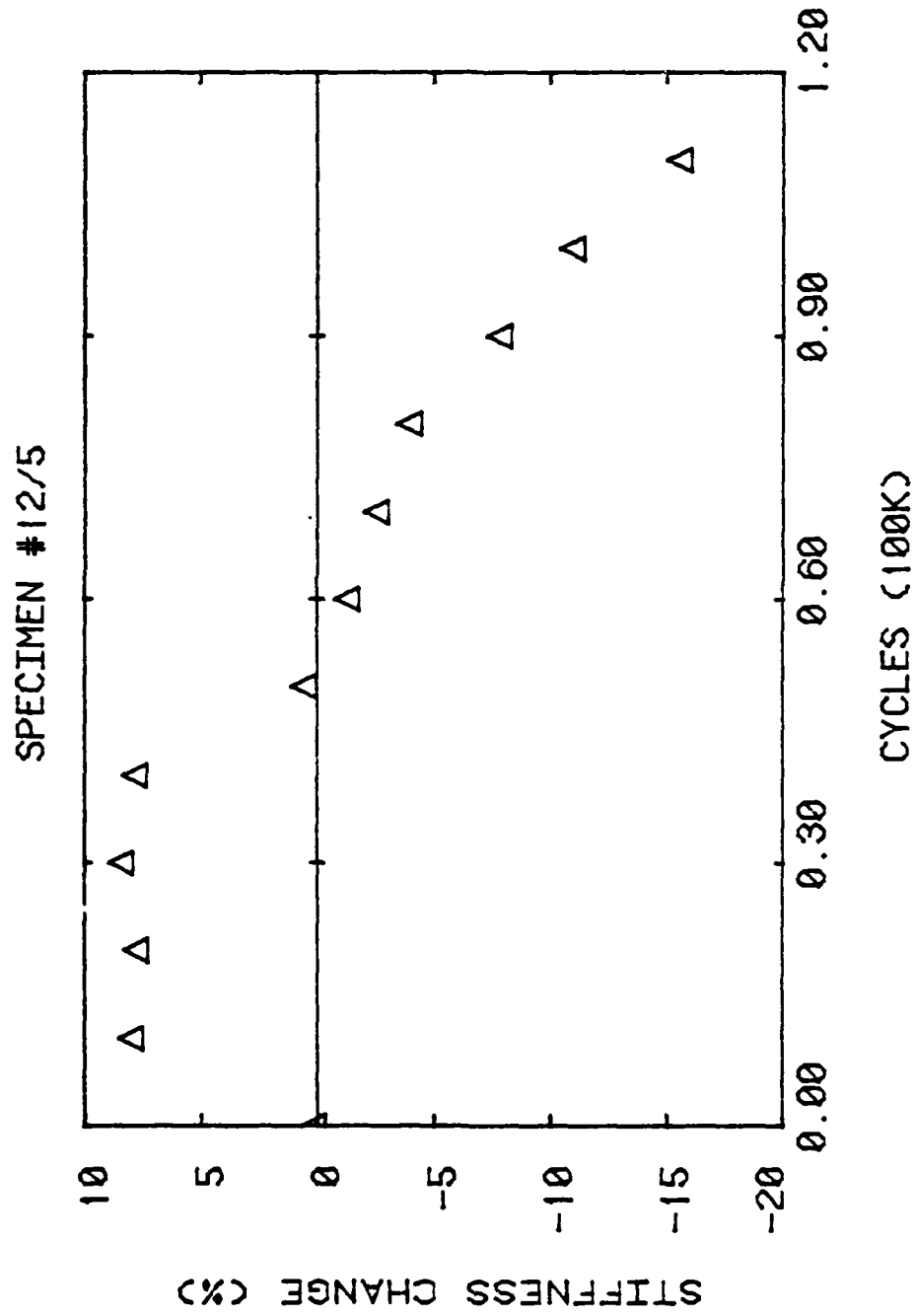


Figure 42: Percent Stiffness Change versus Cycles of Loading in Bend Test

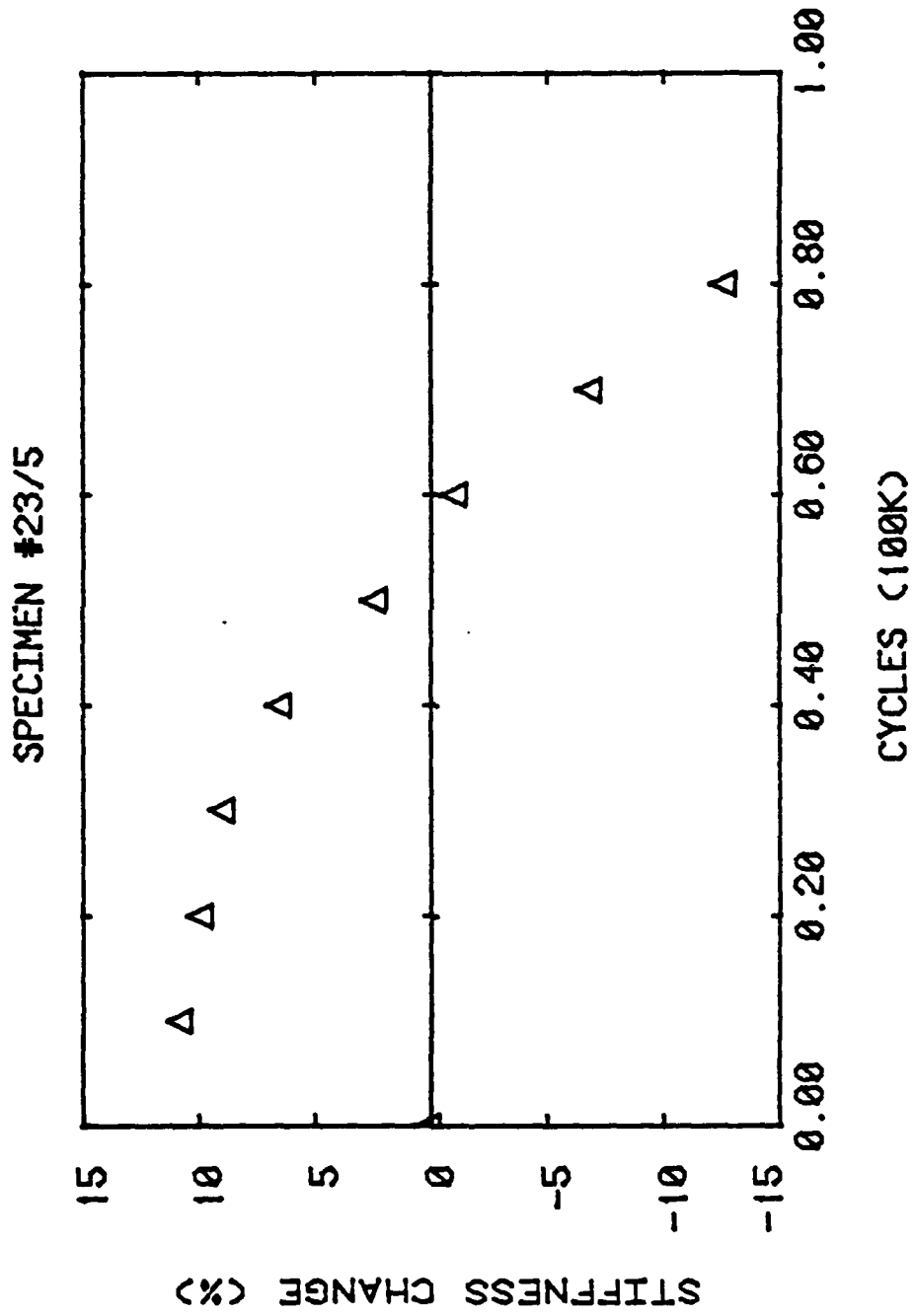


Figure 43: Percent Stiffness Change versus Cycles of Loading in Bend Test

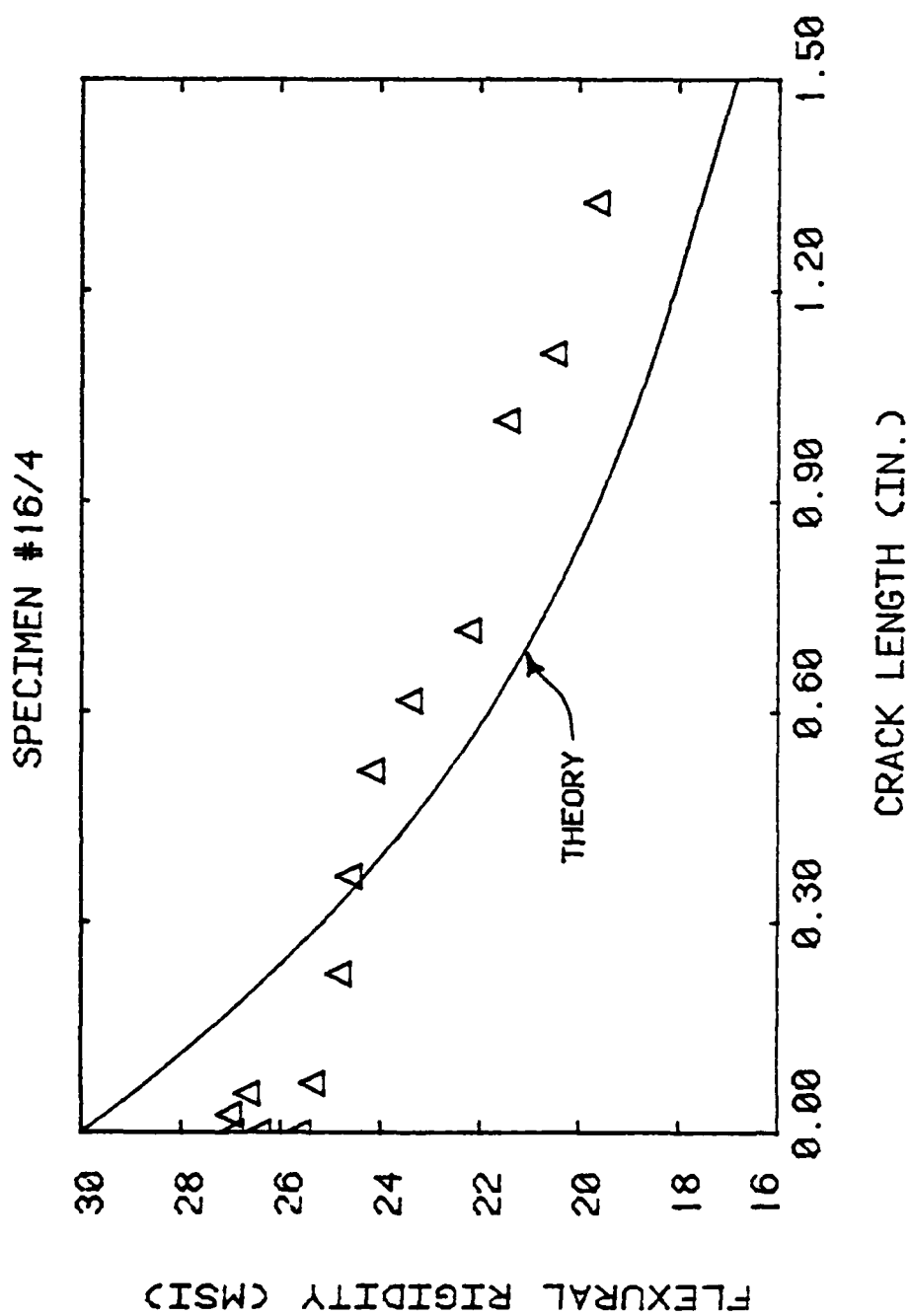


Figure 44: Experimental (points) and Theoretical (line) Stiffness versus Longitudinal Crack Length

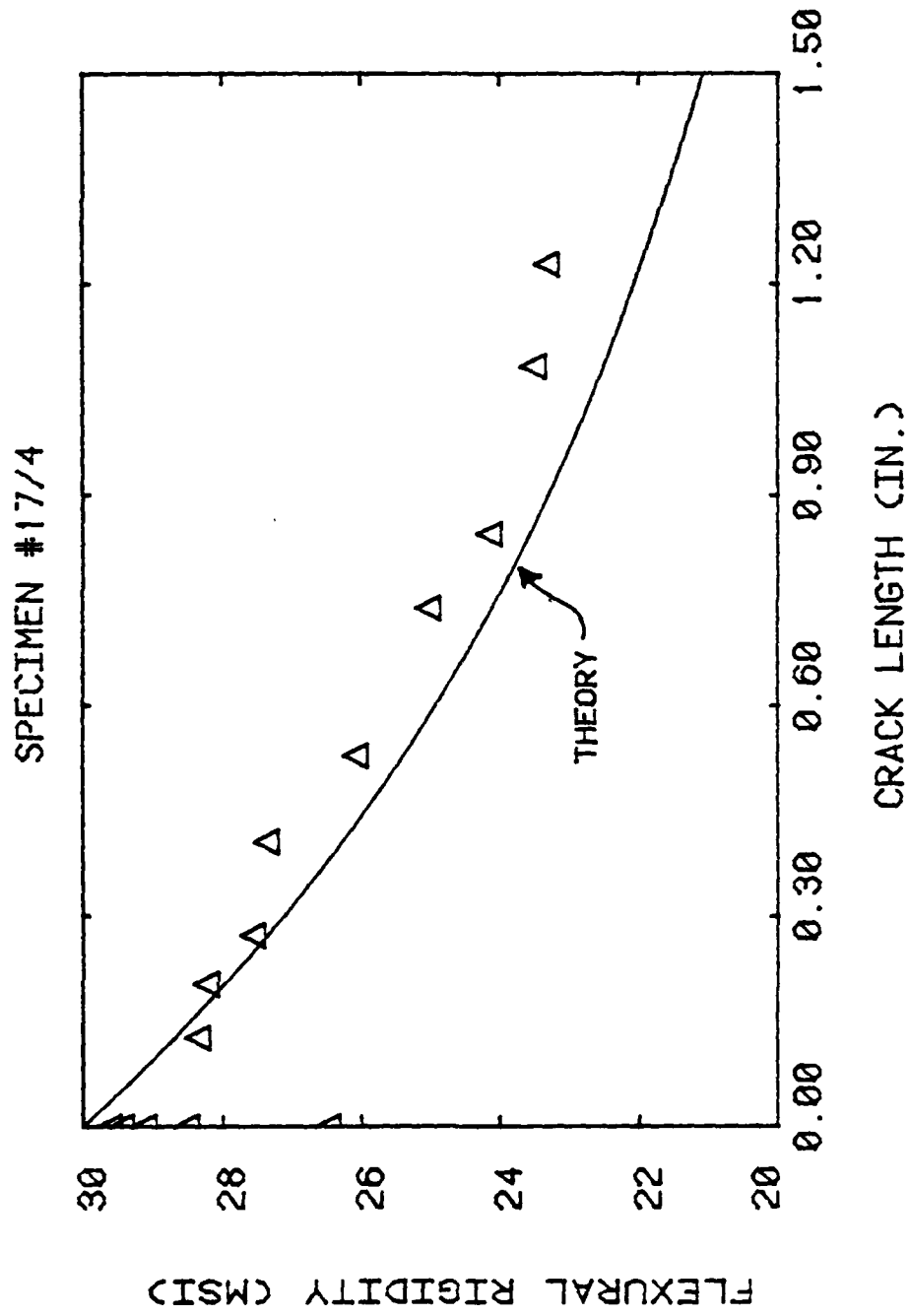


Figure 45: Experimental (points) and Theoretical (line) Stiffness versus Longitudinal Crack Length

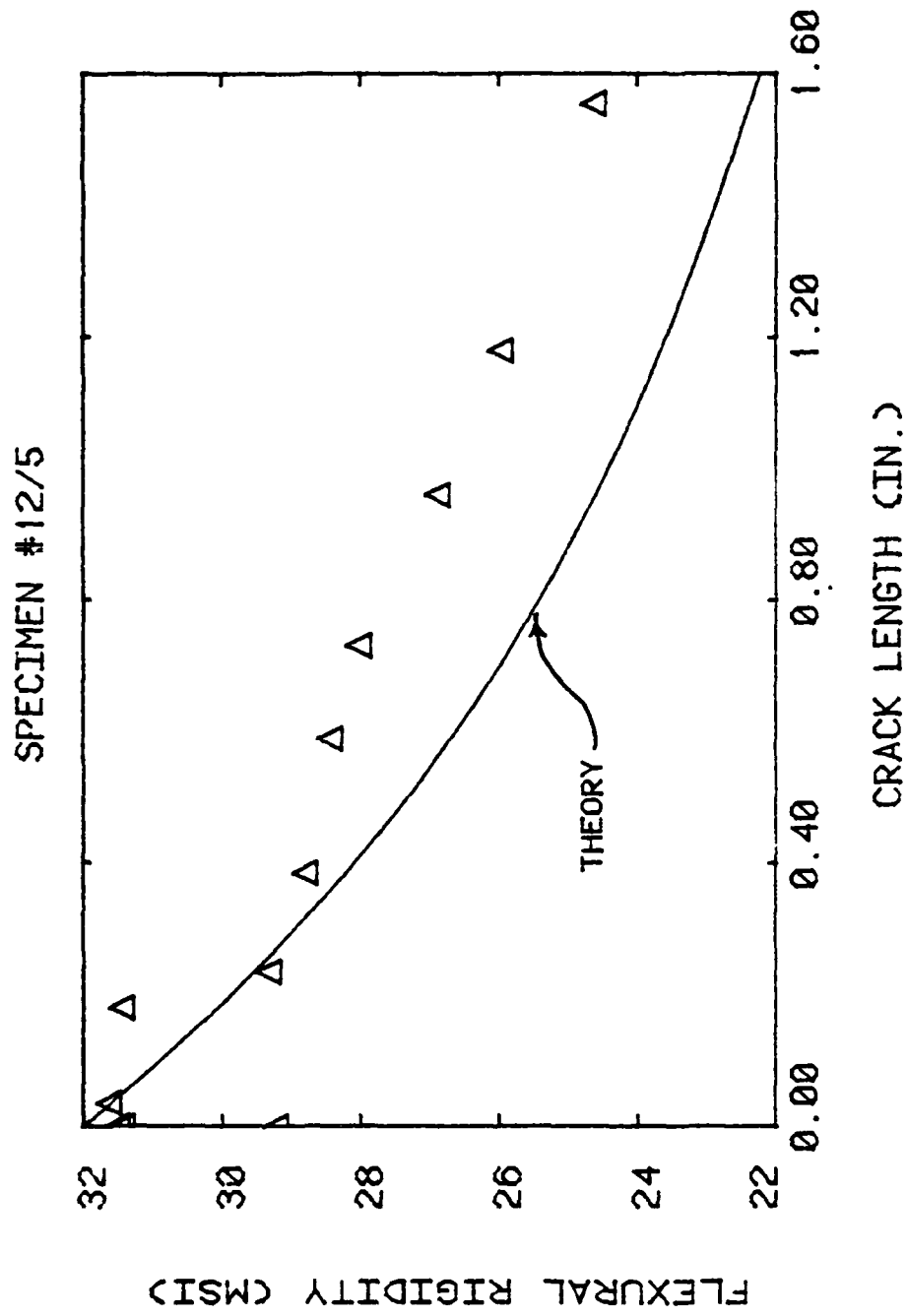


Figure 46: Experimental (points) and Theoretical (line) Stiffness versus Longitudinal Crack Length

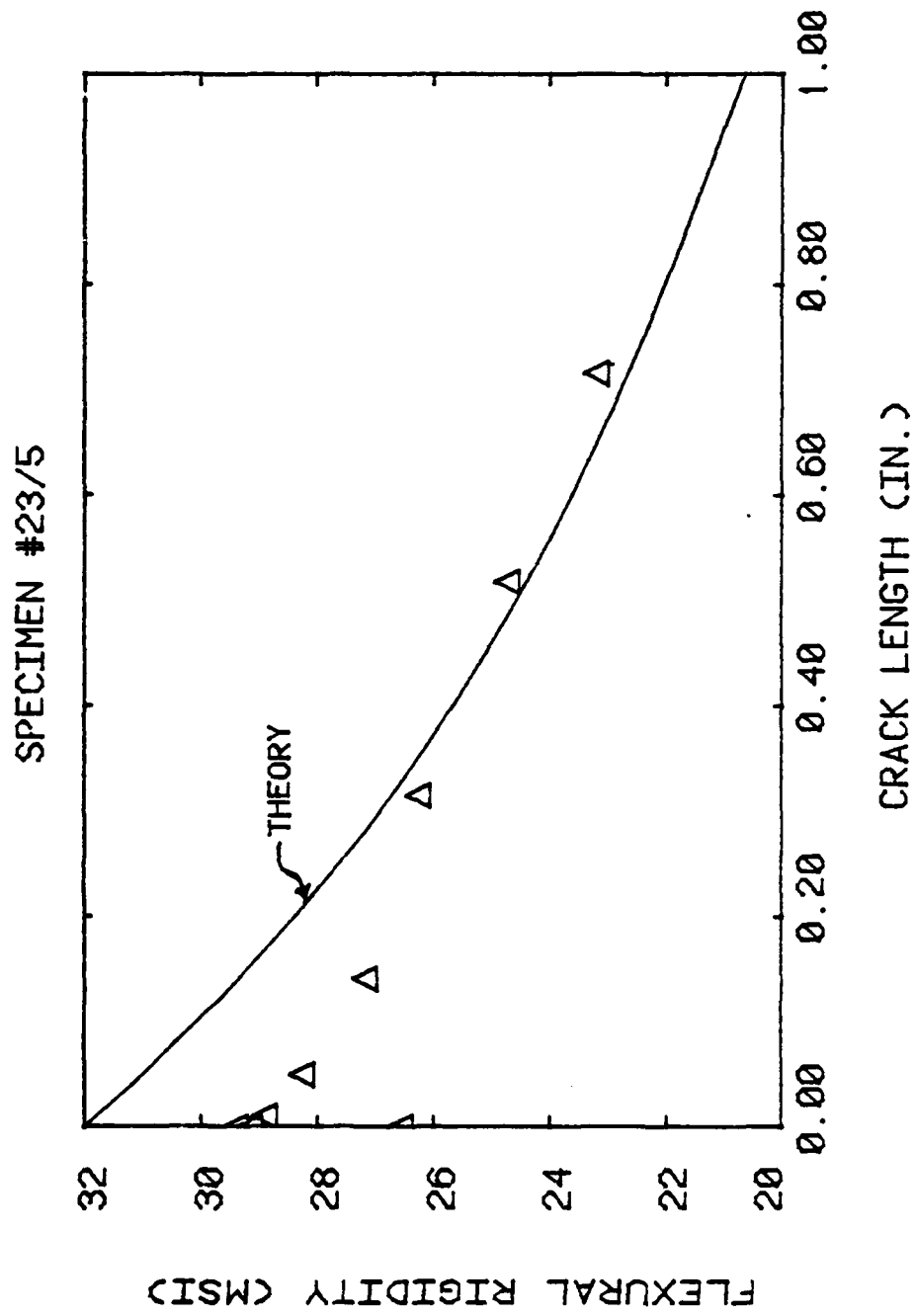


Figure 47: Experimental (points) and Theoretical (line) Stiffness versus Longitudinal Crack Length

theoretical flexural stiffness reduction due to the reduction of the effective moment of inertia of the beam. The modulus of the material, in equation (6), is assumed to be 30 Msi and 32 Msi for 45% V_f and 55% V_f , respectively. Note that this does not account for the stiffness increase that occurred in all specimens due to matrix work hardening. This may be one reason why the experimental points are slightly higher than the theory. However, the relationship between theory and experiment shows that stiffness change can be used not only to detect damage but to quantify the extent of damage development.

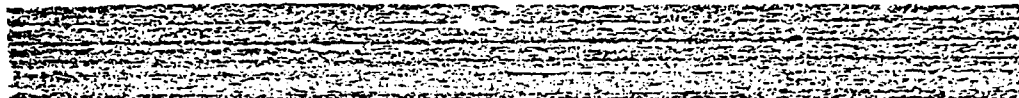
Figure 48 shows the complete C-scan history (trigger level 5-1/2) for specimen 16/4. Note that the longitudinal crack is oriented parallel to the path of the ultrasonic beam. Therefore, the detection of the crack is believed to be primarily due to scattering of the beam by the crack. Also, the crack appears to be much wider than it actually is. This is due to scattering of the ultrasonic beam and/or absorption due to damage created in the region surrounding the crack. For the same reasons, the C-scan technique generally detected a longer crack length than the other NDE methods.

Replication indicated the presence of a transverse crack growing from the notch tip to the longitudinal crack. Figure 49 shows an initial replica of specimen 23/5; Figure 50 indicates the presence of a transverse crack, and Figure 51 shows the transverse crack blunted by the presence of a longitudinal crack running in both directions. Notice that the longitudinal crack is not continuous in Figure 51. By sectioning perpendicular to the longitudinal crack, this discontinuity was found to exist only at the replicated edge. The sectioned piece indicated

110



0 CYCLES



20K CYCLES



40K CYCLES



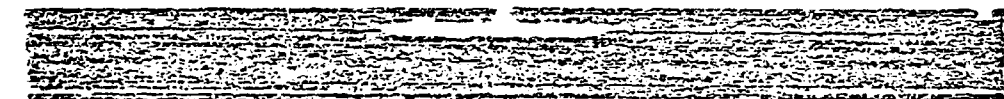
60K CYCLES



80K CYCLES



100K CYCLES



120K CYCLES

Figure 48: C-scan History of Notched specimen 16/4.
(Trigger Level 5-1/2)



Figure 49: Reproduction of Initial Edge Replica of Specimen 23/5
(24 X)

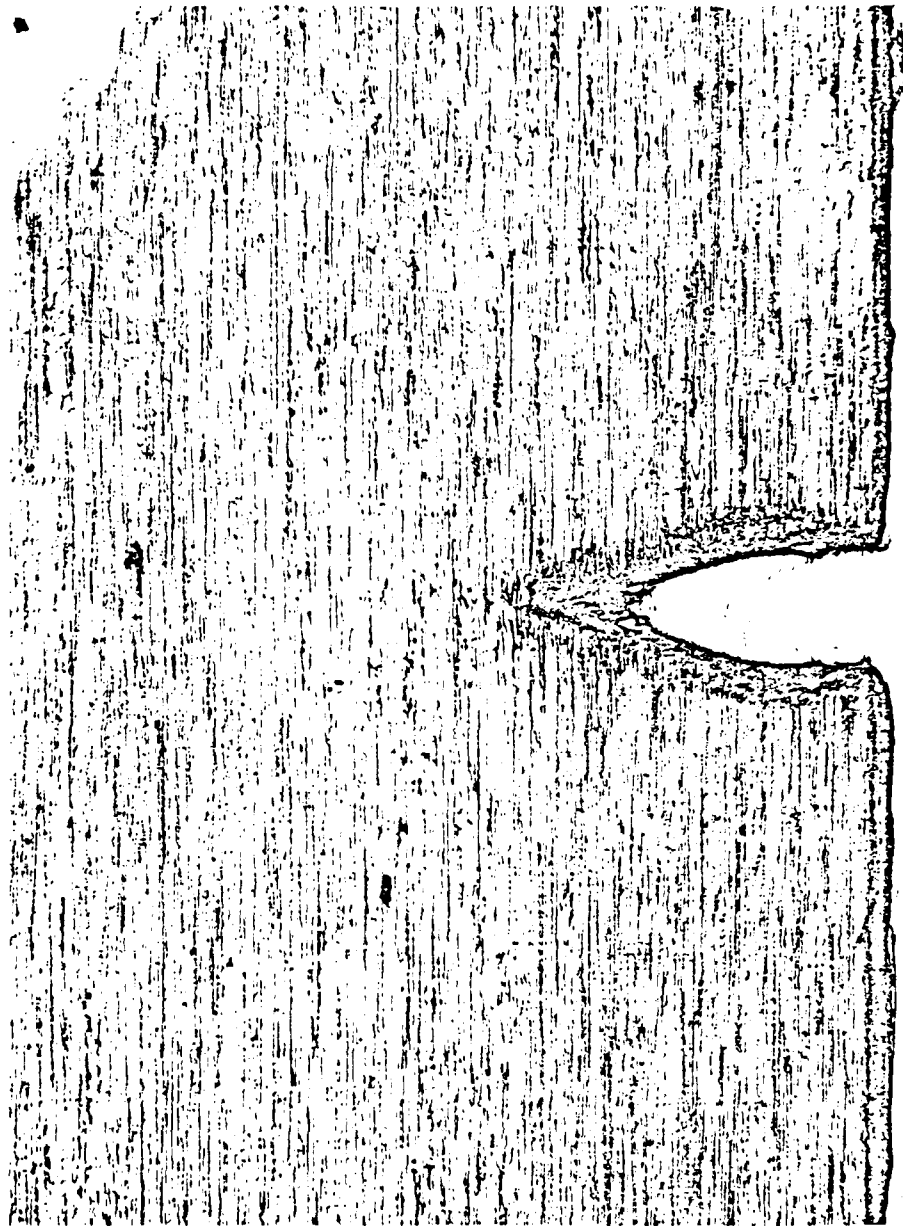


Figure 50: Reproduction of Edge Replica of Specimen 23/5 after 30K Cycles (24X)

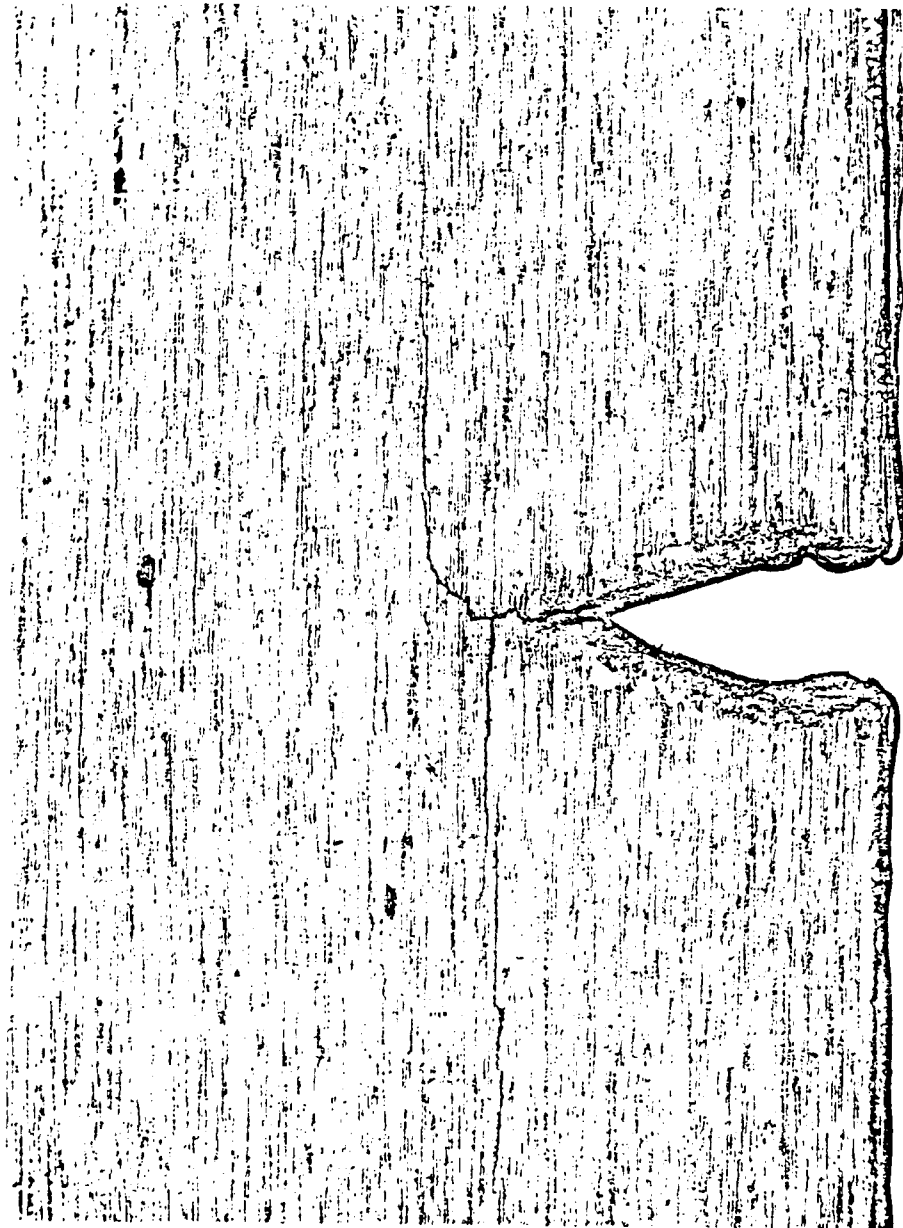


Figure 51: Reproduction of Edge Replica of Specimen 23/5 after 60K Cycles (24X)

that the side with the deeper crack quickly slanted back to the same depth as the other side. Figures 52, 53 and 54 show transverse cracks between the notch and the longitudinal crack for specimens 12/5, 16/4 and 17/4, respectively. Table 16 lists the notch depth and maximum and minimum bounds on longitudinal crack depth and transverse crack length. The crack depth measurements are taken from sections of the failure surface and the transverse crack length calculated as the difference of the longitudinal crack depth and the notch depth. Maximum and minimum values are given because of the variance in longitudinal crack depth across the surface. The table also indicates that the transverse cracks were about 0.005 to 0.010 inches long. The high value of maximum transverse crack length for specimen 23/5 is due to the discontinuity shown in Figure 51.

3.4 Scanning Electron Microscopy

In order to obtain a better understanding of the failure of FP/Al, scanning electron micrographs were taken on several fracture surfaces. The scanning electron microscopy (SEM) results are shown in Figures 55 through 68. Figures 55 and 56 show manufacturing defects found on failure surfaces. Matrix voids, similar to the one shown in Figure 55, were found in all specimens, while Figure 56 shows the largest matrix rich region found.

There were three distinct types of regions detected on failure surfaces: catastrophic failure zones, longitudinal fatigue cracks and transverse fatigue cracks. On some unnotched fatigue specimens a transverse fatigue crack propagated until it reached critical length where catastrophic or almost instantaneous failure occurred. In other

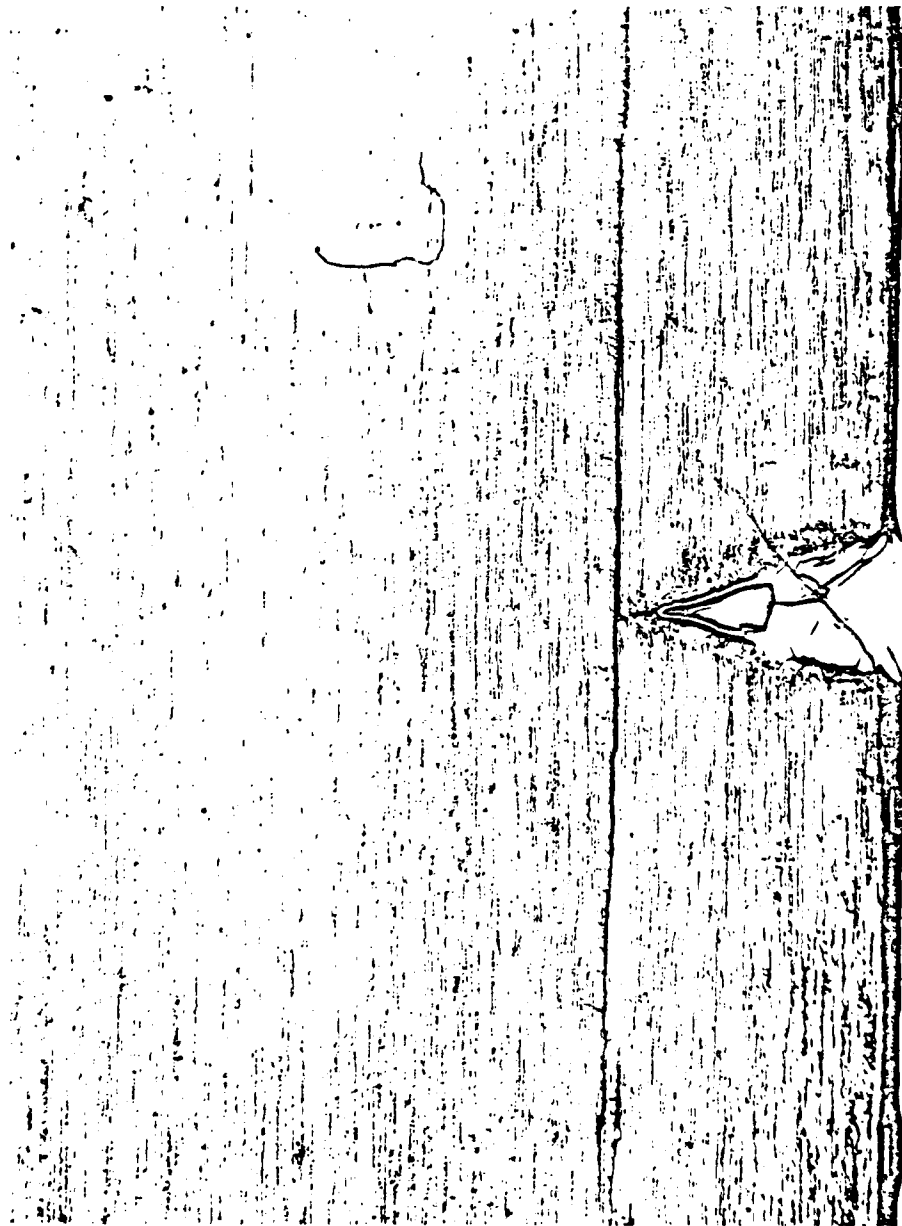


Figure 52: Reproduction of Edge Replica of Specimen 12/5 after 70K Cycles (24X)

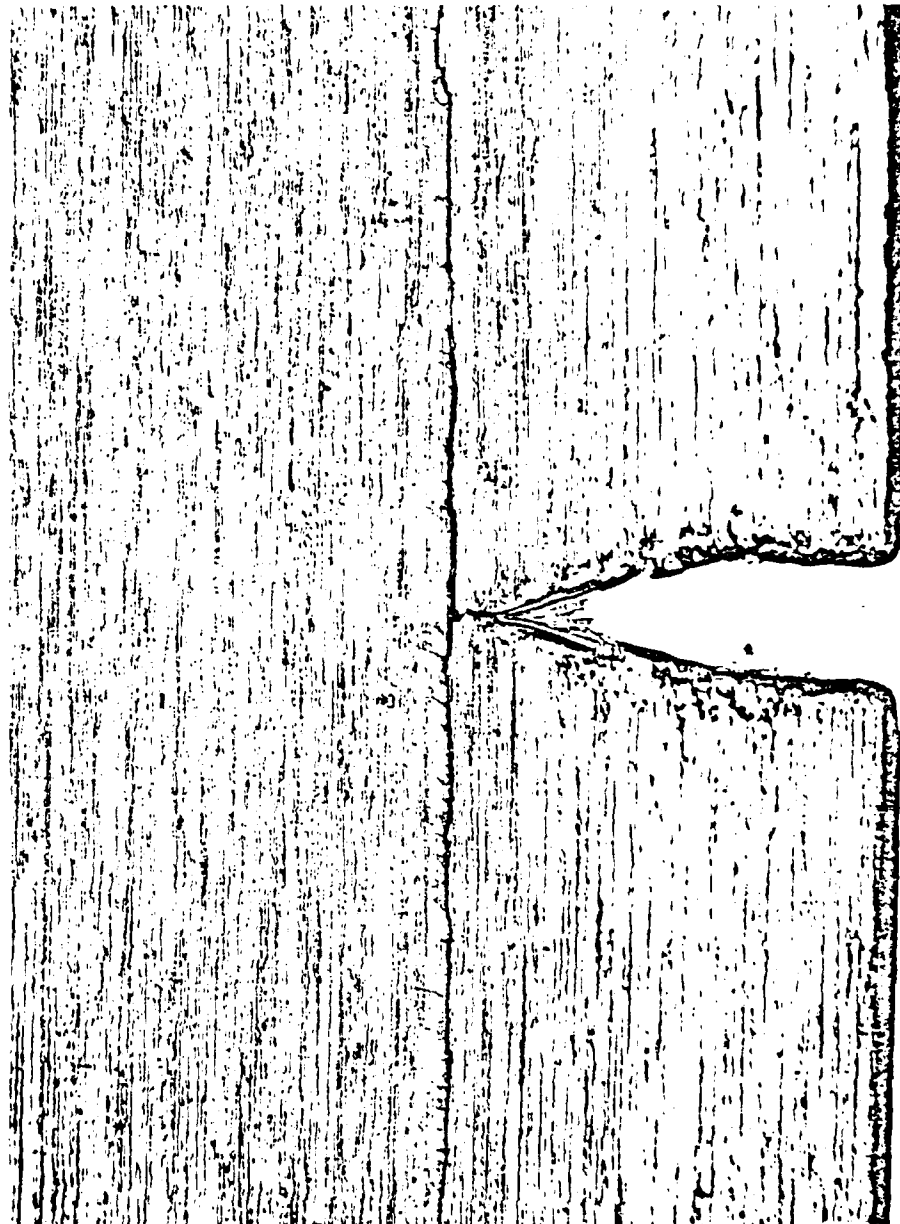


Figure 53: Reproduction of Edge Replica of Specimen 16/4 after 90K Cycles (24X)

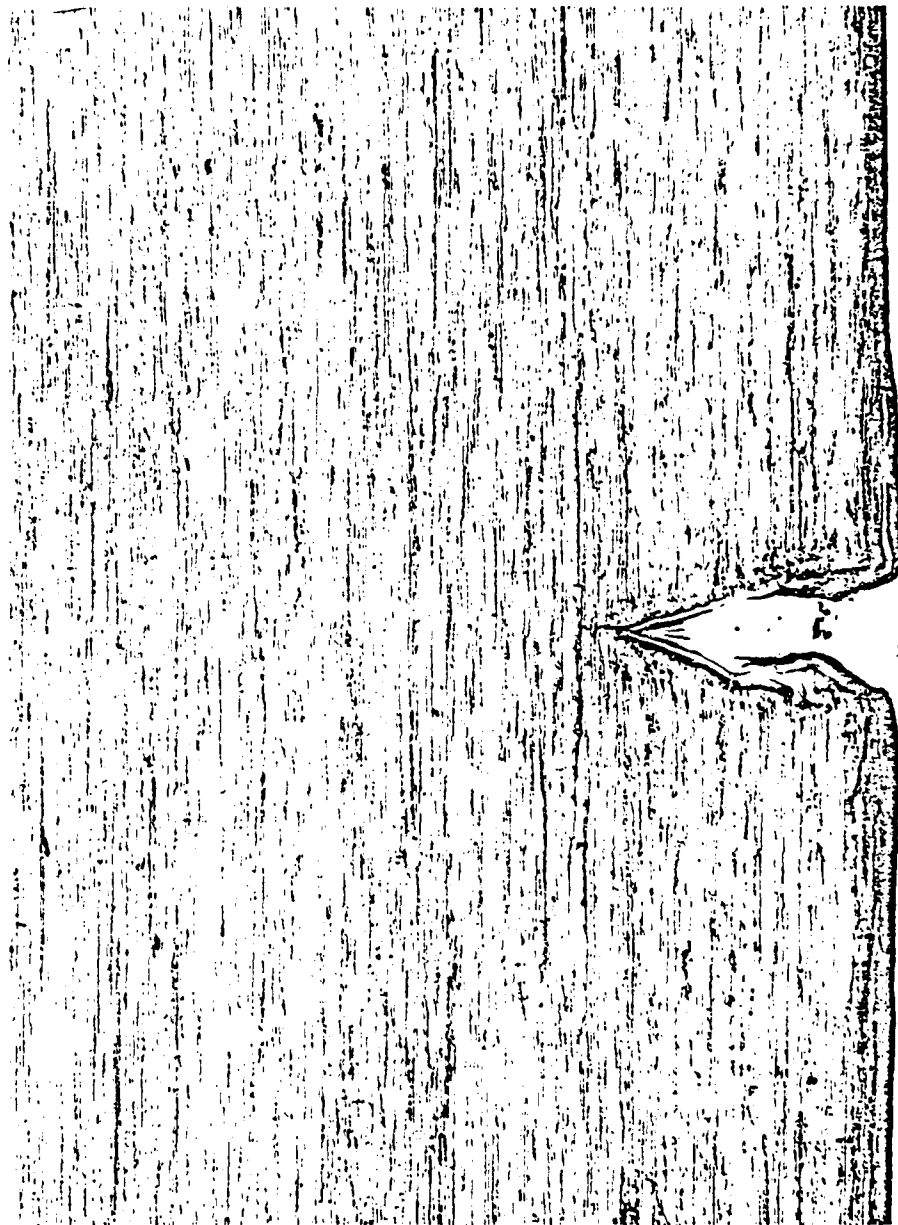


Figure 54: Reproduction of Edge Replica of Specimen 17/4 after 60K Cycles (24X)

Table 16: Longitudinal Crack Depth and Transverse Crack Length

Specimen	Notch Depth (in)	Longitudinal Crack Depth		Transverse Crack Length	
		Maximum (in)	Minimum (in)	Maximum (in)	Minimum (in)
12/5	.060	.068	.060	.008	.000
21/5	.090	.100	.095	.010	.005
23/5	.090	.115	.100	.025	.010
16/4	.100	.112	.106	.012	.006
17/4	.065	.075	.071	.010	.006
21/4	.100	.110	.105	.010	.005

Note: Longitudinal crack depth minus transverse crack length is equal to the notch depth.

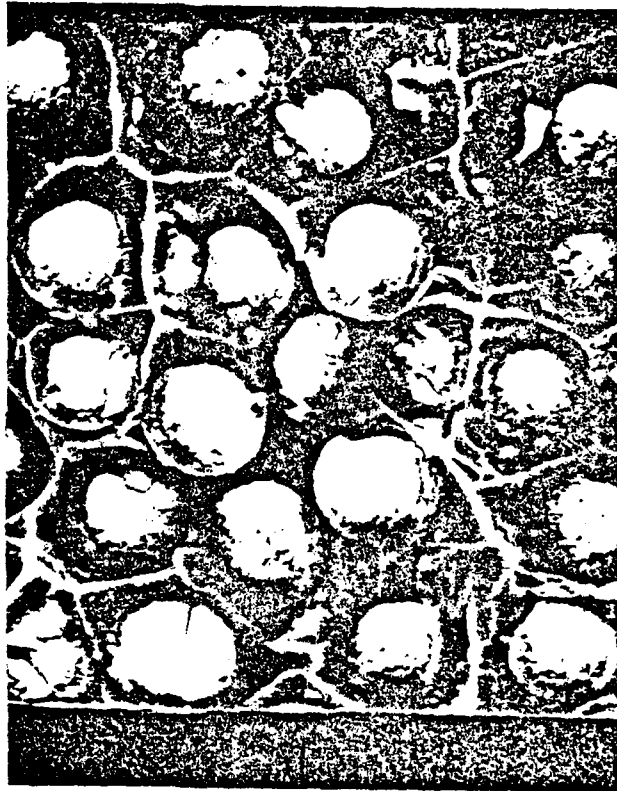


Figure 55: Matrix Void found on the catastrophic failure surface of specimen 21/5 (1000X)



Figure 56: Matrix Rich Region with an interior void found in the catastrophic failure region of specimen 3/4 (500X)

fatigue specimens no observable fatigue crack was found; the fracture surface was completely dominated by the catastrophic failure mode. The notched specimen had all three modes. A transverse crack grew from the notch tip to a longitudinal crack until catastrophic failure occurred in a transverse direction across the remainder of the specimen width.

Catastrophic failure, shown in Figures 55 through 58, was characterized by the ductile shear surfaces and large plastic deformation of the matrix. Also, fiber breakage appears to be very brittle (Figure 58). Figures 59 and 60 show longitudinal cracks that existed in the notched specimen. At the top of Figure 59 the surface where the failure began to propagate catastrophically across the remaining specimen width is shown. Notice that the longitudinal crack extends beyond this surface. Figures 61-67 show transverse fatigue cracks that grew from the notch tip or down from the tension side of the specimen.

Figure 61 is interesting because it is on the boundary between the region of catastrophic failure and fatigue crack growth. Notice the matrix crack that separates the two zones (Figure 61). Figure 62 shows roughness and fiber pullout in a fatigue crack zone and also a small region of catastrophic failure characterized by ductile matrix behavior. Lines that appear in Figure 63 are actually caused by the topology of the fiber failures. The rough topology is a characteristic of the fatigue crack zones. Fibers break at different places and at different times thus creating the appearance of lines (Figure 63), which really are graduations or steps in the level of the failure surface as shown in Figure 62.

Figures 64, 65 and 68 show fatigue cracks in unnotched specimens

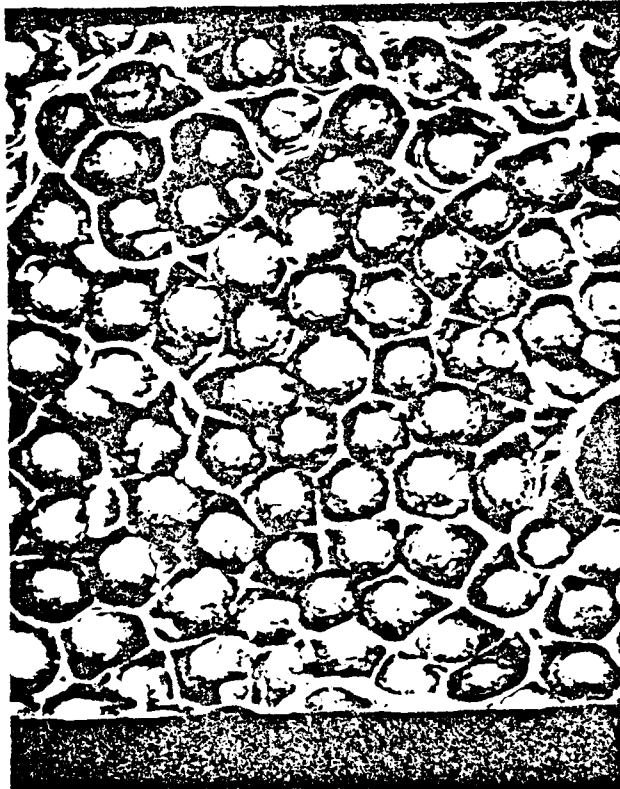


Figure 57: Catastrophic Failure Surface of specimen 21/6 (500X)

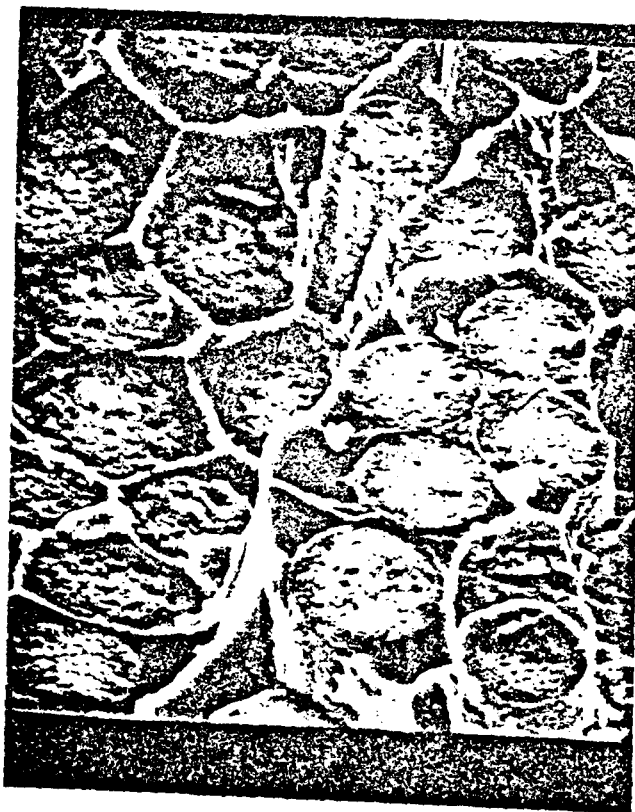


Figure 58: Ductile matrix behavior during catastrophic failure found on specimen 15/5 (1000X)



Figure 59: Longitudinal fatigue crack found on specimen 21/5 (500X)

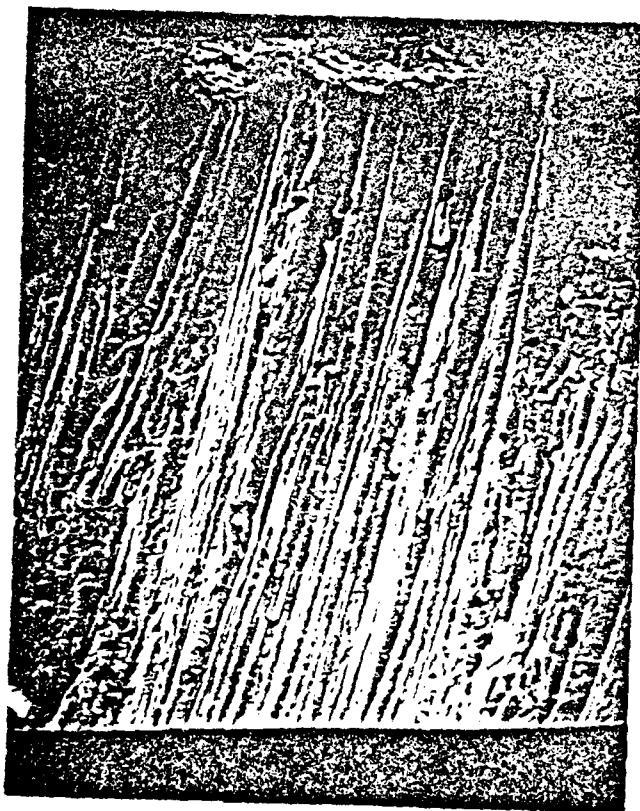


Figure 60: Longitudinal Fatigue Crack found on specimen 21/5 (100X)

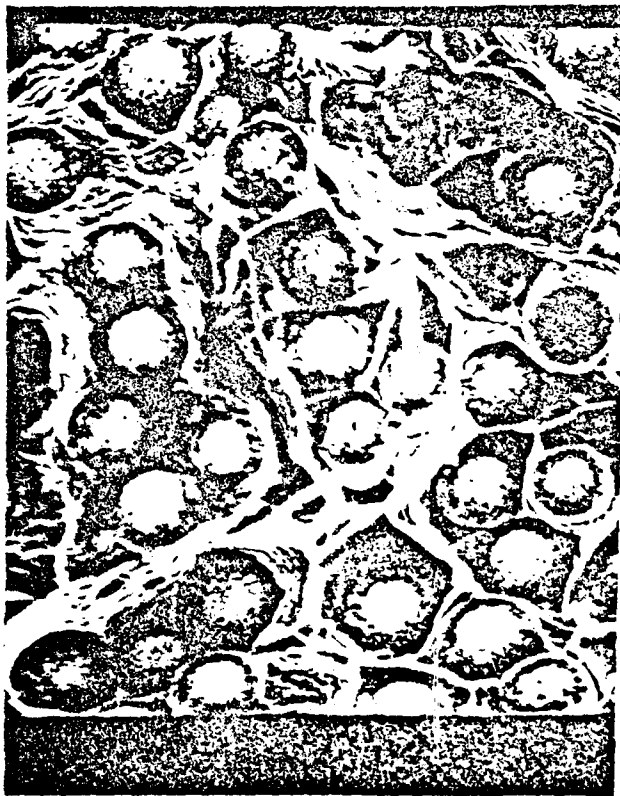


Figure 61: Ductile Matrix Failure (lower left) separated from a Fatigue Crack Failure zone by what appears to be a Matrix Crack, found on specimen 9/4 near tensile edge. (700X)



Figure 62: Surface Roughness and Fiber Pullout on specimen 15/5 near tensile edge (300X)

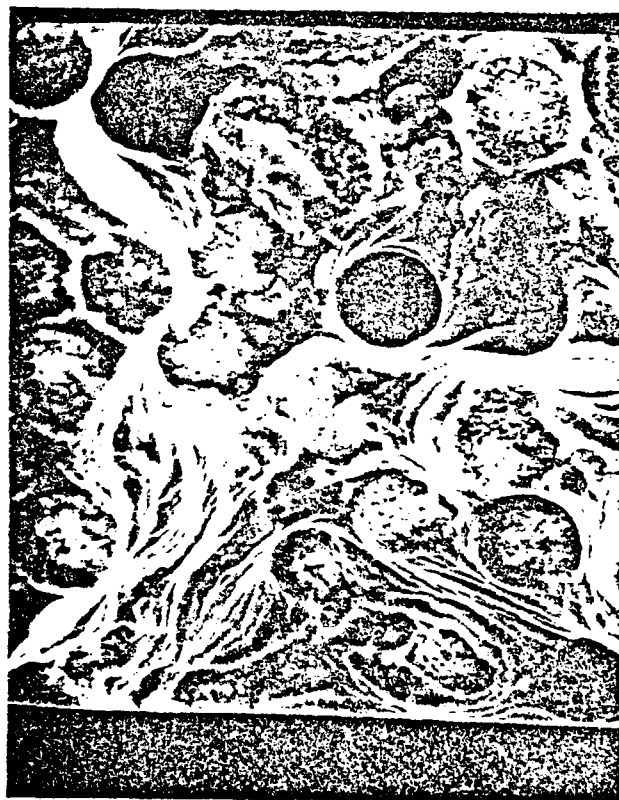


Figure 63: Fatigue Crack and Fiber Pullout on specimen 15/5 near tensile edge (800X)

while Figures 66 and 67 shown transverse fatigue cracks in the notched specimens. Notice, that in these regions the matrix material is smashed to various particular matter size. In the notched specimen 21/5 (Figures 66 and 67) a total of 90K cycles were performed after the longitudinal crack was detected. Since these surfaces appear to have finer particular matter than those in Figures 64 and 65, the implication is that the transverse cracks in the unnotched specimens grow to catastrophic lengths very rapidly, i.e., over a few number of load cycles.

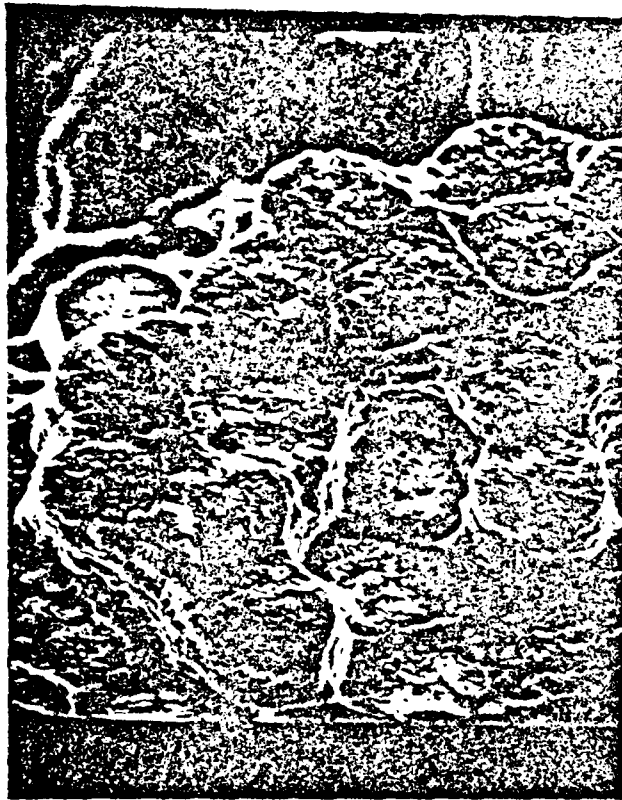


Figure 64: Fatigue crack, specimen 15/5, near tensile edge (1000X)



Figure 65: Fatigue crack, specimen 16/5, found near tensile edge
(1000X)

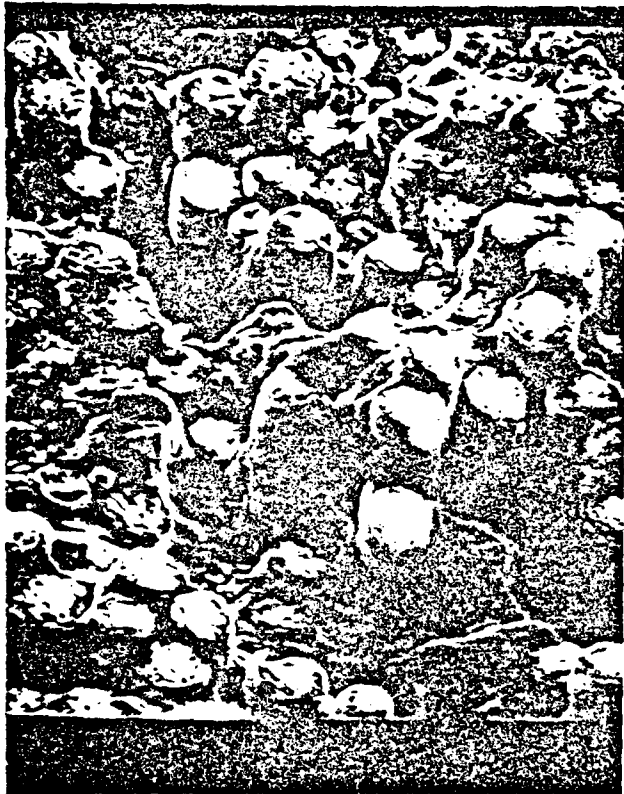


Figure 66: Transverse fatigue crack, specimen 21/5 (500X)



Figure 67: Transverse fatigue crack found on specimen 21/5 (1000X)

Tensile Edge

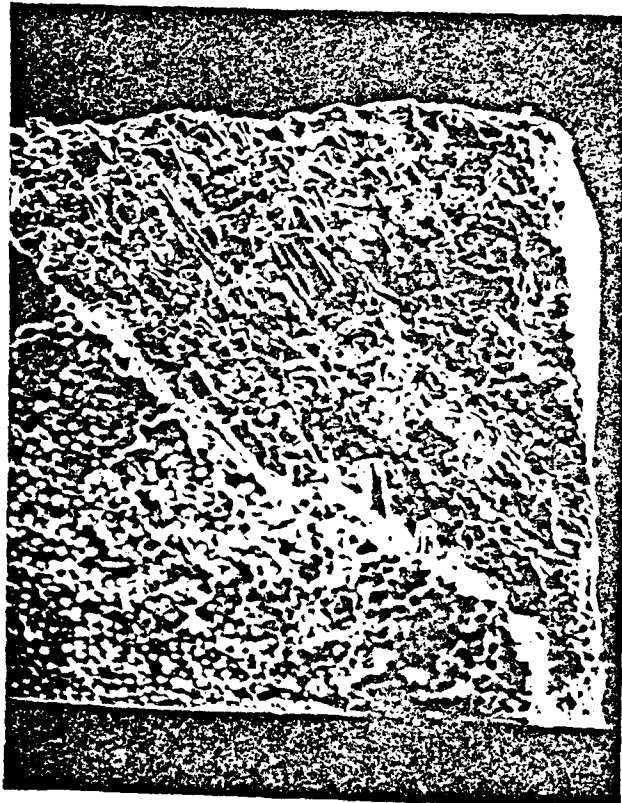


Figure 68: Transverse Fatigue crack growing from tensile edge of Specimen 16/5 (100X)

4. DISCUSSION AND SUMMARY

The objective of the research performed was to investigate the utility of different nondestructive evaluation techniques for metal matrix composites, in particular FP/Al. The characterization of material defects and damage development during load by various NDE techniques was to be examined. The material properties and specimen geometry substantially affect the ability of NDE techniques to characterize the damage state or to locate initial defects in a material. Therefore, the material properties were characterized by the response of the material to a variety of mechanical tests.

The mechanical response of FP/Al to axial loading was similar to that of many metals. FP/Al behaved linearly until the matrix material yield point was exceeded. After yielding, Young's modulus gradually decreased until failure. The yield stress, 15 to 20 ksi, was determined to correspond to the start of plastic deformation of the matrix material, an aluminum-lithium alloy.

A further indication of matrix plasticity was the change in Poisson's ratio that coincided with the yield point. The average value of Poisson's ratio was 0.25 before yielding and increased to an average value of 0.36 after yielding occurred. Assuming that the V_f is the average value of 50%, that ν for the aluminum matrix is 0.3 when elastic and 0.5 when plastic, and applying the rule of mixtures [19], it can be verified that the matrix undergoes plastic deformation. Using ν equal to 0.25 for the FP/Al and ν equal to 0.3 for the matrix, then ν for the fiber is calculated to be 0.2. After matrix yielding, if ν for the fiber is still 0.2 and ν for the matrix is 0.5, then ν for the FP/Al

after matrix yielding is calculated to be 0.35, which is very close to the experimentally measured value of 0.36.

Another characteristic of FP/Al behavior that is similar to many metals is the disappearance of the yield point on subsequent loadings. This property was utilized by making secant measurements of longitudinal modulus only when the material behaved elastically. As expected, the value of Young's (longitudinal) modulus was found to be dependent on the fiber volume fraction. For 55% V_f specimens the longitudinal modulus varied from 30 to 34 Msi, while for 45% V_f specimens the longitudinal modulus varied from 28 to 32 Msi.

In three point bending, FP/Al displayed some characteristics which were similar to those found in the axial tests. During the first loading cycle the matrix plastically deformed in those regions where the stresses were sufficiently large. Also, small regions of localized deformation under all three load points were encountered. However, as noticed in the axial tests, the material behaved elastically after several load cycles, i.e., the yield point disappeared. The values of flexural rigidity, calculated from a secant line, were slightly less than the measured values of longitudinal modulus. This discrepancy is primarily due to the assumption in elementary beam theory which neglects the shearing deformation. As previously mentioned, the parameter of primary significance to the present work is stiffness change.

During fatigue testing, considerable stiffness changes occurred. In the first 50K cycles of fatigue, substantial stiffness increases were found. These five to ten percent increases were apparently due to matrix work hardening. After about 100K cycles most specimens underwent

a stiffness reduction. This stiffness change, on the order of a two to four percent reduction (except for the notched specimens), is believed to have been caused by damage initiation along the tensile edge of the specimen. It is believed that damage consists of small matrix cracks and a small amount of fiber breakage. In the notched specimens a large stiffness reduction occurred. This reduction was found to be related to the elongation of the longitudinal crack. A direct correspondence between detected damage and stiffness was made using the elementary beam theory model.

As in all composite materials the complexity of the microstructure makes it difficult to determine the exact failure mode of FP/Al. Perhaps the best description of the failure can be had by making an analogy to a brittle metal. In brittle materials a small fatigue crack, when started, rapidly propagates to critical length. When the crack reaches critical length catastrophic failure occurs immediately. On the fracture surface two distinct failure modes exist: the region of fatigue cracking (indicated by characteristic particulate matter) and the region of catastrophic failure (indicated by the ductile shear surfaces and the large plastic deformation of the matrix material). In FP/Al two distinct regions of failure also exist. The predominant mode was found on all specimens whether the failure was fatigue or quasi-static. This mode is the catastrophic or almost instantaneous failure mode. The other failure mode only occurred in fatigue specimens at the tensile edge and therefore is believed to be a fatigue crack.

There were three reasons why the extensive NDE did not detect the existence of the transverse fatigue crack in the unnotched specimens.

First the crack length was very small. The longest measured transverse fatigue crack grew only 0.04 inches inward from the tensile edge. A SEM of the 0.04 inch crack is shown in Figure 68. Secondly, the location of the fatigue crack was always near the tensile edge, thus making detection difficult for many NDE techniques. Finally, the fatigue crack growth rate is believed to be rapid. Hence, unless one inspected more frequently during the fatigue test, it is likely that the crack could initiate and grow to critical length between NDE inspections and thus not be detected before failure.

There are several facts which substantiate the above comments. First transverse fatigue cracks of the size that appear in Figure 68 (0.04 inches) can be seen with the naked eye, thus making their detection after fracture easy. Secondly, the transverse cracks that grew from the notch tips were between 0.05 and 0.10 inches long, and the only NDE technique that detected those cracks was replication. Therefore, the transverse cracks are hidden by the region of edge effects of the various NDE techniques.

Finally, in comparing Figures 65 and 67, a significant difference can be noticed. Figure 67 shows a transverse crack that existed in a notched specimen for approximately 100K cycles while Figure 65 shows a close-up of the transverse crack in the same specimen shown in Figure 68. The transverse crack in the notched specimen (Figure 67) appears to have finer particulate matter than the transverse crack in the unnotched specimen (Figure 65). This implies that the crack in the unnotched specimen was exposed to fewer fatigue cycles (less mashing together) than the crack in the notched specimen, which was known to undergo 100K

cycles. Therefore, crack growth is believed to be relatively rapid.

Transverse cracks did not occur in all unnotched fatigue specimens. Some specimens, usually those which were fatigued at higher loads did not indicate the presence of transverse cracks. The entire failure surface of these specimens appeared to be in the catastrophic failure mode. In order to understand this, an analysis of the crack initiation process is needed.

Transverse cracks are believed to initiate when and where a sufficient concentration of local damage (fiber fracture and matrix cracking) has occurred to cause a local region to fracture. When this happens the material either relieves the stress concentration caused by local failure or it does not. If the material relieves the stress concentration, a fatigue crack is believed to develop; if not, catastrophic failure occurs without the presence of a transverse fatigue crack zone.

The fatigue load has a considerable effect on transverse fatigue crack growth. This is because the critical crack length varies with stress (load) applied to the crack. Therefore, catastrophic failure is more likely to occur sooner when the applied load is higher. This observation is supported by Figure 10 and by the observation that transverse fatigue cracks were more common in specimens that were fatigued at lower load levels.

In the notched specimens the transverse cracks did not propagate to critical lengths because the normal stress concentration was effectively eliminated by the longitudinal crack. The stress concentrations at the notch and crack tips are not investigated here; however, it is believed that the shear stress concentrations are what govern the growth of the

longitudinal crack. As previously mentioned, no evident correlation between the longitudinal crack and the longitudinal striations that were believed to be ply interfaces was found to exist. Instead the longitudinal crack started 0.005 to 0.010 inches from the crack tip, again implying that local shear stress concentrations caused the initiation of the longitudinal crack.

Every NDE technique had its own set of advantages and disadvantages. For example, the X-ray and C-scan techniques provided good overall pictures of the specimen, while other techniques such as replication, eddy current and ultrasonic attenuation were only used to investigate regions of interest. Some techniques were more reproducible than others. For example, ultrasonic C-scans were easily reproduced but it was very difficult to reproduce consistent data using the ultrasonic attenuation equipment and the techniques available in our laboratory at the present time. An individual flaw, or particular type of damage could not be detected by every NDE method, therefore, the NDE method must be chosen so as to be matched to the type of flaw or type of damage. In general, several NDE methods will have to be used to provide complementary information about the damage state.

X-ray radiography was found to be a valuable NDE technique. It provided excellent detail of the internal defects, such as longitudinal striations, matrix voids and the region at the end of the specimen caused by the matrix injection process (the matrix injection zone). The actual nature of the imperfection here has not yet been determined. Radiography with image enhancing penetrant detected the presence of longitudinal cracks. However, transverse cracks could not be detected

by this technique. The primary limitation of X-ray radiography was found to be edge distortion. The outer 0.01 inches on both sides of the specimen were subject to this effect. The transverse cracks, if indeed they exist during the intermediate NDE tests, did not grow any larger than 0.01 inches from the edge prior to failure. Also small interior defects were not detected by image enhancement procedures unless exposed to the surface by matrix cracks.

Ultrasonic C-scan was another valuable NDE technique. It detected longitudinal striations, matrix voids and the matrix injection zones. The damage created by fatigue loading was evident in many specimens. It is possible that either small matrix cracks or the matrix work hardening, or both, increased the attenuation of the material, thus giving the appearance of damage. Although it appeared slightly distorted the longitudinal crack was easily detected. Distortion due to the ultrasonic beam size was both an advantage and disadvantage of the ultrasonic C-scan technique. Distortion slightly reduces the resolution in the specimen interior and also causes an edge effect of approximately 0.03 inches on all edges of a crack, a flaw or the specimen. However, this distortion allows ultrasonic C-scan to evaluate the quality of small regions rather than of geometrical points, thus making the C-scan technique less sensitive to the material microstructure. This is evident when comparing the observation of longitudinal striations by X-ray and C-scan. The X-ray shows high local detail while the C-scan shows strips.

Problems with inconsistent coupling between transducer and specimen made the measurement of ultrasonic attenuation difficult to repeat. Also, when transducers generate beams which are 1/4 or 1/2 in wide in a

1/2 inch wide specimen, good resolution can not be obtained. As a result, small defects and variations such as matrix voids and longitudinal striations can not be resolved. However, larger regions such as the matrix injection zone tended to have slightly higher attenuation. With increased reproducibility of data, of course, it is possible that this technique may be useful in obtaining an estimate of the integrated damage state over the volume of material scanned. For composites, the integrated damage state may play a more important role in failure than any individual details of damage. Knowing that the longitudinal crack existed, an ultrasonic A-scan technique was developed to detect it. The transducer was placed on the smallest edge and the time delay of the returning pulse verified the existence of the through crack.

The use of thermography by the techniques described earlier was not very effective as an NDE technique for FP/Al because significant thermal patterns developed only near failure. Heat was generated on the compression side during fatigue cycling, but this apparently did not indicate the presence of a flaw or of damage development. Heat generated by the longitudinal crack was not visible until the crack propagated to a length where it could be detected visually if the specimen was under load. When failure occurred, a substantial thermal pattern developed but dissipated rapidly thereafter. The rapid dissipation of the heat generated occurs since FP/Al is a good thermal conductor, thus making the detection of flaws or minor damage by this technique difficult. The heat generated at the notch tip was not substantial at lower loads even when observed through the microscope attachment of the thermographic camera.

The replication procedure was the best method of the ones used here

for monitoring the growth of the longitudinal notch. Replication provides a quick and simply obtained permanent record of the specimen surface. It was the only method that detected the existence of transverse cracks growing from the notch tips. However, no transverse cracks were ever detected in unnotched specimens before failure, either because there were not any when the specimen was replicated or because the cracks were not opened by the axial loading applied while replicating. Perhaps the biggest drawback of replication is obvious, only exposed surface defects or damage can be detected.

As discussed earlier in this chapter, the large stiffness changes encountered were apparently the result of both matrix work-hardening and damage development. The knowledge that the material is becoming less stiff strongly implies the development of damage. This is verified by the performance of the notched specimens. A definite correlation was developed between stiffness change and longitudinal crack length. This correlation was successfully modeled using beam theory with reduced cross-sectional areas. However, other than the longitudinal crack, no information correlating the type of damage to stiffness change is presently available for FP/Al. Other studies in graphite-epoxy, for example [5], have shown a strong correlation between different types of damage and stiffness degradation.

Except in the case of the longitudinal cracks that grew in the notched specimens, no significant variance could be found in the eddy current results. This is believed to be caused by two factors. First, a relatively large region of the material surrounding the probe affects the eddy current readings. This is the cause of the very

evident edge effect discussed in chapter two. Secondly, the inspection frequency used did not appear to be sensitive enough to material variances such as the large matrix voids.

As with stiffness change, acoustic emission can detect only the actual development of damage. It can not presently be used to characterize the type of damage that emits the acoustic energy. Large acoustic emissions were concentrated around two zones, near the matrix yield stress and at loads approaching failure. When near failure, the AE is believed to come from energy released in the region where damage development is occurring. The types of damage that create various energy levels and rate of AE are unknown at this time.

The exclusive use of one NDE technique gives an incomplete picture of the specimen condition. Any one technique can not indicate the presence of all flaws and can not completely characterize the damage state. Also, any one technique may not distinguish between types of flaws or damage that is present. This concept is best explained by examples.

Ultrasonic C-scan, X-ray radiography, eddy current and ultrasonic pulse-echo all detected the presence of the longitudinal crack that propagated away from the notch tip, but none of these techniques indicated the existence of the transverse crack. If the notched specimens had not been replicated, the transverse crack would have gone undetected until the failure surface was examined.

Similarly the matrix voids were detected only by ultrasonic C-scan and X-ray radiography. However, upon examination of the ultrasonic C-scan it would be difficult to distinguish matrix voids from matrix

injection regions. These both appear as white (high ultrasonic attenuation) regions on the C-scans. When a comparison is made with the radiographs, a distinction becomes evident. Matrix voids do not impede the transmission of X-rays, but the matrix injection zone does.

As previously discussed, all NDE techniques had characteristic limitations. Radiography, C-scan, ultrasonic attenuation and eddy current were all subject to edge effects. Even with the use of penetrant, the distortion of X-rays by the specimen edge prevented the detection of transverse cracks. Edge distortion also prevented detection in notched specimens where transverse cracks about 0.01 inches long were known to exist. A lower bound on the X-ray edge effect can be determined by comparing the width of the radiograph to the specimen width. The specimens are, on the average, 0.02 inches wider than the radiographic image, thus explaining why the transverse cracks could not be detected. Similarly, ultrasonic C-scan has a beam width that creates a 0.03 to 0.04 inch edge effect that distorts damage near the edge. The eddy current probe, operating at a frequency of 100K Hz, was determined to be subject to edge effects when the probe center was within 0.08 inches of the edge. The size of the area under the influence of the attenuation transducer makes it impractical to detect the location of small transverse cracks. In other words, the only technique employed in this study that is effective near the edge is replication, which is sensitive only to defects open to the surface.

5. CONCLUSIONS

The conclusions of this work are broken down by category and listed on the following pages. The knowledge gained about the material behavior of FP Aluminum is presented. Also an evaluation of each NDE technique, including advantages, disadvantages and results and a separate section on areas for future investigations is presented.

1. Mechanical Behavior of FP Aluminum

- The aluminum matrix work-hardens.
- FP/Al behaves like a brittle material. This is characterized by the rapid transverse crack growth which quickly reaches catastrophic length.
- The fatigue failure process is believed to be controlled by local damage build-up (fiber failure and matrix cracking), rapid transverse crack growth to a critical size, and catastrophic failure.
- Longitudinal cracks are formed by shear stress concentrations that exist near the notch tips in notched specimens.
- In only one case was a detectable initial flaw associated with the final failure site.

2. X-Ray Radiography

- Radiography provides very good detail of the specimen interior.
- The entire specimen (less edge effects) is characterized.
- Initial defects such as matrix voids, matrix injection zones and longitudinal striations can be detected by radiography.
- With the use of TBE as an enhancing penetrant, damage such as longitudinal cracks were detected.

- In only one specimen was damage found by this technique at the final failure location.
- The edge effect prevented the detection of any transverse crack which initiated at the edge.

3. Ultrasonic C-Scan

- C-scanning provides fair detail (in comparison with X-ray radiography) of the specimen interior.
- The entire specimens (less edge effects) is characterized.
- Initial defects such as matrix voids, matrix injection zones and longitudinal striation can be detected by C-scan.
- The C-scan technique correlated well with the X-ray radiography technique.
- Damage, believed to be matrix cracking and/or work-hardening, was indicated in specimens subjected to fatigue.
- The longitudinal cracks were detected.
- Edge effects prevented the detection of any transverse edge cracks.
- C-scanning, as applied in this work, yielded qualitative and not quantitative information.
- Using the method described, reproducible results can be obtained.
- Better perception was given by the multiple trigger level C-scan technique.

4. Ultrasonic Attenuation

- The ultrasonic transducer used in this study was too large to provide detail.
- Large initial defects such as the matrix injection zone can be detected.

- Consistent coupling between transducer and specimen was difficult to achieve and hence data was not very reproducible.
 - Longitudinal cracks could be detected by transmitting the pulse across the width of the specimen.
 - The attenuation measurement correlates well with C-scan in those regions where large-scale damage or defects are present.
5. Thermography
- The heat generated on the compression side during bend tests shows a relationship with the stress-state.
 - Heat generation, that cycles with fatigue load at the longitudinal crack, shows promise for detection of flaws in other materials.
 - FP/Al is too thermally conductive for the development of substantial thermal patterns.
6. Replication
- The replication method provides excellent edge and surface detail.
 - Both longitudinal and transverse cracks can be detected under load.
 - This technique is limited to defects open to the surface.
 - Replication did not detect transverse cracks in unnotched specimens.
7. Stiffness Change
- Damage development in both notched and unnotched specimens was indicated by changes in stiffness.
 - A good correlation exists between the extent of damage (longitudinal crack length) and stiffness.
 - Stiffness change resulting from the growth of longitudinal crack could be modeled using beam theory.

- The type of damage is not, in general, indicated by stiffness change.
8. Eddy Current
- FP/Al was insensitive to the operating frequency, 100K Hz, used in this work.
 - Longitudinal cracks could be detected.
 - One was unable to detect initial defects, transverse crack and other damage development with the specific eddy current technique used here.
9. Acoustic Emission
- An increase in AE count rate coincided with the onset of matrix plasticity as determined from the proportional limit of the stress-strain curve.
 - Damage development at high loads was indicated by an increase in AE rate.
 - Some correlation exists between a low number of AE and higher strengths.
10. Additional Research
- Does ultrasonic wave speed change with damage or matrix strain hardening?
 - What is the effect of other operating frequencies of eddy current systems?
 - Is stiffness change (unnotched) caused by matrix cracking and fiber breakage?
 - Testing of different thermographic techniques such as passive heating methods.

- Is acoustic emission actually caused by matrix plasticity and/or other type of damage development?
- Further experimental efforts (especially replication under bending load) should be attempted to see if transverse cracks which grow in unnotched specimens can be detected.
- Investigation into the stress concentrations governing longitudinal crack formation and growth should be undertaken.

6. REFERENCES

1. M. A. Knott, "The Detection and Effect of Fabrication Damage in Boron Aluminum Composites," M.S. Thesis, Virginia Polytechnic Institute and State University, September 1976.
2. D. T. Hayford, E. G. Henneke, and W. W. Stinchcomb, "The Correlation of Ultrasonic Attenuation and Shear Strength in Graphite-Polyimide Composites," Journal of Composite Materials, Vol. 11, October 1977, pp. 429-444.
3. T. S. Jones, "Thermographic Detection of Damage Regions in Fiber-Reinforced Composite Materials," M.S. Thesis, Virginia Polytechnic Institute and State University, April 1977.
4. K. L. Reifsnider and J. E. Masters, "Investigation of Characteristic Damage States in Composite Laminates," ASME 78-WA/Aero-4, September 1979.
5. T. K. O'Brien and K. L. Reifsnider, "Fatigue Damage: Stiffness/Strength Comparisons for Composite Materials," Journal of Testing and Evaluation, Vol. 5, No. 5, September 1977, pp. 384-393.
6. C. N. Owston, "Eddy Current Methods for the Examination of Carbon Fibre Reinforced Epoxy Resins," Materials Evaluation, November 1976, pp. 237-244.
7. E. G. Henneke, II, C. T. Herakovich, G. L. Jones, and M. P. Renieri, "Acoustic Emission from Composite-Reinforced Metals," Experimental Mechanics, Vol. 15, January 1975, pp. 10-16.
8. E. G. Henneke, II, and H. W. Herring, "Spectrum Analysis of Acoustic Emissions from Boron-Aluminum Composites," Composite Reliability, ASTM STP 580, 1975, pp. 202-214.
9. S. S. Russell, "Signature Analysis of Acoustic Emission from Graphite/Epoxy Composites," M.S. Thesis, Virginia Polytechnic Institute and State University, June 1977.
10. S. P. Timoshenko, Strength of Materials, Part I, Van Nostrand, New York, 1955.
11. E. P. Popov, Mechanics of Materials, Prentice-Hall, Englewood Cliffs, New Jersey, 1952.
12. C. Zweben, W. S. Smith and M. W. Wardle, "Test Methods for Fiber Tensile Strength, Composite Flexural Modulus, and Properties of Fiber-Reinforced Laminates," ASTM STP 674, 1979, pp. 228-262.
13. N. J. Pagano, "Analysis of the Flexure Test of Bidirectional Composites," Journal of Composite Materials, Vol. 1, 1967, pp. 336-342.

14. J. M. Whitney, C. E. Browning and A. Mair, "Analysis of the Flexure Test for Laminated Composite Materials," ASTM STP 546 1974, pp. 30-45.
15. D. T. Hayford and E. G. Henneke, II, "A Model for Correlating Damage and Ultrasonic Attenuation in Composites," ASTM STP 647, 1979, pp. 184-200.
16. T. K. O'Brien, "An Evaluation of Stiffness Reduction as a Damage Parameter and Criteria for Fatigue Failure in Composite Materials," Ph.D. Thesis, Virginia Polytechnic Institute and State University, October 1978.
17. G. J. Dvorak and W. S. Johnson, "Fatigue of Metal Matrix Composites," Submitted August 1979 for publication in a Special Issue on "Fatigue of Composites and Non-metals," of the International Journal of Fracture.
18. W. F. Brown, Jr., and J. E. Srawley, Plane Strain Crack Toughness Testing of High Strength Metallic Materials, ASTM, Philadelphia, PA., December 1967.
19. R. M. Jones, Mechanics of Composite Materials, McGraw-Hill, New York, 1975.